University of South Carolina

Scholar Commons

6-30-2016

Study of Friction Extrusion and Consolidation

Xiao Li
University of South Carolina

Follow this and additional works at: https://scholarcommons.sc.edu/etd

Part of the Mechanical Engineering Commons

STUDY OF FRICTION EXTRUSION AND CONSOLIDATION

by

Xiao Li

Bachelor of Science
Hohai University, 2008

Master of Science
Hohai University, 2011

_____

Submitted in Partial Fulfillment of the Requirements

For the Degree of Doctor of Philosophy in

Mechanical Engineering

College of Engineering and Computing

University of South Carolina

2016

Accepted by:

Anthony P. Reynolds, Major Professor

Michael Sutton, Committee Member

Xiaomin Deng, Committee Member

Joshua Tarbutton, Committee Member

Paul Ziehl, Committee Member

Lacy Ford, Senior Vice Provost and Dean of Graduate Studies

DEDICATION

To my Mom Ping, for giving me life

To my wife Shanshan, for giving me love

To my Oncoming daughter Aurora, for giving me hope

ACKNOWLEDGMENTS

This dissertation was made possible due to the masterly guidance of Dr. Anthony P. Reynolds. I was nourished profoundly from your erudite knowledge, dedication to work, optimistic attitude to life and spirit of always seek truth from facts. You set a good example of both researcher and experimentalist. Those countless brainstorm enlightens me to think critically and deeply, today and tomorrow. I can't feel luckier to have you as my Ph.D. advisor.

Dan, you are the best engineer and model plane maker in the world. Only your generous selfless help makes my experiments possible and I feel I owe you too much that can't be expressed by words. I also gratitude to Dr. Wei Tang, who helped me get along with USC and living in Columbia. Your methodology and advises are still guiding me find the right path. I appreciate my committee members' effort of helping me improve this dissertation and providing valuable suggestions for my research.

To make my past five years unique, not only it is a course of pursuing doctor degree but also a wonderful journey of knowing friends come from all over the world. I am amazed by the transcultural communications between people who born in lands and cultures apart, who exchange thoughts with spark but respects as well. I sincerely thank all my group members, also my comrades and partners: Piyush, Rabby, Clinton, Joel, Hussein, Xiaomin, Hejun, Dawei, Ryan, Marie, Mathieu, Corbin, Ilana, Jeffery and many people who worked with me and help me in academic area or daily life. I miss the moments not only we can

share our idea of research but also our feeling and attitude to the entire world. Love in advancing side, life in retreating side. All little drops of time shared with you come together as a priceless stream that will always flow in my mind.

ABSTRACT

Friction extrusion and consolidation was invented by The Welding Institute (Cambridge, UK) in the early 1990's. It is related to simple extrusion processes with the primary difference being that the extrusion die rotates about the extrusion axis and the die is required to impart substantial deformation to the initially, finely divided charge (like metal waste or chips) in order to consolidate it prior to extrusion. It can produce high quality wire and fully consolidated bulk material from low-cost precursors like metal chips or powders. The advantages lie in that it is a direct method to recycle metal chips or scraps and considered as more convenient, economical and "green" process when compared with conventional recycle processes involving melting and casting. This is a novel process believed to have huge potential for producing high quality wire products with customized chemical composition for fusion welding and additive manufacturing with relatively simpler devices and less time/labor/energy requirements.

This dissertation work aims to develop insight understanding of the underlying physics of friction extrusion and consolidation processes and enable its use for a wide range of high value-added manufacturing applications, like additive manufacturing. The specific works are listed as follow: The thermal-mechanical progression of friction extrusion and consolidation process was studied experimentally and numerically. The deformation and material flow were revealed via a marker insert technique, thus, strain in friction extrusion

wire is deduced. The relationship between control parameters (like extrusion/consolidation force and die rotational speed) and responses (like torque, extrusion rate, grain size and features of marker pattern etc.) were analyzed. Electron backscatter diffraction result showed that there is no strong texture preference in friction extruded aluminum wire. Using friction extruded aluminum alloy wire, wall samples were built via wire and arc additive manufacturing. Finite element simulation helped predict heat transfer and temperature field during the additive manufacturing process. Post-analysis indicates that good mechanical properties can be achieved if favorable thermal management was provided.

TABLE OF CONTENTS

ix

LIST OF FIGURES

LIST OF TABLES

CHAPTER 1

INTRODUCTION AND BACKGROUND

1.1 Introduction

Along with rapid developing of aerospace industry and manufacturing in 2010's, novel technologies like additive manufacturing, solar energy jet and fuel cell battery play growing critical role in producing safe, economical and durable products. With regard to traditional manufacturing processes, more efficient, green, energy saving and environmentally friendly technologies are required to confront new challenges in coming industry revolution.

Friction extrusion (FE) was invented at The Welding Institute (Cambridge, UK) in the early 1990's and subsequently largely ignored. It was first derived from friction stir processing as a method of forming or reforming metal/ceramic composite material [1]. It is related to simple extrusion processes with the primary difference being that the extrusion die rotates about the extrusion axis and the die is required to impart substantial deformation to the initially finely divided charge (like metal waste or chips), in order to consolidate it prior to extrusion, see Figure 1.1.
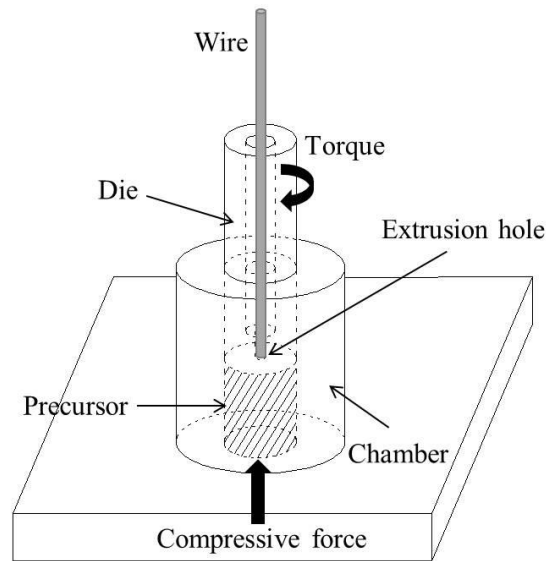
Figure 1.1 Schematic diagram of friction extrusion process

For initially unconsolidated charges, the shearing and heating due to dissipation of the plastic deformation imparted by the rotating die lead to consolidation and subsequent extrusion of the feedstock material. As with other friction-based processes, FE is a nominally solid-state process with peak process temperatures below the bulk melting point of the material being processed. This process is well suited for creating solid wire/rod from particulate materials such as metal powder or machining chips. As such, one of its primary applications may be in the recycling of otherwise low values material streams. The process may also be of value for the production of small lots of custom composition wires for either welding or wire-arc additive manufacturing feedstock. The difference between friction consolidation (FC) and friction Extrusion is that friction consolidation does not have extrusion hole in the rotating tool. Friction extrusion can be used for recycle metal waste as well and meanwhile extrude products like wire or rod by a single process without

2

complex devices and high energy input. Friction consolidation can convert metal powders or metallic waste such as machining chips or swarf directly into produce useful fully dense metallic disc

Metal wire is a single, usually cylindrical, flexible strand or rod of metal. As a final product, like wire net, engineered spring or cable core, it is used to bear mechanical loads, electricity or telecommunications signals. Also, it was commonly used in modern manufacturing industrial processes like fusion welding and additive manufacturing as a convenient feedstock. The main method of producing wire is by drawing metal through a hole in a die or draw plate. However, it is inconvenient to make a wire with special chemical composition and/or relative thin diameter because multi-steps of alloying and drawing are required. At the same time, considerable time and energy are consumed during drawing processes. Besides, not all metals and metallic alloys possess the physical properties necessary to make useful wire. For conventional manufacturing methods, the metals must be ductile and strong in tension, the quality on which the utility of wire principally depends on. The metals suitable for wire, possessing almost equal ductility, are platinum, silver, iron, copper, aluminum and gold; and it is only from these and certain of their alloys with other metals, principally brass and bronze, that wire is prepared[2]. Therefore, an alternative way of producing wire with custom chemical composition, high efficiency, less waste or friendly-to-material is highly valuable.

Recycling is a process to convert waste materials into new products to prevent waste of potentially useful materials, reduce the consumption of fresh raw materials, reduce energy usage, reduce air pollution (from incineration) and water pollution (from landfilling) by reducing the need for "conventional" waste disposal[3]. Aluminum recycling can save up to 95% energy that would be needed to create a comparable amount from raw materials[4]. However, the conventional method of recycling and reuse process consists of multiple steps of refining, re-melting and casting, which is a complex process of converting waste into useful products and considerable labor and power were required. Also, special devices and strict working environment are demanded due to high temperature liquid-state metal involved in the process. There is no doubt that considerable benefits will bring about if reasonable simplification and energy/labor saving can be achieved in recycling and reuse process. The last but not least, in certain extreme environments like outer space or underwater, liquid state is highly unfavorable. It is worthy to develop a solid-state alternative recycling and manufacturing process for such situations.

In this research, friction extrusion is proposed as a convenient manufacturing process of producing high quality metal wire and bulk material from finely divided precursor or metal wastes with one step process and relative simpler equipment requirements compared to conventional recycle process. The physical mechanism is studied and illustrated, features of products are presented, the influence of control parameters on process and product are analyzed, a reasonable thermal mechanical model

is established and validated, and viability of being used for additive manufacturing is proven.

1.2 Background of research and motivation

Aircraft and spacecraft have always been fabricated from high performance, structural, materials. Competition between the composites and metallic materials communities has led to continuous improvement in the performance of both classes of materials. However, the cost of increased performance is typical, increased cost. As high performance materials become increasingly expensive, manufacturing methods which reduce waste and improve (reduce) the buy-to-fly ratio are of increasing interest to the aerospace community. Use of integral metallic structure (versus built-up structure) is a potential route to improved performance and lower cost through reduced part count and reduced labor costs. The integral structure may be produced by various methods including (1) high-speed machining from thick plate, (2) additive manufacturing (e.g., free form fabrication), and (3) welding of simple extruded and/or rolled forms to produce more complex structures (e.g. stiffened skins). High speed machining results in a large volume of waste (machining chips) and a high buy-to-fly ratio (and a great deal of associated energy waste). Ideally, machining waste would be recycled into high value added material, though the technology for doing so effectively remains elusive for many aerospace materials. Since many fusion welding and additive manufacturing techniques require a wire feedstock (e.g.

NASA's Electron Beam Free Form Fabrication, EBF3), it follows that a technology which can produce high quality wire or fully consolidated bulk material from finely divided metals (e.g. machining chips or low-cost, powder precursors) would be a useful adjunct to both the integral machining process and many free form fabrication processes. Such a process would likely be economical and "green": direct conversion of such waste without an intervening melting step should be relatively energy efficient. Besides, the wire products in current manufacturing industry cannot fulfill the requirements of rapidly developing additive manufacturing in types and special composition. The friction extrusion process (FEP) was invented and patented in early 1990's by W. Thomas[1]. It is a novel friction based extrusion method for producing high quality wire or rod with custom chemical composition from low-cost precursors (e.g. powders and chips). As will be shown in the remainder of this dissertation, friction based consolidation and extrusion fulfills these needs.

In recent decades, our step of discovering outer space was slowed down. The reasons behind this are complex. In a practical way, there are two major barriers to discover outer space: (1) Extreme cost in travel and manufacturing. (2) Technical difficulties like resource shortage, zero-gravity condition and space debris collision. One avenue to overcome the above barriers is outer space manufacturing. If we could recycle space junk or waste to usable feedstock and remake it to new parts or machines, we not only reduced the collision chance of space stations but also realize "made in space" and save huge consumption on transportation and repair. Additive manufacturing (AM) has gained much

6

attention due to its flexible functions and robust features. Especially, the wire-based AM like fused deposition modeling (FDM) and wire and arc additive manufacturing (WAAM) could be a potential manufacturing avenue in the zero-gravity environment. Recently, NASA started an outer space AM project to realize the application of a 3D printer with plastic material[5]. However, the current study has involved neither metal feedstock AM nor metal reuse technologies for outer space manufacturing. To close the gap between recycling space debris and practical additive manufacturing in zero-gravity, friction consolidation and extrusion is proposed as a novel manufacturing solution here. It has many advantages like less device/space demanding and durable in an extreme environment, so can potentially be utilized in out space manufacturing.

Although friction extrusion was already invented for twenty years, its physical mechanism, advantage and potential application have not been well studied. Therefore, it is necessary to develop an in-depth understanding of the physics of the friction extrusion process and establish reasonable finite element simulation model to interpret its thermal mechanical history. The relationship between process conditions/parameters (like extrusion force, rotational speed, the size of die hole, the pattern on die surface etc.) and characteristics of product (texture, microstructure, grain size, redistribution state, hardness and surface finish etc.) should be analyzed. More important is to enable its use for a wide range of high value-added manufacturing applications or fusion welding feedstock. The shortcomings, limitations, and a potential way of improvement also need to be discussed.

7

1.3 Dissertation Layout

This dissertation is divided into six chapters:

(1) Chapter 1 presents a brief introduction of friction extrusion and consolidation with industrial background and anticipated applications. The motivation, objectives and methodology of this dissertation are also elucidated.

(2) Chapter 2 reviews the history of friction extrusion and consolidation as a friction stir processing. Related conventional manufacturing and recycling methods are compared with friction extrusion and consolidation. As a potential way to apply friction extrusion wire, additive manufacturing especially wire and arc additive manufacturing was introduced. Methods of simulation of this process are also reviewed.

(3) Chapter 3 focus on studying friction extrusion process using experimental analysis and numerical simulation approach. The with following aspects are mainly discussed: (a) experimental apparatus and procedure, (b) progression of process, (c) features of wire product, (d) material flow, (e) effects of control parameters on process, (f) post-extrusion drawing and annealing, (g) validation of finite element models.

(4) Chapter 4 includes friction consolidation using aluminum chips and oxide dispersion steel, respectively. The progress of the friction consolidation process is

revealed by studying a series of partial consolidations with increasing processing time. The effect of initial sizes of precursors on the consolidated disc is analyzed. The efforts of experimental parameters on deformation are quantified.

(5) Chapter 5 introduces (a) produce and analyze friction extrusion wire made for additive manufacturing, (b) build wire and arc additive manufacturing sample using friction extrusion wire, (c) finite element simulation of aluminum wire and arc additive manufacturing. The feasibility, shortcomings, and possible ways of improvement of this technology are discussed.

(6) A summary of the research outcome is stipulated in Chapter 6 with the concluding remarks and provision of future works for further research directions.

CHAPTER 2

LITERATURE REVIEW

2.1 General background

Friction consolidation and extrusion was invented at The Welding Institute (Cambridge, UK) in the early 1990's. It was first derived from friction stir processing as a method of forming or reforming metal/ceramic composite material[1]. Subsequently, it was largely ignored for years until early 2010's. The boom of aerospace industry and rising of additive manufacturing aroused attention to friction extrusion due to its great potentials in recycling and producing high quality feedstock with customized chemical composition for wire-based processes. In this chapter, literature and manufacturing methods are reviewed for depicting a thorough background of friction consolidation and extrusion process in the following aspects: (1) friction stir process and other relative researches (2) comparing friction consolidation and extrusion with relative conventional manufacturing and recycling methods (3) additive manufacturing and applications.

2.2 Friction stir process

A friction stir process (FSP) is general designation of various kind processes which push a non-consumable rotating tool friction stir on/into material to change the properties of metal or alloy through severe plastic deformation. Mishra et al. firstly proposed the term friction stir process in 1999 and adopting friction stir welding to refine the microstructure of aluminum alloy[6]. In series of works[7]–[11], FSP was proven have the ability of improving the superplastic behavior via severe plastic deformation and inspired many other concepts based on "friction stirring", like friction stir casting modification[12], friction stir micro-forming[7], friction stir channeling[13] and friction stir fabrication of surface composite[9].

2.2.1 Friction stir welding

Friction stir welding is most common used and well-known friction stir process. Friction extrusion and consolidation possess many commons with friction stir welding in many aspects, like physical mechanism, advantages, experimental device, applicable material and microstructure evolution. Therefore, it is worthy to review friction stir welding first as a headstream of friction extrusion and consolidation process.

Friction stir welding was invented at The Welding Institute (TWI) of the United Kingdom in 1991 as solid-based joining process[14]. The process can be described as a rotating pin with shoulder is inserted into the abutting edges of plates to be joined and

subsequently travel along the welding path as shown in Figure 1 [15]. Divided by the abutting interface, the side which tool moves in the same direction with welding is known as advancing side, the other side which tool moves in the opposite direction of welding is called retreating side. Friction stir welding can be thought of as a process of constrained extrusion under the action of the tool[16]. The friction around the pin tool causes plastic deformation and consequent heat dissipation. Along with increased temperature, the neighboring material is softened and stirred around the pin. But it remains in solid-state and is constrained by the tool shoulder during the process.
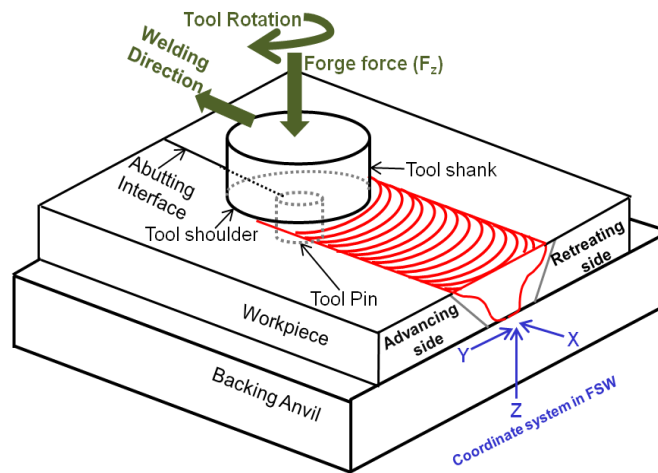
Figure 2.1 Schematic diagram of friction stir welding

The major advantages of friction stir welding, as well as friction consolidation and extrusion, are listed as follows:

(1) Due to it is a solid state process, many unfavorable features in conventional welding like porosity, hot cracking, element loss, etc. are avoided in friction stir welding.

(2) It is a robust process. It works in special conditions like outer space or underwater.

(3) No filler wire is required. Extra material is saved.

(4) No shielding gas for aluminum alloy and copper welding.

(5) Operated by machine and doesn't rely on special skill. Manual operation is not required.

(6) The energy requirement of friction stir welding is lower than laser welding[16].

(7) Tolerant to poor quality edge preparation.

In friction stir welding, tool plays a critical role in heat generation, material flow pattern and quality of the weld. The processing temperature might be reached elevated temperature of the workpiece, and it is strictly forbidden that the tool reacts with the workpiece or the environment. So, tool material is the first thing to be determined. For material as aluminum or magnesium alloys, tool steel like AISI H13 chromium-molybdenum hot-worked air-hardened steel is most commonly used due to its good elevated-temperature strength[17]. When it comes to harder alloys such as steels and Titanium alloys, polycrystalline cubic boron nitride tools and tungsten based tools are preferred due to high strength and hardness at elevated temperature[17]. The range of

weldable material for friction stir welding is wide: aluminum and alloys, copper, brass, magnesium, titanium, steel alloys, stainless steel, tool steel, nickel, lead and so on.

During both friction stir welding and friction extrusion, the severe plastic deformation in friction stirred zone brings about fine, equiaxed grain structure to material. Mishra et al. first proposed friction stirring to refine microstructure of material[6]. After that, the ability of friction stir process on improving the superplastic behavior of metals and alloy are presented.[6]–[8], [11] Therefore, the studies of microstructure evolution in friction stir welding are fairly instructive in the analysis of friction extrusion process. The banded microstructure in 2XXX series aluminum alloy friction stir welding was related with hardness and crack propagation process[18], [19]. Some attempts are made to explain multi-layer material flow and onion ring structure in friction stir welding but none of them are complete[20]–[22]. Seidel and Reynolds successfully applied a marker insert technique to illustrate the material flow in the friction stir welding process[23]. Grain characteristics and texture evolution in friction stir welds of nanostructured oxide dispersion strengthened ferritic steel are illustrated using electron backscatter diffraction (EBSD)[24].

2.2.2 Friction consolidation and extrusion

A friction forging process was developed in 1975 by D. R. Andrews and M. J. Gilpin[25]. It is a process of using a die to shape the resultant flash but not involved with extrusion. Inspired by this process, the friction extrusion process (FEP) was invented and

14

patented in early 1990's by W. Thomas[1]. It is a friction based extrusion method for producing high quality wire or rod from low-cost precursors (e.g. powders and chips). It can be developed into a recycling process for various metals and alloys and eliminate the energy and labor intensive processes of melting and casting.

Tang and Reynolds rekindled this technology and produced high quality aluminum wires from machining chips[26]. Hardness tests and bending tests were performed and the results were related to experimental parameters. Extrusion rate was simply related to the power input and die rotational speed. The fully equiaxed, recrystallized microstructure in extruded wire was observed. But, neither the trend of process nor material flow has been revealed. With similar principle, a testing machine using combined pressure and shear to granulate and recycle aluminum was built by Wideroe et al[27]. The result indicated that the shear movement remarkably reduced minimum axial force for compacting aluminum scrap. Also, they showed that the number of revolutions of rotating tool influences penetration depth and mixing range. Since limited experimental parameters were used, the relationship between control parameter and results like flow pattern and microstructure was not well explained. Abu-Farha successfully produced fine-grained tube via friction back extrusion[28]. A rotating tool is plunged into aluminum round bar specimens at a selected feed rate, forcing the processed material radially outwards and thus forming tubes. The grain size measurements indicate significant refinement in the microstructure of the starting material in stir zone. However, the temperature during the process was not measured so its

15

mechanical-thermal history is not clear and microstructure evolution cannot be interpreted.

Different die rotational speeds and travel speeds were tried by Hosseini et al. for studying the effect of process parameters on the physical properties of AA2025 friction extruded wires[29]. Appropriate parameters for AA2025 were presented by comparing the surface defects on wires. Bad surface finishes were inspected and classified into hot crack and channeling effect. Further studies like texture of wire and material flow undergoing different parameters are necessary to carry on. With similar concepts, Joshi et al. proposed a technique of torsional shear assisted indirect extrusion process (SAIE) uses a rotating ram as opposed to the axially fed ram used in the conventional indirect extrusion process[30]. This work has shown that by using optimized high shear deformation and second phase particles of Mg_2Si and Mg_xZnZr_y the energy absorption of the extrusions can exceed that of AA6061. It also demonstrated significant promise with regards to tailoring the microstructure and is readily scalable to produce large parts relevant to automotive applications.

Although limited research has been done on friction consolidation and extrusion process, there is knowledge from related studies that can benefit our understanding and is worthy of referencing. Sato et al. discovered relationship between control parameters and grain growth in friction stir welded samples[31]. His study indicated that higher heat input which brings about high temperature causes grain growth and consequent hardness drop. This is helpful to understand similar microstructure evolution during friction extrusion

process. High pressure torsion (HPT) is another metal forming process having aspects in common with friction consolidation and extrusion. It refers to the processing of metals whereby samples are subjected to a compressive force and concurrent torsion in the quasi-static state[32]. The strain in HPT process can be easily calculated and may be helpful to estimate the strain in friction consolidation and extrusion process.

2.3 Conventional manufacturing methods

In this section, several conventional manufacturing processes will be reviewed and discussed. Their advantages and disadvantages will be elaborated. The comparison will be made between them with friction consolidation and extrusion process.

2.3.1 Powder Metallurgy

Powder metallurgy is a process of producing useful components parts from metal powders by pressing and simultaneous or subsequent heating to produce a coherent mass. The conventional powder metallurgy process consisted of three operations: powder blending and mixing, powder pressing, and compact sintering. Blending and mixing ensure the unpacked ingredients are homogeneous so that finished product will be uniform. Lubricants are added before mixing to reduce friction and minimize die wear. Pressing usually called as green compact which consists of filling a die cavity with a controlled amount of blended powder applying the required pressure, and the ejecting the as-pressed compact. Basically, this step is performed at room temperature. The pressure is varied by

17

both material and target density to be achieved. The strength and density of compacted powder increase with pressure due to interlocking and plastic deformation. Along with increasing pressure, density reaches its plateau by work-hardening and friction. Also, density decreases with increasing distance from pressing die surface. It is very difficult to reach full density. The last step, sintering, involves heating compacted powders in a controlled-atmosphere furnace to a temperature that is generally slightly below the melting point of the powder metal. It can produce strong bonding between powder particles, make chemical, dimensional or phase changes, and alloying if mixed elemental powders were used. Temperature, time and atmosphere are the most critical parameters in sintering. Temperature depends on what material is used. Proper sintering time ranges from 30 minutes to several hours. Commonly used atmosphere includes carbon monoxide, hydrogen and cracked ammonia.

There are many commonalities between powder metallurgy and friction consolidation process and a few differences as well: Firstly, they both start from finely divided precursors and end up with a finished part. Beyond powder metallurgy, friction consolidation deals with not only metal powder but also metal wastes like machining chips. The surface finish of friction consolidated production may not as good as the part made by powder metallurgy. Secondly, great pressing force is required for achieving high density production. Thirdly, the high temperature is the key of bonding pieces together in both processes. Fourthly, they both offer high material utilization efficiency because almost no

scrap is lost. A major difference between them is friction consolidation is a one-step process. Mixing, compacting and bonding almost happen together because the die is rotating with pressing force and the accompanying plastic deformation lead to heat dissipation and temperature rising. Blending tool, lubricants, furnaces and special sintering atmosphere are not required. This means friction consolidation process can save considerable time, labor, devices and space relative to conventional powder metallurgy. Also, the requirement of the quality of precursor for friction consolidation is not as strict as powder metallurgy. Metal scrap like machining chips and dust are eligible for friction consolidation even if their sizes are highly uneven. So, a further saving of material can be made. However, it has to be mentioned that the production of powder metallurgy parts is more precise and there is no need for further machining.

2.3.2 Extrusion and wire/rod drawing

Conventional extrusion involves forcing a billet through an opening die whose exiting hole is smaller than entering hole, see Figure 2 [33]. The shape of the cross-section of the extruded metal will conform to that of the die opening. Nonferrous metals and alloys like copper, brass, aluminum, zinc, and magnesium are friendly material for extrusion but other metal can also be extruded when proper lubricants and devices are applied. Extrusion can be classified into two types: cold extrusion and hot extrusion. The latter one is prepared at elevated temperature prior to each extrusion cycle. There are four types of extrusion:

Direct extrusion, indirect extrusion (or back extrusion), hydrostatic extrusion, impact extrusion.
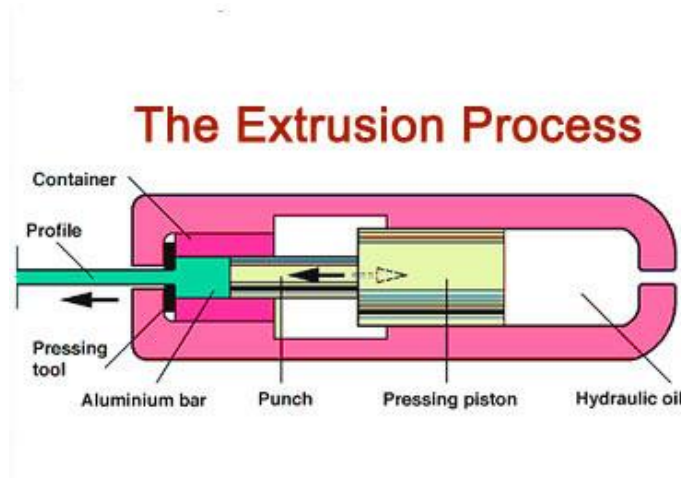
Figure 2.2 Conventional extrusion process

The biggest difference between conventional extrusion and friction extrusion is the die rotation is involved in latter one. Except this, there are many concepts and definition can be used in both processes. Therefore, it is significant to review them and specify the commonalities and differences.

The extrusion ratio, R, can be defined as

$$R = \frac{A_o}{A_f} \qquad\qquad \text{Eq (2.1)}$$

Where A_o is the cross-sectional area of initial billet and A_f is the cross-sectional area of the final product. The complexity of an extrusion is described by shape factor, which is the ratio of the perimeter of the part to its cross-section area. For a round rod or wire extrusion, the shape factor is 2/radius, which is the lowest shape factor. These two

parameters can be used in friction extrusion also. But so far only round wire has been tried in friction extrusion process.

Based on extrusion ratio, the true strain can be written as:

$$\epsilon = \ln\left(\frac{A_o}{A_f}\right) = \ln R \qquad\qquad \text{Eq (2.2)}$$

For a perfectly plastic material with a yield stress Y, the ideal force without considering friction can be written as:

$$F = A_o Y \ln\left(\frac{A_o}{A_f}\right) \qquad\qquad \text{Eq (2.3)}$$

For hot extrusion, because of the strain-rate sensitivity of metal at elevated temperatures, it is difficult to calculate extrusion force accurately.

The defects in extrusion and wire drawing are of three principal types: The first one is surface cracking. If the extrusion temperature, speed and friction are too high, the surface temperature can rise significantly and cause local incipient melting. This phenomenon will lead to surface cracking and tearing. It can be avoided by using lower temperature during the process. Surface cracking can also occur at low temperature due to periodic sticking of the extruded product along the die land during extrusion. The second type is called extrusion defect. The reason is attributed to a large shear dead zone which is due to high container-wall friction. In this situation, the material near the container walls cools rapidly, whereby the material becomes stronger. As a result, the material in the central regions of the billet flows toward the die more easily than that at the outer regions. A large dead metal zone then forms and the flow is inhomogeneous. This kind of defect can be avoided by

21

modifying the flow pattern or machining the billet surface prior to extruding to eliminate impurities. The third defect is the internal defect which also well-known as chevron cracking. It is attributed to a state of hydrostatic tensile stress at the centerline of the deformation zone in the die. To avoid this situation, die angle and contact length should be picked properly. In friction extrusion, the material close to die tip was in plastic state before being extruded out. So there is negligible friction between material and chamber. The second and third defect are avoided in friction extrusion.

2.3.3 Aluminum recycling

While quantification of deformation levels in friction extrusion has not been published, there is some related work in the literature. Direct recycling of aluminum chips via hot extrusion was first proposed and patented by Stern [34]. Gronostajski and Matuszak [35] comminuted and compacted aluminum chips followed by conventional hot extrusion. This solid state process avoids the formation of thick oxide skin so the scrap can be converted to a finished product without further processing. The process was also used for the development of novel alloy compositions based on the blending of multiple alloy particulates. A Recent study indicates that high quality extrudates can be produced when appropriate die design criteria are satisfied [36]. Tekkaya et al. [37] show that the pre-compaction step is not important when minimum stress, strain, and temperature conditions are achieved for creating metallic bonding between chips. M. Haase et al. [38] use the

integrated equal channel angular pressing (iECAP) die instead of the flat-face or the porthole die as a tool for solid state recycling of aluminum machining chips. Since additional shear deformation and strain are introduced, improved chip bonding and superior strength and ductility are achieved. McDonald et al.[39] also use ECAP to recycle Ti-6Al-4V machining chips to produce fully dense bulk material. Compared with commercial Ti-6Al-4V, better mechanical properties are achieved after mill-annealing treatment. Güley et al. [40] Studied the welding quality of using flat-face die and porthole die via conducting experiments and numerical simulation. The bonding criteria of chips and the breakdown mechanism of oxide layer were established. The welding quality index (WQI) related to normal pressure and effective stress has been proposed. Cooper and Allwood [41] Reviewed previous theoretical and experimental work on solid bonding. The summation of experiments shows that a minimum strain is required for bonding. Increasing the temperature, normal contact stress or shear stress can reduce this required minimum strain. A normal contact stress above the materials' uniaxial yield stress is necessary to produce a strong bond. Haase and Tekkaya (Haase and Tekkaya 2015) further processed hot extruded chips by backward can extrusion or forward rod extrusion. By comparing the microstructure and result of mechanical tests, it was shown that the deformation route during hot extrusion is critical to high quality finished products. Duflou et al. [43] discussed the significant environmental impact reduction associated with solid state recycling

processes. 4% less material loss were documented for screw extrusion when considering average industrial material loss fraction.

Using a principle similar to that of friction extrusion, a testing machine using combined pressure and shear to granulate and recycle aluminum was built by Widerøe et al. [27]. Their results indicated that the shear deformation greatly reduced the axial force required for compacting aluminum scrap. Also, they showed that the number of revolutions of the tool influences deformation penetration depth and mixing range. Since limited experimental parameters were used, the relationships between control parameters and process responses such as material flow pattern and microstructure were not determined. Widerøe and Welo [44] observed spiral core path as a possible material flow path in screw extrusion. Their result indicates that the highest rate of material flow was found in the center of screw channel and dead metal zones were located at the bottom of the screw channel and toward the container wall.

The above studies show that extrusion at high temperature is not only an economical avenue to recycle aluminum chips but also a route to produce high quality finished products. Compared with traditional hot extrusion, friction extrusion requires considerably smaller extrusion force to produce high deformation and strain. Also, chamber preheating is avoided, so energy, time, and capital can be conserved.

2.4 Wire based additive manufacturing

2.4.1 Introduction

This section introduces the basic concept and the history of wire based additive manufacturing, especially Wire and Arc Additive Manufacturing (WAAM). The knowledge of arc welding process is also reviewed since WAAM uses arc welding as a heating source. Particular attention is focused on the thermal modeling of the welding process and WAAM process. The advantage and disadvantage of these models are discussed and summarized.

2.4.2. Wire based additive layer manufacturing

Additive manufacturing (AM) was considered as top 10 breakthrough technologies in 2013 for its vast utilities from fabricating meticulous artificial organs for medical purpose to producing critical jet engine parts in aerospace industry. This technique not only makes complex parts quickly and precisely but also lower cost through saves considerable material and labor. The mainstream AM technologies can be classified by the type of heat sources, such as Electron Beam Fabrication (EBF), Laser Melting (LM), Ultrasonic Additive Manufacturing (UAM), Plasma Deposition (PD), and Gas Metal Arc Welding (GMAW) etc. Wire and power are the two mostly used precursor form.

Comparing with powder-based additive manufacturing, wire-based additive manufacturing process gained some attention because of its higher deposition rate and

higher producing efficiency[45]. Besides, it doesn't require additional sealing chamber for

reserve powder. Syed and Li studied the deposition of metallic wire with high power diode

laser on mild steel[46]. Mok et al. applied same technique on Ti-6Al-4V[47], [48].

Components with good integrity were fabricated using this process. The Electron Beam

Freeform Fabrication (EBF3) layer additive manufacturing process was proposed by

NASA Langley Research Center to build near-net-shape parts requiring less raw material

and finish machining than traditional manufacturing methods[49]. It uses an electron beam

as a heat source and solid wire as feedstock. Domack produced aluminum alloy 2219

components [50] and Brice fabricated Ti alloy parts[51] by EBF3.

WAAM combines conventional low energy input welding process like Metal Inert

Gas (MIG) and Tungsten Inert Gas (TIG) with wire feeding. Among the different AM

processes, WAAM has the ability to manufacture large, low volume metal workpieces due

to its high deposition rate. In this process, 3D metallic components are built by depositing

beads of weld metal in a layer by layer fashion[52]. The fast deposition speed and high

deposition rate enable it to produce large-scale components for aerospace and aeronautical

industry.

The predecessor of WAAM is proposed and firstly patent by Baker in 1920[53].

Modem automation technologies and robotic welding provide it more precise control on

geometry and process temperature. In 1990, Schmidt used shape welding to build

components for a large reactor coolant system[54]. It proved possible with this

manufacturing technique to fabricate an item complying dimensionally and metallurgically with the specifications in a relatively short time. Ribeiro and Norrish developed an automated additive manufacturing called Shape Metal Deposition (SMD) [55], [56]. This technique realized fast prototype a CAD drawing model using welding robot and conventional MIG power source[57]. What's more, the welding parameter for a designed geometry can be calculated by the program. Spencer et al. fabricated free-standing parts and improved surface finishing using temperature control[58]. Muscato et al. implemented video feedback algorithms to fully automatically control SDM system[59]. In 2010, Cranfield University, UK designed wire and arc additive manufacturing for manufacturing efficiently complex geometries[60]. Ti-6Al-4V wall samples made with WAAM were tested by Baufeld et al. for analyzing microstructure and mechanical properties[61]. Results showed its mechanical properties are competitive to cast material and components built by other additive manufacturing techniques. Wang et al. showed it is very necessary to minimize or diminish wire contamination for producing a defect free wire[62]. Cong manufactured aluminum alloy wall samples via WAAM and studied effort of arc mode in cold transfer process on the porosity characteristic[63]. He pointed out that fine equiaxed grains microstructure of wire is the key to porosity elimination.

2.4.3 Simulation on WAAM process

In order to better predict the thermomechanical properties of WAAM parts and to achieve better controlling on the process, analytical solution and finite element models of welding are introduced. In 1946, based on empirical studies Rosenthal derived an analytical solution of heat transfer in the moving heat source welding process[64]. It gives an accurate prediction on the region where the temperature is 20% lower than the melting point but error on fusion zone and heat affected zone. In1984, Goldak et al. developed a non-axisymmetric heat source model in which power density is dispensed with a Gaussian distribution in a double ellipsoid[65]. Goldak's double ellipsoid heat source model is flexible to fit different welding processes by adjusting the parameters in the model. Many works were developed based on this model. In 1992, Brown and Song applied finite element simulation of welding of large structure[66]. The thermal analysis considered temperature dependent material properties, including latent heat and nonlinear heat convection and radiation boundary conditions. In 1997, Michaleris and Debiccari proposed a two-step numerical model to predict welding distortion[67]. Ding et al. employed a 3D thermo-elastic-plastic transient model and a model based on an advanced steady-state thermal analysis to analyze the thermo-mechanical behavior of the multi-layer wall structure made by the WAALM process[68]. A significant distortion and residual stress are attributed to high heat input. Fawad et al. obtained temperature field in Gas Metal Arc welding (GMAW) metal deposition using heat transfer finite element modeling[69].

28

CHAPTER 3

FRICTION EXTRUSION

3.1 Experimental and testing procedures

3.1.1 Wire made by Friction Stir Welding Process Development System

3.1.1.1 Experimental apparatus and procedure

The friction extrusion apparatus are composed of the following four parts: dies, chamber, back plate and Process Development System. The dimension of the extrusion die is Φ25 mm X 114.3 mm with a through hole at the center, which defines the size of extruded wire, see Figure 3.1. It is interesting to note that the 100:1 extrusion ratio is near the maximum for conventional extrusion of alloys such as AA6061. There are two kinds of die tip pattern: one has a scrolled surface which is similar to a friction stir welding tool shoulder designed for operation at a $0°$ angle of attack. The scroll die is rotated in a clockwise direction (From top view) so that the scroll pattern can gather plastic material toward the center hole. The other die has a flat smooth surface. This flat die is also rotated in a clockwise direction to facilitate comparison with the scrolled die. All dies were fabricated with H13 tool steel. Both die tips are shown in Figure 3.2.

30

Wire extrusion tool for 2.54mm wire
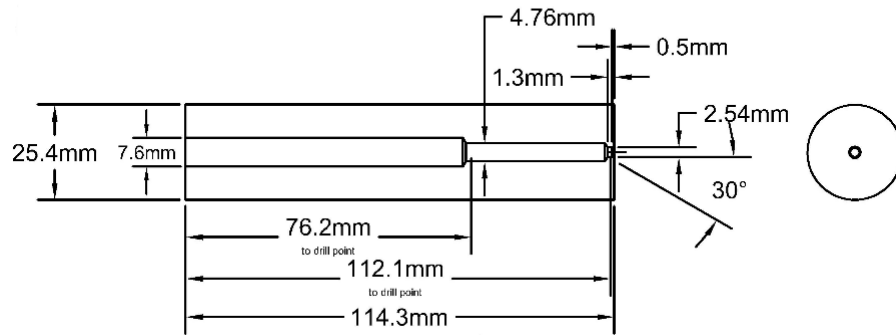
Figure 3.1 Schematic diagram of friction extrusion die for 2.54mm wire

Figure 3.2 Friction extrusion scroll die (left) and flat die tips (right)

Figure 3.3 shows the 'billet' chamber used in the friction extrusion process. The inner diameter of stationary 'billet' chamber is 25.4mm, which is a little bigger than unprocessed AA 6061 cylinder samples and dies. The chamber has a wider shoulder ring outside with two semicircle breaches for being fixed on the back plate. The chambers were fabricated with O1 tool steel.

31

Figure 3.3 Billet chamber used in friction extrusion and consolidation

A stainless steel plate is adopted as the back plate for supporting the chamber and cylinder samples, see Figure 3.4. In order to prevent slipping between the back plate and cylinder sample, a short bar with 4 mm height is set on the back plate inside 'billet' chamber, this prevents the billet charge from rotating.

Figure 3.4 Stainless steel backing plate used in friction extrusion

The FSW PDS (Friction Stir Welding Process Development System) was used to implement the extrusion process, Figure 3.5. Using this machine, the extrusion process is performed under extrusion force control. Unlike conventional rate controlled extrusion

processes, this force control mode can lead to varying die advance speed and extrusion rate.

Because of the limited headspace above the die in the FSW PDS, only a small part of the

aluminum cylinder would be extruded out to form a wire with about 150mm length.

Figure 3.5 University of South Carolina Friction Stir Welding Process Development System
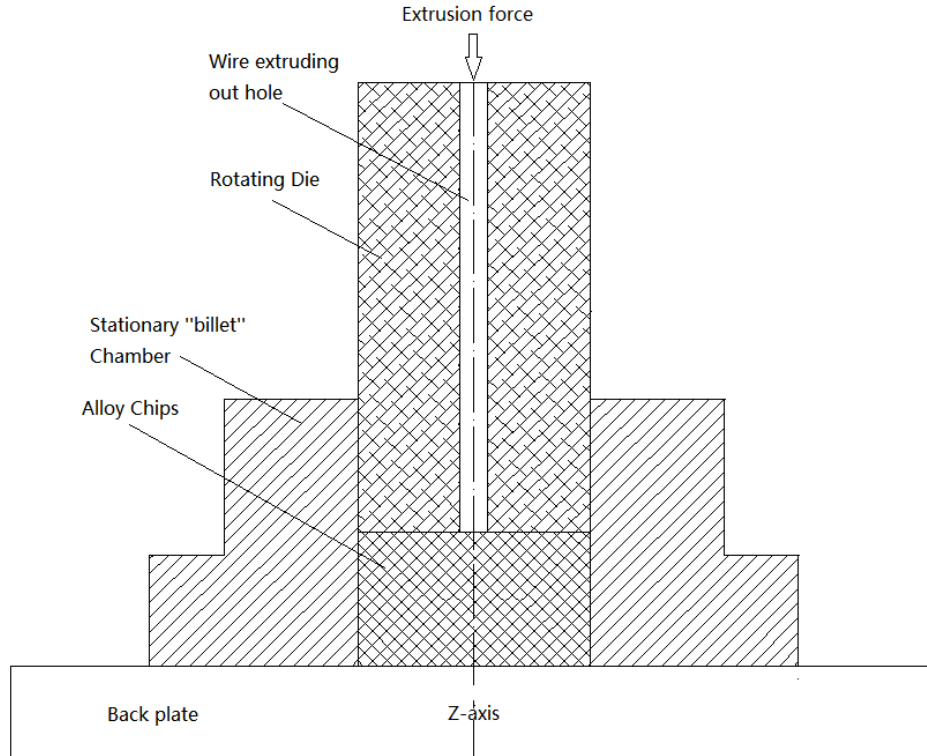
Figure 3.6 Schematic diagram of friction back extrusion

The friction extrusion process using FSWPDS is described as a back extrusion wherein the rotating die is pressed into the billet chamber under load control and the wire is extruded up through the central hole in the die, see Figure 3.6. The experimental procedure is described as following: the first step in setting up for extrusion is to shift the die right above of the chamber containing the sample and make sure Z-axis of the machine is coincident with the extrusion axis: hence the Z-force is equivalent to the extrusion force. Move the die down until it contacts with the sample, and then start to spin the die. The heat generated by the friction between the die and aluminum charge increases the temperature immediately. As a result, aluminum alloy close to die tip is turned into plastic state and

34

will flow. With the downward pressure and heat input, aluminum cylinder expands towards

the chamber wall to fill in the small gap (~0.4 mm) between the sample and chamber. When

sufficient temperature is reached aluminum enters the center hole and the wire starts to

extrude out. In this friction extrusion processes, the die rotation speed, die position and Z-

force (extrusion force) were recorded by the FSW system control computer with 10Hz

sampling rate. The rotating torque and power were recorded by a torque transducer

mounted on the machine spindle (which drives the die rotation): these data were recorded

with at least 40Hz data collection rate.

3.1.1.2 Material flow study

To visualize material flow and redistribution of friction extrusion process, marker

insert technique (MIT) is adopted to prepare special precursor samples. In this study,

AA2195 (Al–4.0Cu–1.2Li–0.4Mg–0.4Ag–0.12Zr) wire was adopted as a marker material.

A precipitate hardening alloy, AA6061 (Al-1.0Mg-0.6Si-0.6Fe-0.25Cr-0.2Cu), that is

commonly used in automobile and aerospace structures was used as the billet. Its good

weldability in friction stir welding has been widely accepted so it is picked as precursor

material in friction extrusion. The chemical composition difference between marker

material and billet material enable the two materials to be distinguished by etching[70].

Hot deformation flow stress data from Gleeble testing indicates that at relevant

temperatures, the flow stresses of the marker and parent material are quite similar[71].

Figure 3.7 is a plot of flow stress vs. temperature for AA6061 and AA2195 at a strain rate

of 0.3 s-1. At low temperatures, the flow stress of AA2195 is significantly higher than that of AA6061 but, the flow stress of the AA2195 declines more rapidly with increasing temperature than does that of the 6061 and as temperature approaches relevant hot-working values, the flow stresses of the two alloys become quite similar.
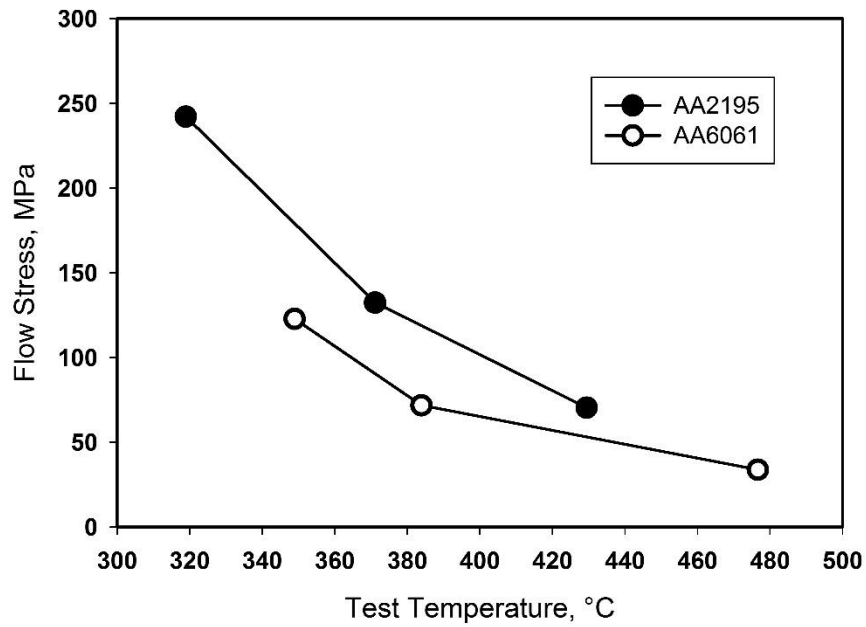
Figure 3.7 Elevated temperature flow stress of the marker and parent alloys.

In this study, $\Phi 25$ mm X 19.2 mm AA6061 aluminum alloy cylinder is adopted. All cylinders were drilled through from the top surface to bottom. AA2195 aluminum alloy wire with $\Phi 2.54$ mm X 19.2 mm was fully embedded into the drilled hole to substitute a part of the AA6061 cylinder. Each cylinder has a sole AA2195 wire segment which was located in different positions: Center of the cylinder (0r for short), 1/3 cylinder radius far from center (1/3r), 2/3 cylinder radius far from center (2/3r), respectively, see Figure 3.8.

36

Therefore, the material flow of the corresponding region can be analyzed by etching in post-extrusion. Beside die with 2.54mm hole size, dies with 2mm, 1mm and 0.5mm hole size were also tried to verify extrudability and provide more information about material flow. All these dies have same length and diameter as shown in the last section. In all runs, consistent experimental parameters are used: die rotational speed is 300 *RPM* and extrusion force is 44500 *N*.

Figure 3.8. AA6061 Cylinder Samples with AA 2195 marker in center, 1/3 radius, 2/3 radius position respectively

3.1.1.3 Parameter study

The experimental parameters (extrusion force and die rotational speed) play critical roles in friction extrusion process. Extrusion force affects extrusion rate and thus material flow. Die rotational speed is related with temperature and also extrusion rate and material flow. Surface finish is also influenced by processing temperature. Hot crack and cold tear defect appeared on wire surface using either too high or too low die rotational speed[72]. With current understanding on proper experimental parameters window and considering machine capability, 3 different rotating speeds combining with 3 different Z-forces were

selected for a series of extrusion runs to better discover the effect of the control parameter (extrusion force and die rotational speed) on product and material flow. Both of scroll die and flat die was adopted respectively, see Table 3.1. Marker material was placed in 1/3 radii position for each billet in these experiments.

Table 3.1 Adopted friction extrusion parameters in parameter study (SD: Scroll die; FD: Flat die)

rpm	200	300	400
Z-force(N)			
22250	FD	SD, FD	FD
44500	SD, FD	SD, FD	SD+FD
66750	FD	SD, FD	FD

3.1.1.4 Temperature measurement

To better understand the mechanism of friction extrusion process and contribute to the creation of a scientific knowledge base for this novel process, a three-dimensional computational fluid dynamics (CFD) model of friction extrusion process has been established[73] by a co-worker for studying the material flow and strain rate. In order to help modeling and verify simulation results, transient temperatures have been measured and recorded in several locations during the process. K-type thermocouples were placed at eight locations on the die, chamber and back plate. The layout of locations of the thermocouples is shown in Figure 3.9.
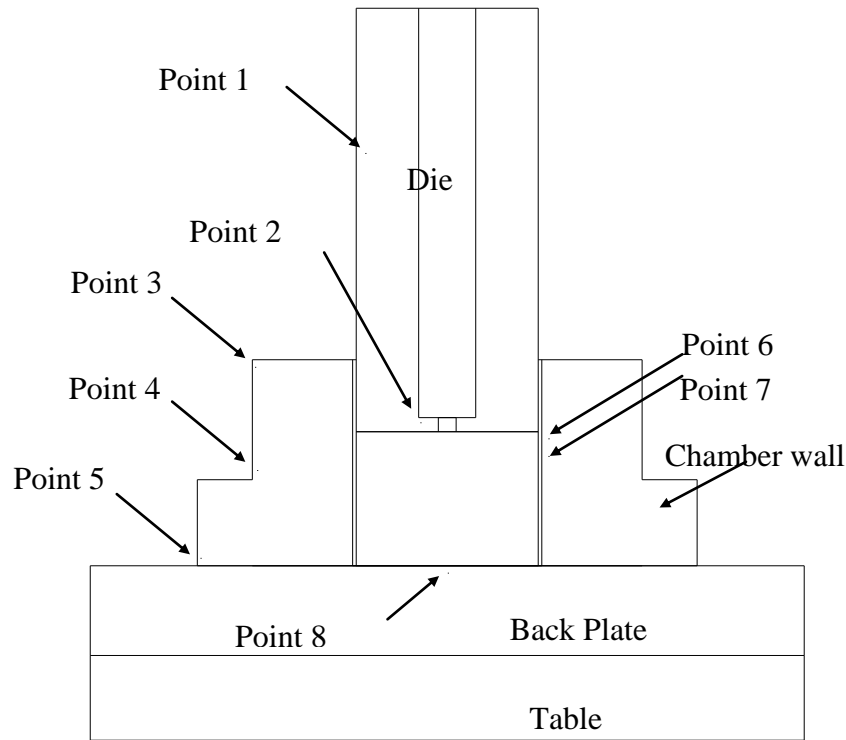
Figure 3.9 Layout of thermocouples on friction extrusion devices

Two thermocouples were placed on the tool die, one is attached to the outside wall

of middle part of the die (point 1), 54.7mm far from the die extruding surface; and the other

one was embedded inside the die which was 1.27mm far from die extruding surface (point

2). Three thermocouples were placed on the chamber outer surface. They are located at the

top of the chamber, the corner of the chamber shoulder and the bottom of the chamber,

respectively (point 3, 4, and 5). Close to the chamber inner wall, two thermocouples were

placed at 18mm (point 6) and 15.5mm (point 7) far from the back plate respectively.

Correspond to the center of extrusion chamber, point 8 thermocouple was put in the back

plate where 2.35mm far from the top surface. Temperatures at point 1 and point 2 were

recorded using HOBOware Data logger with 1 Hz collecting rate, and temperatures of the

rest locations were recorded using Labview software on a PC with 2.4 Hz frequency.

3.1.1.5 Post-extrusion analysis

Since the configuration of the FSW PDS machine confines the length of aluminum

wire, only upper part of the cylinder has been extruded out. Meanwhile, pressed and stirred

by the spinning die, some aluminum was squeezed up through the gap between the die and

chamber. After the friction extrusion, the remnant cylinder became a deformed disk in the

chamber. By analyzing the deformation of the disk and tracking the distribution of marker

material, AA 2195, the flow pattern of material can be determined.

The wire extruded by the FSW PDS was about 150mm long, and it was cut into 6

segments of approximately 25 mm each. Each aluminum wire segment was mounted in

epoxy so that transverse cross sections could be observed. The transverse cross-section of

every segment was ground, polished and then etched with Keller's Reagent (190ml water,

2ml HF, 3ml HCl, and 5ml HNO_3). The distribution of AA2195 marker in the 6061 wire

cross sections was examined by optical microscopy. The remnant disk was carefully

removed from the chamber and necessary machining was applied on the top side to form a

flat and smooth surface. After that, it was ground and polished. Keller's Reagent was

applied on the machined surface. With the etchant chemical attack, AA2195 turned dark

but AA6061 remained the bright. Pictures were taken by an optical microscope and by a

flatbed scanner. Furthermore, multiple grinding, polishing, etching and imaging procedures

were applied to expose successive layers of the disk with each layer being 0.25mm thick. Hence, deformation and flow pattern at different height were obtained (a form of mechanical tomography). By assembly of all pictures in sequence of height, a three-dimensional image of the marker positions was established. Therefore, the material deformation/flow before entering into the extrusion die hole can be observed.

3.1.2 Wire made by modified milling machine

3.1.2.1 Experimental apparatus and procedure

Because of the headspace limitation of FSWPDS, a modified C-frame milling machine with hollow drawbar was employed for the extrusion process, as shown in Figure 3.10. The hollow drawbar enables the extrusion of wires come out from the top of the machine. The spindle of the milling machine was used to rotate the die while a hydraulic cylinder mounted on the knee was used to drive the billet chamber charge into the spindle. Hence, this was a force controlled extrusion somewhat analogous to forward extrusion with a rotating die. Under frictional heat between die face and billet, billet material was elevated close to solidus temperature and softened. After being compressed into central extrusion hole, material cooled down quickly and form a wire as shown in Figure 3.10. The milling machine was not instrumented: the rotation rate was set by gear selection and the extrusion pressure was determined by setting the hydraulic pressure on the ram by adjustment of a

41

pressure regulator (the maximum hydraulic power supply pressure was 21 MPa). Three

hundred RPM was used as die rotational speed.
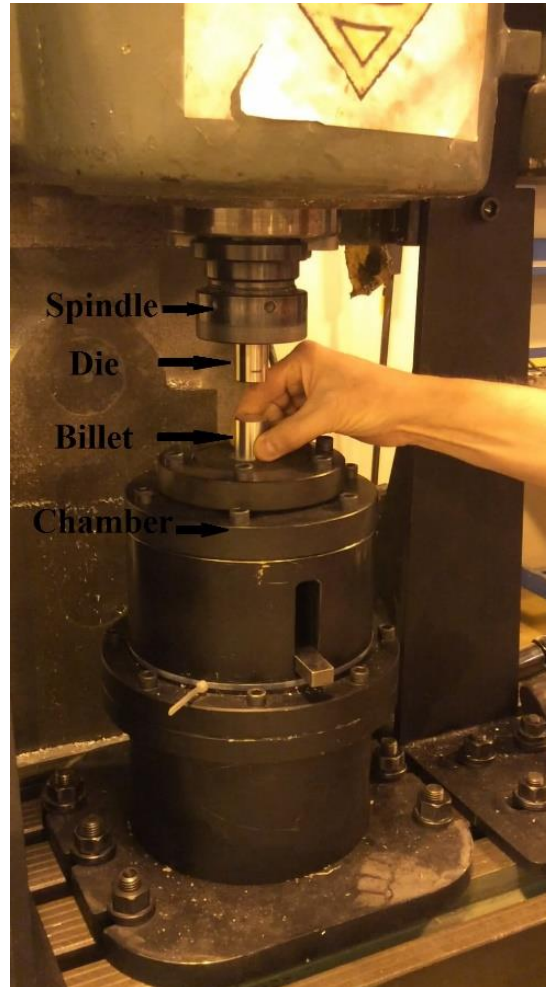
Figure 3.10 Experimental setup of friction extrusion using modified milling machine
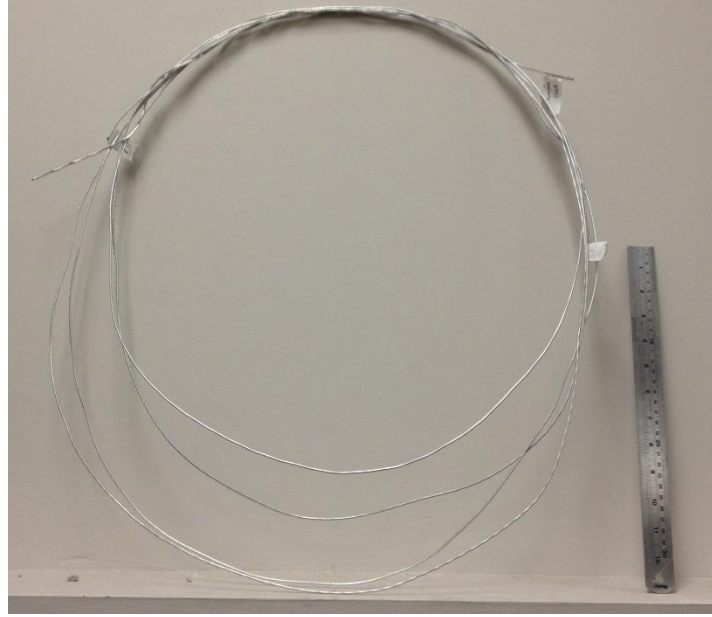
Figure 3.11 Friction extrusion wire made with modified milling machine

The length range of extruded wire is from 1.7 m to 2.3 m, as shown in Table 3.2.

These wires were cut into several segments, each approximately 300 mm long. Portions of

each wire segment were mounted in epoxy so that transverse and longitudinal cross

sections could be observed. The cross-sections were ground, polished and then etched with

Keller's Reagent (190ml water, 2ml HF, 3ml HCl, and 5ml HNO_3). The distribution of

AA2195 marker in the AA6061 wire cross-sections was determined by optical microscopy

and used to qualitatively visualize material deformation and to semi-quantitatively

determine the strain at various stages of the extrusion. The grain size of the AA2195 marker

wire in the extruded material was measured using the mean linear intercept (MLI)

method[74].

3.1.2.2 Material flow study

For visualizing material flow and deducing strain, marker study experiments are also performed. A 25.0 mm diameter by 38.1 mm long AA6061 cylinder was used as the extrusion billet and 2.4 mm diameter AA2195 wire was used for the flow marker. A single through thickness hole was drilled in the AA6061 billet at a 1/3 radius location and a segment of AA2195 wire was embedded in the hole Figure 3.12. The AA2195 wire had been previously produced by friction extrusion from AA2195 machining chips. The die rotation speeds and extrusion forces used are shown in Table 3.2.
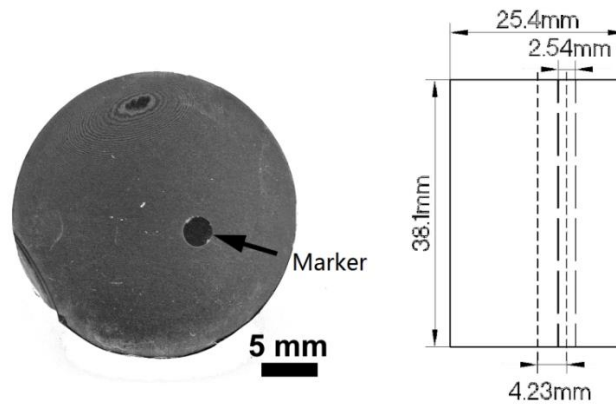
Figure 3.12 AA6061 cylinder sample with AA2195 marker in 1/3 radius position

Table 3.2 Extrusion parameters and resulting wire lengths.

No.	Rotational speed (RPM)	Maximum Extrusion force (kN)	Wire length (m)
1	300	106.8	2.30
2	300	80.1	1.68
3	400	106.8	2.19
4	400	80.1	1.83

3.1.2.3 Electron backscatter diffraction

The texture of wire from extrusion No.1 in Table 3.2 was analyzed using electron backscatter diffraction (EBSD) at NASA Langley research center. Three samples from different points along the length of the extruded wire (76 mm, 990 mm, and 1840 mm from the first part extruded) were examined using EBSD. Prior to EBSD, these samples were prepared on a precision, automated mechanical polishing system. Samples were polished on a plane normal to the extrusion direction using 1200 grit SiC paper for approximately 5 minutes, followed by a final polish with 0.05 μm colloidal silica for 20 minutes. The samples were then examined in a scanning electron microscope with a tungsten filament at an accelerating voltage of 20kV, a probe current of 2nA and a sample tilt angle of 70 °. All data was collected using a step size of 1 μm. EBSD data was initially collected in 300 μm wide strips across the diameter of each of the three samples. Texture analyses included standard inverse pole maps and pole figure plots. All texture data were referenced with the normal direction, ND, in the extrusion direction. The MLI technique was used to measure the 6061 grain size on the grain maps produced from EBSD: both the 2195 marker material and several observed regions of abnormal grain growth (AGG) were excluded from this grain size measurement.

3.1.2.4 Post-extrusion drawing and annealing

Because of the limitation of current equipment, the longest wire that can be made is about 3 meters. That's not long enough to be used as filler wire in either welding or

additive manufacturing. Besides, due to rotating during hot forming in friction extrusion process, the as-extruded wire is twisted and not strictly round shape. Also, the beginning and end of wire have some surface defect caused by cold tear and hot cracking. To overcome these disadvantages, using a die with large extrusion hole and post-extrusion drawing were proposed to make a smooth round wire with considerable length.

For conducting post-drawing and annealing experiments, AA2050 has been used as billet material. The reason that picking AA2050 is because it is another aluminum alloy widely used in aeronautical industry and wire made from AA2050 may be an attractive precursor for WAAM processes. The chemical composition of AA2050 is listed in Table 3.3[75].

Table 3.3 Chemical composition of AA2050

Wt.%	Si	Fe	Cu	Mn	Mg	Zn	Li	Ag	Zr	Al
Min			3.2	0.2	0.2		0.7	0.2	0.06	balanced
Max	0.08	0.1	3.9	0.5	0.6	0.25	1.3	0.7	0.14	

Firstly, the 2.54mm hole die was adopted to validate extrudability. In order to prevent overheating during the process, lower RPMs, 200, were used. Then, post-extrusion drawing was introduced to reduce wire diameter to desired size and improved surface quality of the wire. A simple drawing bench was assembled which consists of a hand winch, belt, plier hook and stainless steel draw plate with multiple hole sizes, see Figure 3.13 and Figure 3.14. A cutting lubricant was used during drawing to reduce drawing force but it is not optimized. A Φ2.54mm friction extrusion wire was successfully produced firstly.

Because it was slightly twisted so its transverse cross-section is not perfect round, the first

drawing used 2.7mm hole as a start. Then, the wire was drawn from 2.7mm to 1.6mm with

15 drawing steps, 0.1 mm step size.
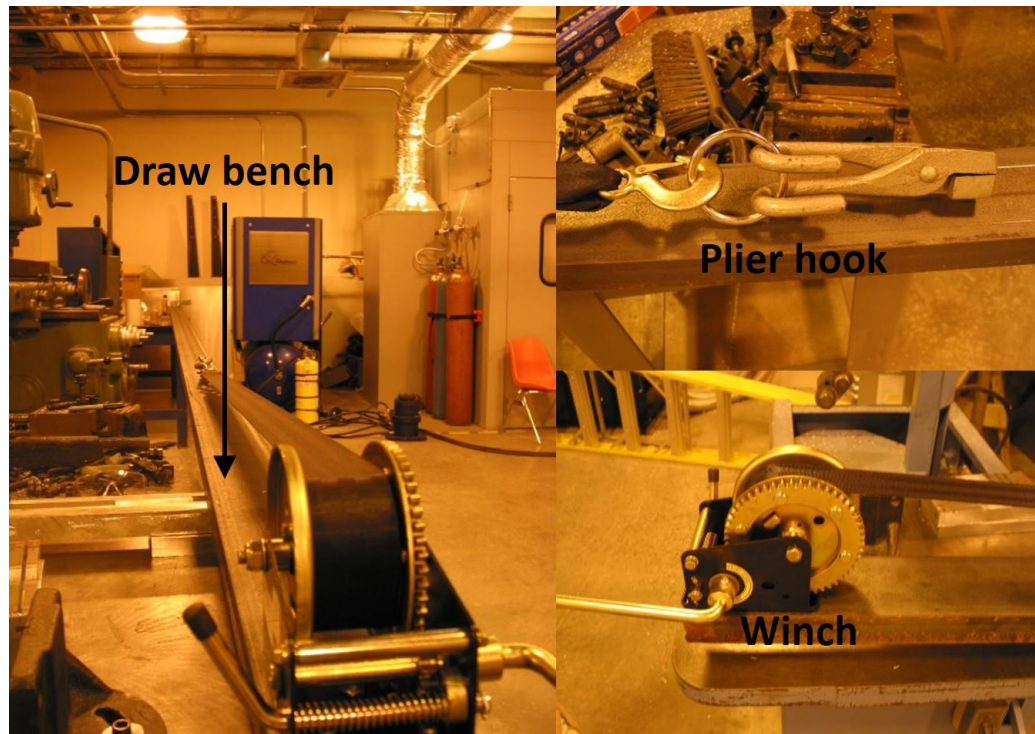
Figure 3.13 Drawing bench, winch and plier hook used in post-extrusion drawing
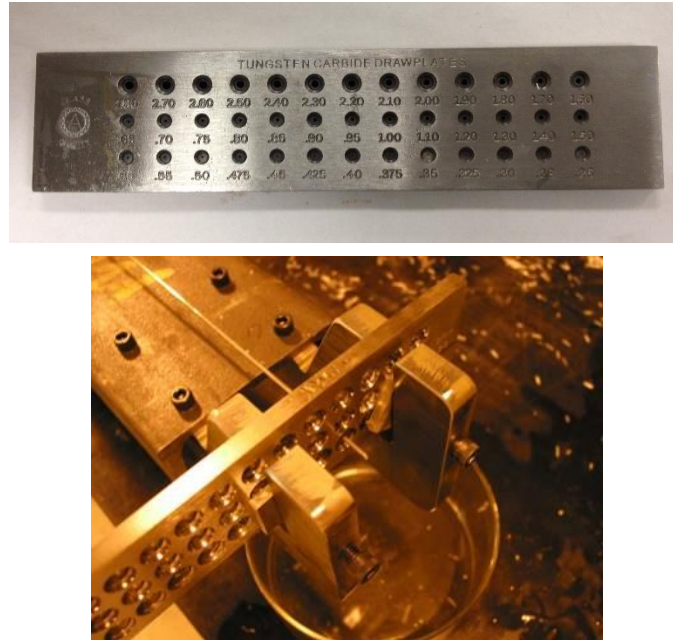
Figure 3.14 Draw plate with multiple size holes

After each drawing, wire loses ductility due to cold work. In order to diminish strain hardening and prevent breaking in new drawing step, annealing was done by an oven (Figure 3.15) at 350℃ between several draws. After annealing and the following drawing step, reannealing was applied with the same temperature of annealing. To study the effect of annealing and re-annealing heat treatment on the microstructure and hardness of AA2050. Different annealing and re-annealing time: 5 mins, 10mins, 15mins, 30mins, 45mins, 60mins were used. Wire sections were cut off in as-made, as-drawn and annealed conditions. Then, they were mounted, ground, polished, etched and inspected by an optical microscope, so the microstructure was revealed. Vickers hardness test was performed on the transverse cross-sections for testing strength.

Figure 3.15 Blue M conventional oven used in wire annealing

Dies with smaller hole diameters were tried to make a wire with proper diameter and longer length that can be directly used as filler wire for downstream processes like welding or additive manufacturing. 1.8mm, 1.6mm and 1.2mm have commonly used diameter of welding filler wire and wire and arc additive manufacturing filler wire as well. So die hole with these diameters were adopted. Lower RPMs 150 and 115 were used to avoid over-heating. Besides, because billet size is constrained by chamber capacity, dies with larger diameters, 4 to 6 mm, were introduced to make a rod first which is not easy to be break. Then, they were drawn down to the desired size and stretched longer at the same time.

3.2 Results and analyses

3.2.1 Wire product and process progress analysis

The AA6061 wire made by FSWPDS is about 160mm long, shown in Figure 3.16. In this picture, the left end is the first extruded part, the right end is the last extruded part. The surface of the wire is clean and smooth. No obvious surface defect was observed. Due to the rotating feature of friction extrusion process, the wire was twisted and curved. It passed 5T bending test which indicates it has good bend ductility.

Figure 3.16 AA6061 wire made with friction extrusion, 300 RPM die rotational speed, 44500*N* extrusion force.

Figure 3.17 shows the typical process parameters responds in friction extrusion using aluminum chip as precursor. The process can be divided into two regimes at about 20s after die starts rotating. Before 20s, aluminum chips was largely compressed and then consolidated. Firstly, die rotation speed soared to 250 RPM in about 3 seconds. From 3 to 12 seconds, die pushed down rapidly until Z-axis load reached desired value. Then, the friction between aluminum chips, rotating die and chips themselves generated local plastic deformation and consequential heat. Along with increased temperature and severe plastic deformation, chips were kind of "welded" together and thus, consolidation happened. After

50

20s, under steady high compressive force and torque, more material involved and generated more plastic deformation further and produced a great amount of heat. The flow stress of aluminum alloy decreased to a low value as a result of elevated temperature. The upper aluminum alloy which was near die tip turned into highly mobile plastic state quickly. The portion located close to extrusion hole exited first. The extruded material left the heat source before melting and cooled quickly. It was confined by die hole and consolidated to form a wire. Thereupon, die gradually moved downward and adjacent material replenished, deformed, got heated up and softened, finally extruded out as well. Such balance continued and wire product was produced.
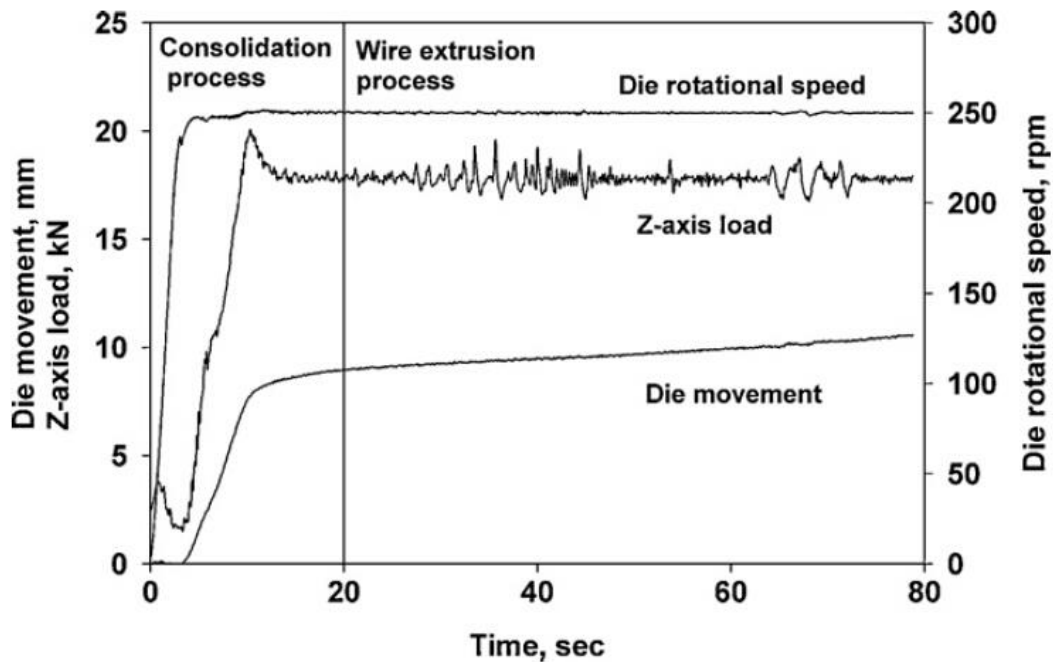
Figure 3.17 Processing parameters feedback in friction wire extrusion[72]

3.2.2 Material flow

AA2195 center marker, 1/3r marker and 2/3r marker were used with both scroll die and scroll die. The material redistribution is revealed by etching sectioned remnant discs and cross-sections of wire products. The results are presented as following:

In the remnant disk, only the center marker remained at its original location and retained a circular cross section. Figure 3.18 shows cross sections from the remnant disk of a scroll die extrusion test at 2 mm below the die face. From Figure 3, it appears that the mixing of the AA 2195 marker and the AA6061 was so complete for 1/3 r marker that the marker can't be traced. It was observed from the serial sectioning of the remnant disks that the disks were deformed to a distance of approximately 4 mm from the die face.
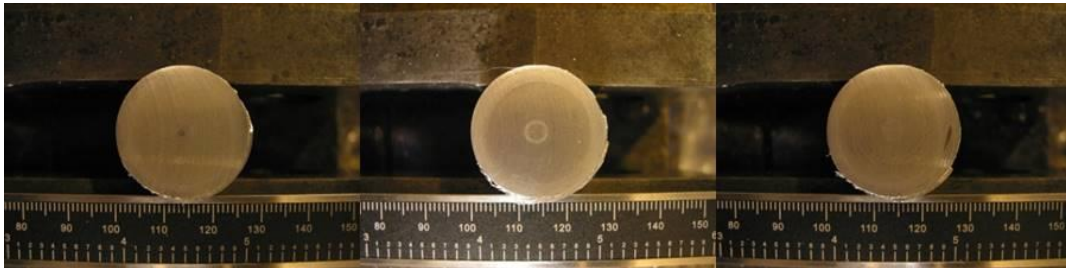
Figure 3.18 Remnant discs cross-sections at 11.9mm height, (left) Center marker, (middle) 1/3 radius marker, (right) 2/3 radius marker

Several binary pictures of different layers in the remnant disc of a flat die extrusion are presented in Figure 3.19. The outside circle is the edge of the remnant disc; the white shapes inside the disc are 2195 marker. The initial stages of deformation process can be deduced from these images.
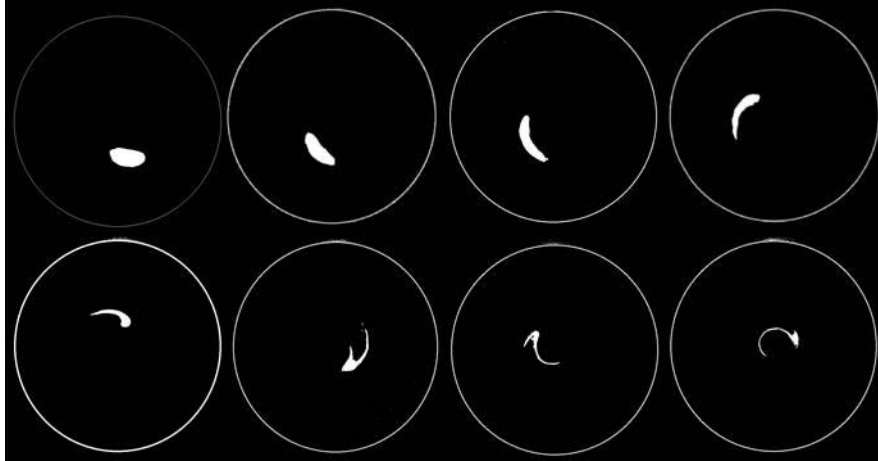
Figure 3.19 Binary picture of 4.30mm, 4.05mm, 3.80mm, 3.55mm, 3.30mm, 3.05mm, 2.80mm, 2.55mm(from left to right, top to bottom) depth of remnant disc

Cross sections of wires extruded using the scroll die with different marker locations are shown in Figure 3.20. As was seen in the remnant disk, only the center marker kept the same location and shape after the extrusion. The diameter of the center marker in the extruded wire was consistently very close to 0.3 mm, about 1/10 of the initial wire diameter and the same as observed at the top of the remnant disk indicating that at the center of the wire, the deformation is similar to that which would be observed in a conventional extrusion. The marker placed at the 1/3 r position was observed to have been deformed into a spiral shape. The minimum spiral radius was 0.44 mm. The width of the spiral arms comprised of the 1/3 r marker is on the order of 5-10 micrometers, which contains about 1 or 2 grain. No obvious evidence of the 2/3 r marker can be observed in the wire.

Figure 3.20 Bottom cross-section of scroll die extruded wire (left) Center marker, (middle) 1/3 radius marker, (right) 2/3 radius marker

Cross sections of wires extruded using the flat die with different marker locations are shown in Figure 3.21. The observed marker patterns are similar to those in the wires extruded using the scroll die. The 0r maker resulted in a 0.28 mm diameter 2195 wire in the 6061 wire center, 1/3 r marker resulted in a spiral pattern, and no evidence of the 2/3r marker can be observed. The only obvious difference between the markers in the scroll die and flat die wires are seen in the disposition of the 1/3r marker wire: the scroll die resulted in a 6 to 7 revolution spiral with 0.44 mm minimum diameter while the flat die resulted in a 2 revolution spiral with 0.32 mm minimum diameter.

Figure 3.21 Bottom cross-section of flat die extruded wire (left)Center marker, (middle) 1/3 radius marker, (right) 2/3 radius marker

The marked wires made using dies with different hole sizes and tip patterns were cut, ground, polished and etched. Their transverse cross-sections are presented in Figure

54

3.22 to Figure 3.27. The markers in 0r marked Φ2mm wires made using flat die remained in the center of the cross-section and generally kept circle shape. The markers in 0r marked Φ2mm wires made using scroll die shows a spiral pattern and strong mixing in the beginning. No clear marker was detected beyond a certain distance from first extruded part. The 1/3r marker in Φ2mm wires made using both flat die and scroll die forms a spiral pattern in cross-sections behind about 40mm from the beginning of wire. No marker was seen in Φ1mm wires made using either flat die or scroll die. For experiments using Φ0.5mm die hole, no marker was found in wires and some of the runs even didn't make a wire due to, it is presumed, the necessary high extrusion pressure. All the results are summarized and presented in Table 3.4. In this table, black dot means circle marker observed on the transverse cross-section, spiral means spiral pattern observed, X means didn't make a wire, / means no maker detected on the cross-section of wire.

Table 3.4 Summary of marker patterns using different hole sizes and die tip

marker position	Flat die, hole size(mm)			Scroll die, hole size(mm)			rpm	Z-force (N)
	2	1	0.5	2	1	0.5		
0r	.	.	X	⊚	⊚	/	300	44500
1/3r	⊚	/	/	⊚	/	X		

55
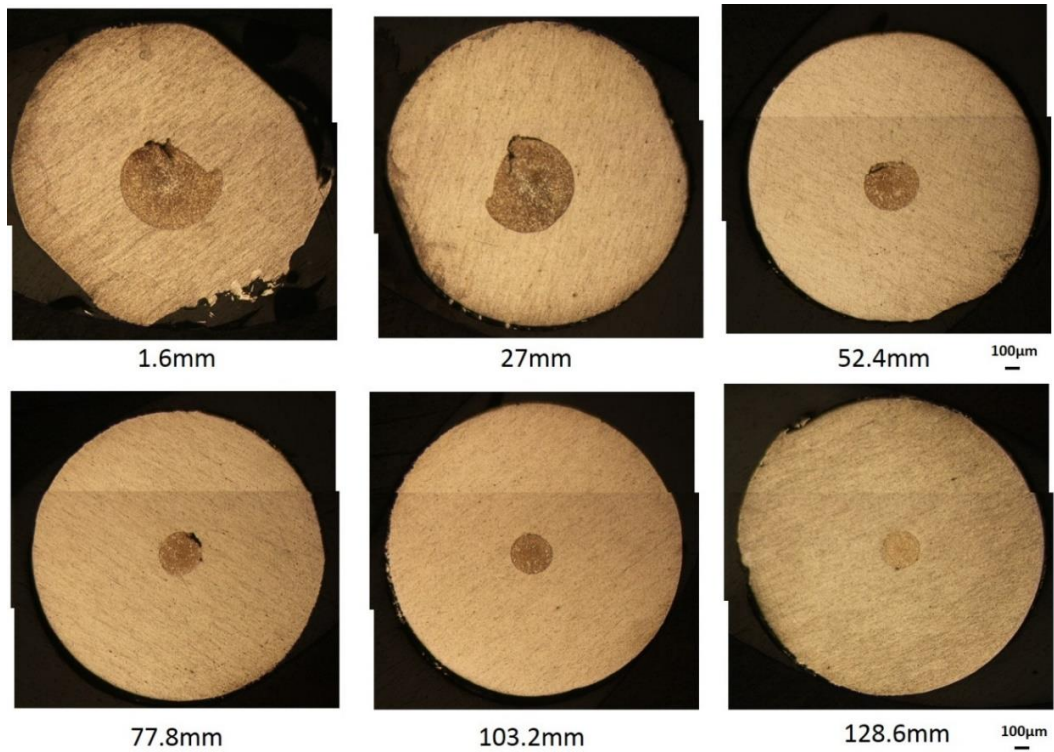
Figure 3.22 Cross-sections of *Φ*2mm wires (flat die, center marker) with distance from beginning of extrusion
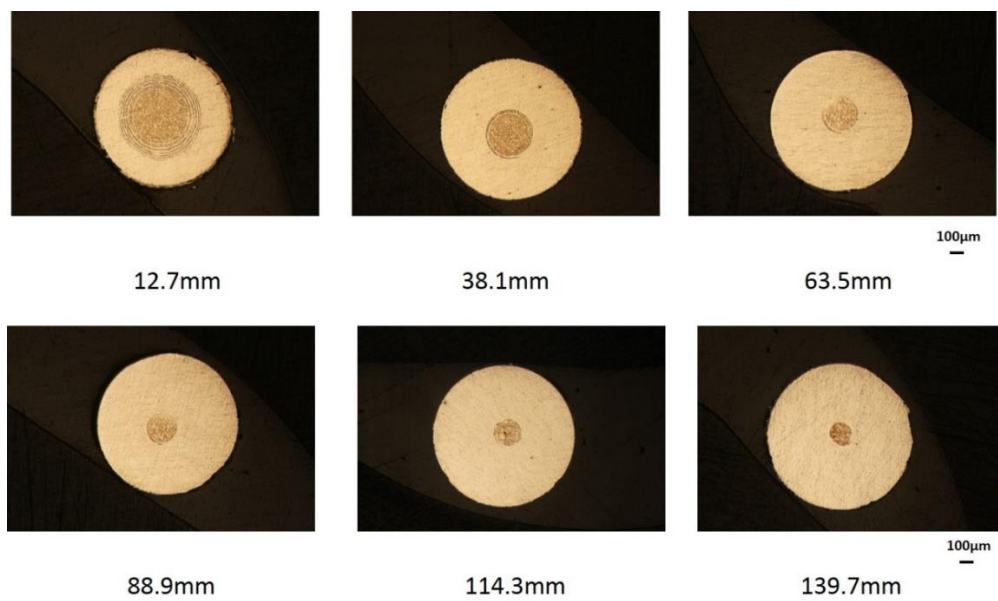
Figure 3.23 Cross-sections of *Φ*1mm wires (flat die, center marker) with distance from beginning of extrusion

0 mm   25.4mm   100μm
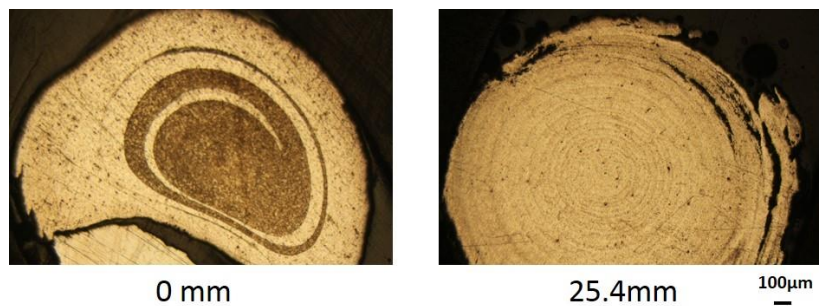
Figure 3.24 Cross-sections of Φ2mm wires (scroll die, center marker) with distance from beginning of extrusion

12.7mm   38.1mm   63.5mm   200μm

Figure 3.25 Cross-sections of 1mm wires (scroll die, center marker) with distance from beginning of extrusion

No marker was seen

12.7mm   38.1mm   63.5mm   100μm

88.9mm   114.3mm   139.7mm
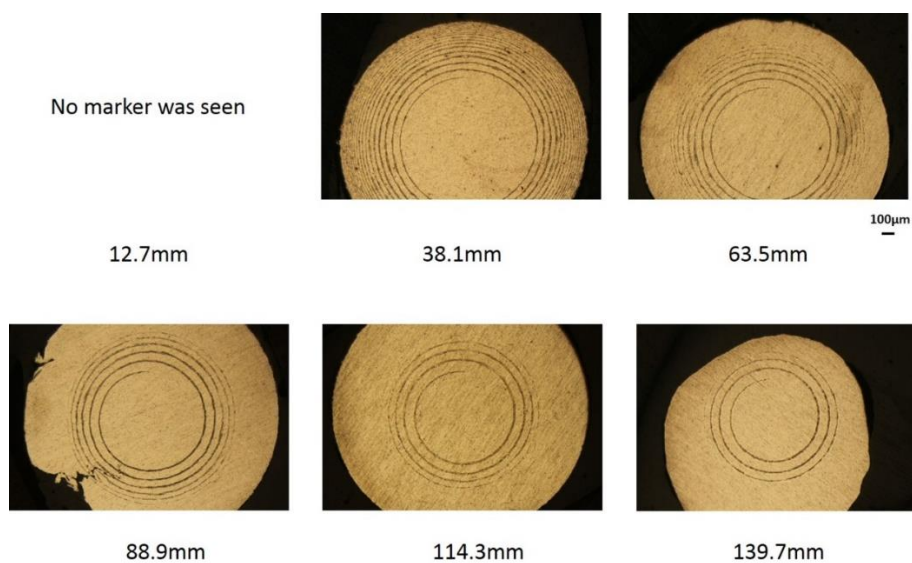
Figure 3.26 Cross-sections of 2mm wires (flat die, 1/3r marker) with distance from beginning of extrusion
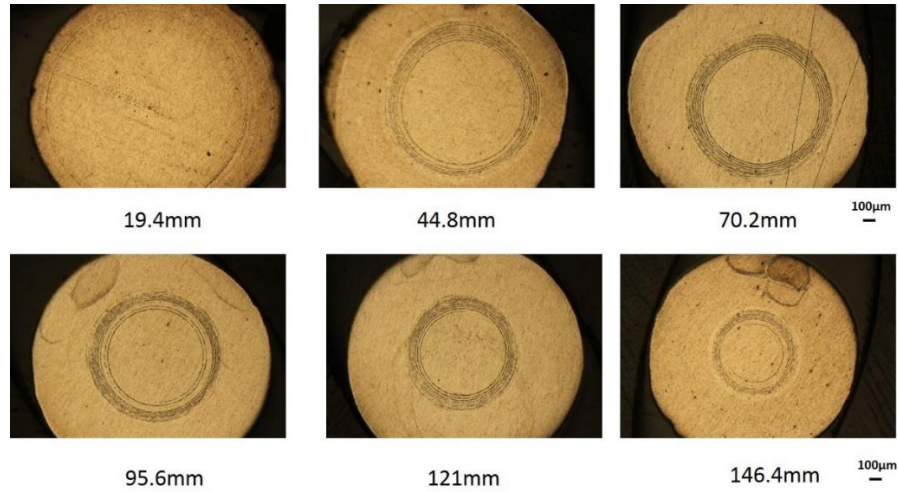
Figure 3.27 Cross-sections of 2mm wires (scroll die, 1/3r marker) with distance from beginning of extrusion

The diameters of markers in wire change along with the length of 0r marked wires are shown in Figure 3.28. It indicates that the diameter of circle marker decreased along wire length increased with a decreasing slope. The same trend was observed in 1/3r marker wire, see Figure 3.26 and Figure 3.27, the diameter of the spiral in wire decreased with length of wire increased.
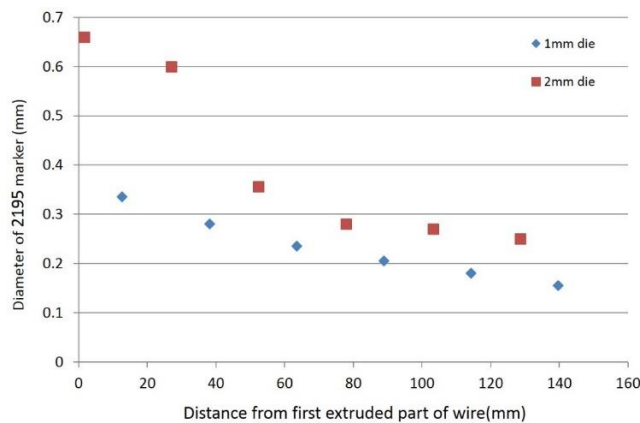
Figure 3.28 Diameter of marker in wire decrease along with length of 0r maker wires increases

For long extruded wire made with a milling machine, at all cross sections, the 1/3r AA2195 marker forms spiral patterns on the wire cross section. However, there are differences in the distribution of marker material and the grain size as functions of extruded length. Figure 3.29 shows cross sections from the extruded wire No.1 taken at 300 mm intervals along its length, 2300 mm. The number of revolutions of marker material spirals on a cross section decreases from the beginning to the end of the wire. Clearly, steady state conditions have not been achieved as the length of the spiral line decreases monotonically with increasing extrusion length. This trend was found in all four wires. The number of spiral rotations on each cross section of the four wires, expressed in radians, was approximated from the images and the data is plotted vs. extruded length in Figure 3.30. In wire No.2 (300RPM, 80.1kN extrusion force), there is no AA2195 detected in the cross-sections that are 80mm and 380mm from the start of wire. Also, in wire No.4 (400RPM, 80.1kN extrusion force), there is no AA2195 detected in the cross-section that is 80mm from the start of wire. Therefore, in the beginning of the process, the material at 1/3 radius doesn't reach the central extrusion hole and enter the wire.
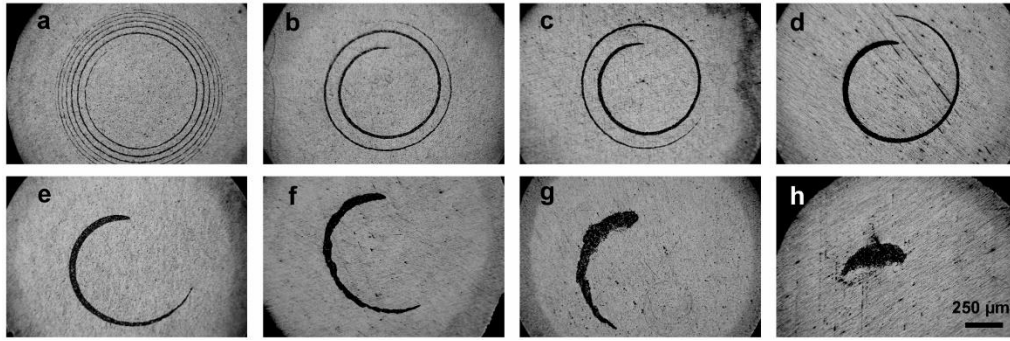
Figure 3.29 Cross sections of extruded wire with 1/3r marker showing variation in marker deformation as functions of distance from the beginning of the extrusion: (a) 80 mm, (b) 380 mm, (c) 680 mm, (d) 980 mm, (e) 1280 mm, (f) 1580 mm, (g) 1880 mm, (h) 2180 mm.
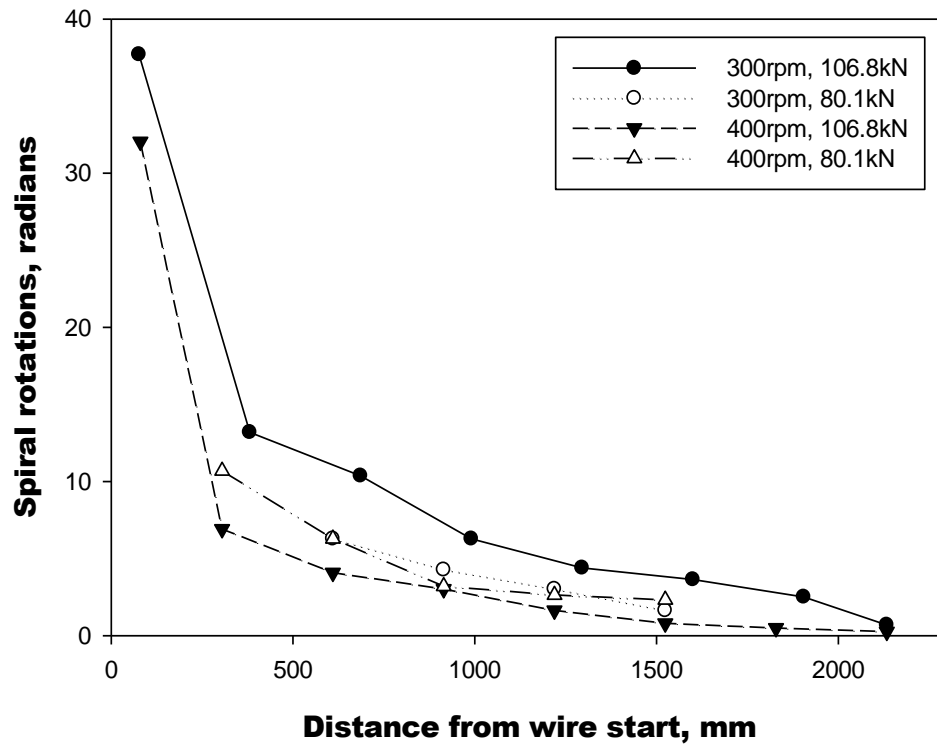
Figure 3.30 Spiral rotations in radians (flat die, 1/3r marker) as a function of distance from extrusion start.

In sum, AA 2195 wire was adopted as marker material inserted in AA 6061 cylinder at different locations and friction extrusion was carried out on those cylinders to investigate material flow/deformation. Except cases of wires were placed too far from center (2/3 radius locations), which resulted in no traceable AA 2195 with the optical microscope, clear AA 2195 patterns were found in extruded wires cross sections. When marker material AA 2195 was inserted at the center of AA 6061 cylinder, it remained the same location in extruded wire and the dimension of 2195 was about 1/10 of its initial size, no matter scroll die or flat die was used. Results demonstrate that near the center of die rotation, the extrusion process is somewhat similar to a "normal" extrusion process. When marker material AA 2195 was inserted at the 1/3 r location, different characters (spiral revolution number and minimum radius) were observed from cross-sections of wires extruded by scroll die and flat die. The deformation/strain values of material extruded by scroll die seem larger than flat die. Die geometry has an effect on the flow but, does not, over the range of geometry examined, fundamentally modify the process.

3.2.3 Parameter study

In parameter study, good quality wires were obtained from all of the extrusion parameter sets except 400 rpm and 22,250N Z-force. Transverse cross sections (12.7mm to the beginning of wire) of all 1/3r marker wires extruded by flat die are shown in Figure 3.31. All AA 2195 showed coaxial multi-spirals pattern. The cross sections at the same

position of scroll die wire are shown in Figure 3.32. With different rpm and Z-axis force, the number of spiral revolutions and inner radius (the distance from the center of the cross-section to the inside end of the spiral line) are different. Inspection of several transverse cross sections of a single wire indicates that these two values are also varying along the longitudinal direction of the wire. See Figure 3.33.

The trend of number of spiral revolutions and inner radius along the longitudinal direction of flat die wire with different control parameters are shown in Figure 3.34 and Figure 3.35, respectively.

rpm Z-force(N)	200	300	400
22250			
44500			
66750			

100μm

Figure 3.31 Transverse cross sections of 1/3r marker wires extruded by flat die, 12.7cm from the beginning of wire
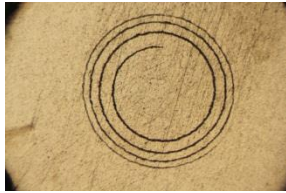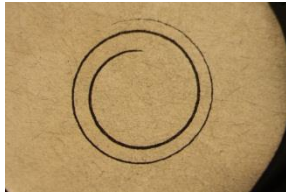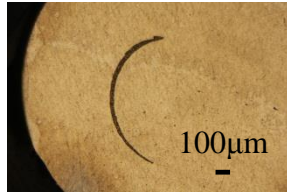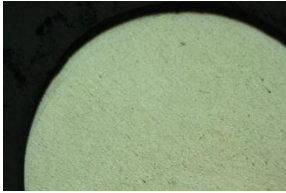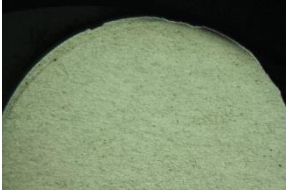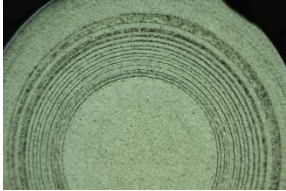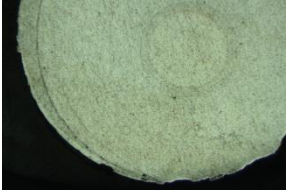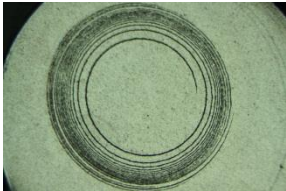
rpm	200	300	400
Z-force(N)			
22250			
44500			
66750			100μm

Figure 3.32 Transverse cross sections of 1/3r marker wires extruded by scroll die, 12.7cm from the beginning of wire

Figure 3.33 Spiral changes along the length of the wire extruded using the flat die with 400 rpm and 44500N, (left) 2.54cm from the beginning (middle) 7.62cm from the beginning (right) 12.7cm from the beginning
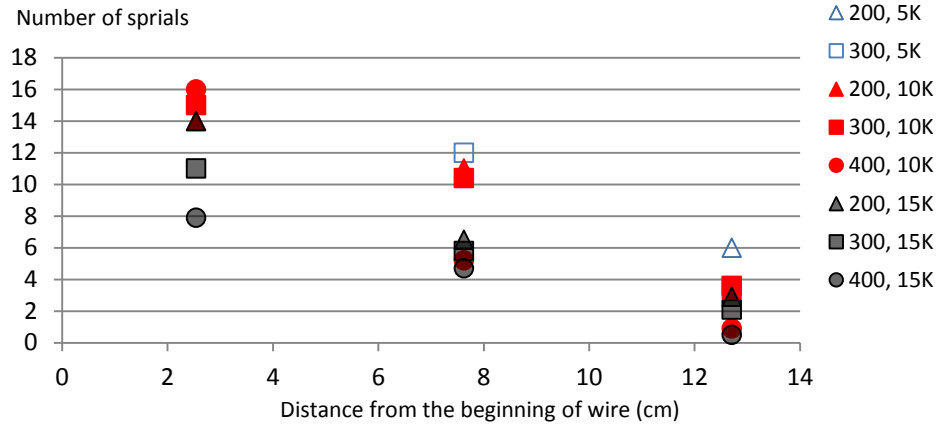
Figure 3.34 Variation trend of number of spiral revolutions along longitudinal direction of flat die wire with different control parameters
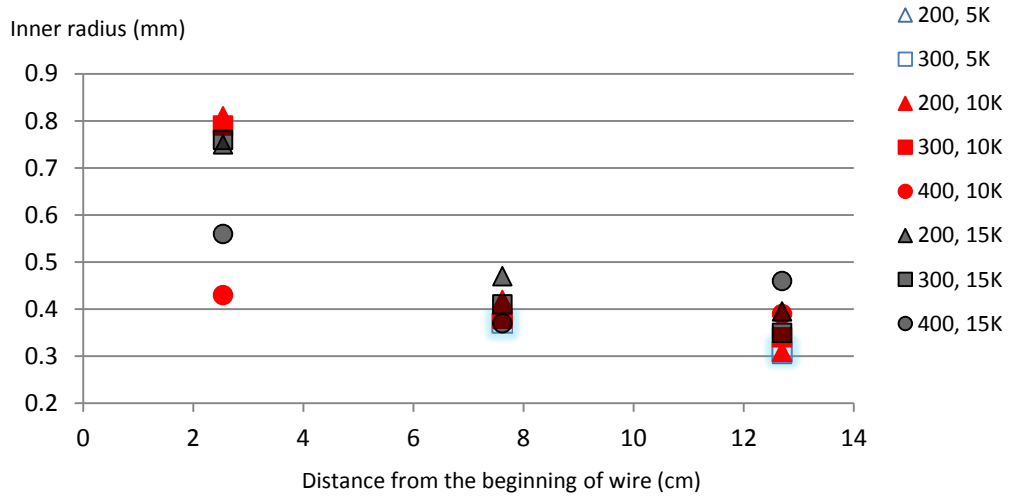
Figure 3.35 Variation trend of inner radius along longitudinal direction of flat die wire with different control parameters

The average extrusion rate in FSWPDS friction extrusion was calculated as following:

Assume the volume of die advanced equals the volume of extruded wire:

$$(h_1 - h_0) \times \pi R_c = \pi R_w L \qquad \text{Eq (3.1)}$$

Where, R_c is the radius of the chamber, R_w is the radius of wire, L is the length of extruded wire, h_1 and h_0 are the final and initial Z position of the die, respectively. h_0 can be determined as the lowest position of the die. So h_1 can be calculated by Eq (3.1). Find the corresponding time of h_1 and h_0, extrusion time is t derived. Let L divided by t, we have average extrusion rate.

The relationship between extrusion rate and die rotational speed, extrusion force are presented in Figure 3.36. Generally, both increased die rotational speed and extrusion force will increase extrusion rate.
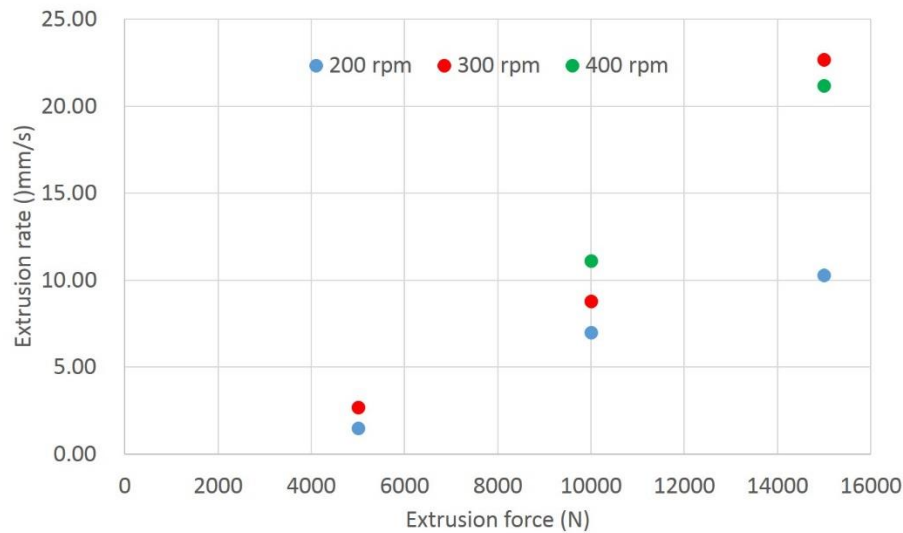
Figure 3.36 Die rotational speed, extrusion force vs extrusion rate

The average power during extrusion time is also related to extrusion rate, see Figure 3.37. It indicates that higher power input will accelerate friction extrusion rate.
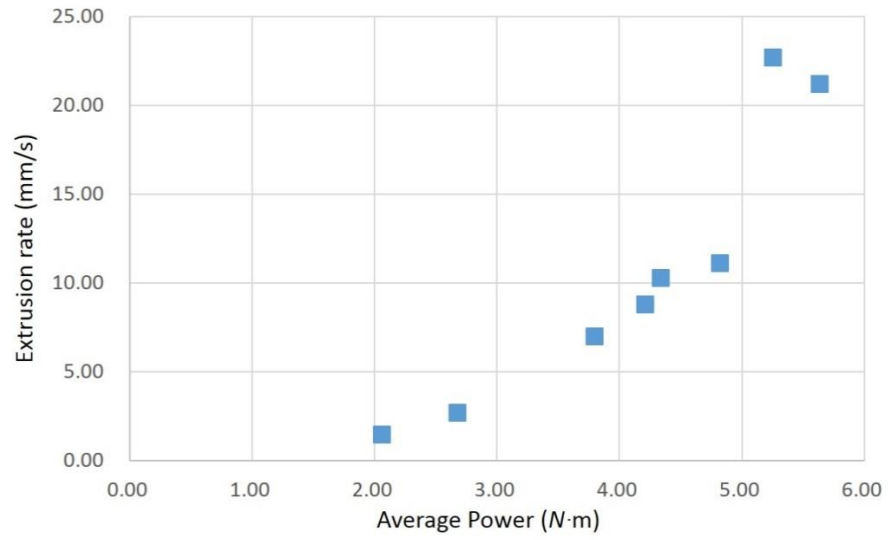
Figure 3.37 Average extrusion power vs extrusion rate

3.2.4 Microstructure, grain orientation and texture analysis
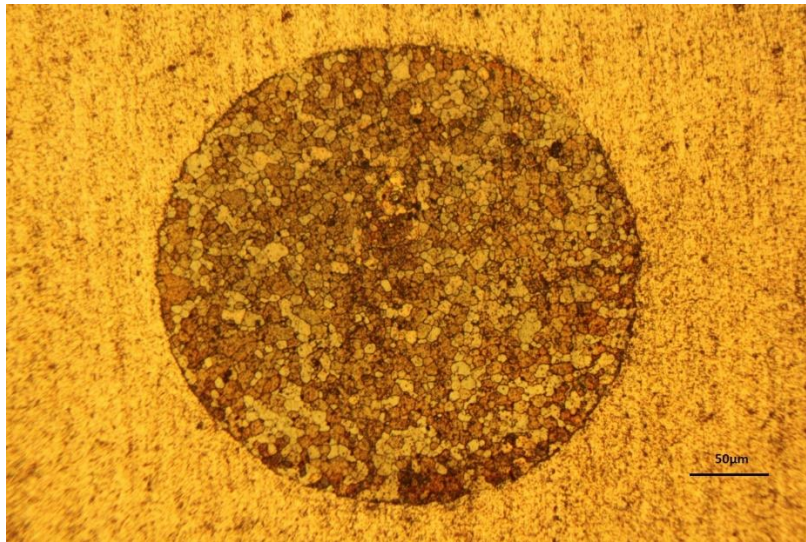
Figure 3.38 Fine equiaxed and recrystallized grain structure of AA2195 in center marked friction extrusion wire, etched with Keller's solution for 8 seconds

Figure 3.39 Fine equiaxed and recrystallized grain structure of AA6061 in friction extrusion wire, etched with Keller's solution for 180 seconds

All cross sections of the extruded wire exhibit microstructures consisting of reasonably fine, equiaxed, and recrystallized-appearing grains with the exception of isolated regions of AGG, see Figure 3.38 and Figure 3.39 as examples. Significantly, based on examination of longitudinal cross sections there is no elongation of the grains in the extrusion direction, as shown in Figure 3.40. This is consistent with previous results [26] on friction extrusion of aluminum alloy wires. In Figure 3.40, some cracks at the boundary between the AA2195 marker and the AA6061 are observed. This kind of crack was observed only in the latter part of wire where the in-plane strain was relatively small. This phenomenon implies that in the latter part of the extrusion, the reduction in the in-plane strain may result in insufficient deformation to "weld" the marker to the billet. Figure 3.41 shows the grain size measured in the AA2195 marker material for both transverse and longitudinal cross sections as well as the AA6061 grain size determined by MLI from the

EBSD grain maps for wire number 1. Grain size in the markers is nearly the same for both longitudinal and transverse sections. The grain size of the AA2195 markers is substantially less than in the AA6061: this is not surprising given the higher solute and dispersoid levels in AA2195 vs. AA6061. All of the data show a trend toward increasing grain size with increasing extrusion length, corroborating the non-steady state behavior of the markers. Sato et al. [31] determined that nugget grain size in friction stir welding (FSW) is related to the FSW temperature. It is expected that the temperature of the billet will increase as the extrusion process progresses due to the buildup of process heat, which matches with previous results of experiment and simulation by [76]. Figure 3.41 shows that wire grain size continues to increase as the wire gets longer, which indicates that the extrusion temperature increases continuously during the process.
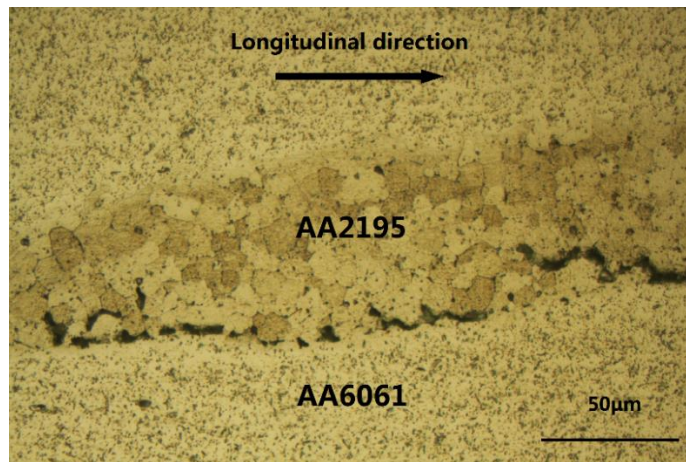
Figure 3.40. Equiaxed AA2195 grains in the longitudinal cross section of friction extruded wire, 1.6m from the start of wire No.1 made by the modified milling machine.
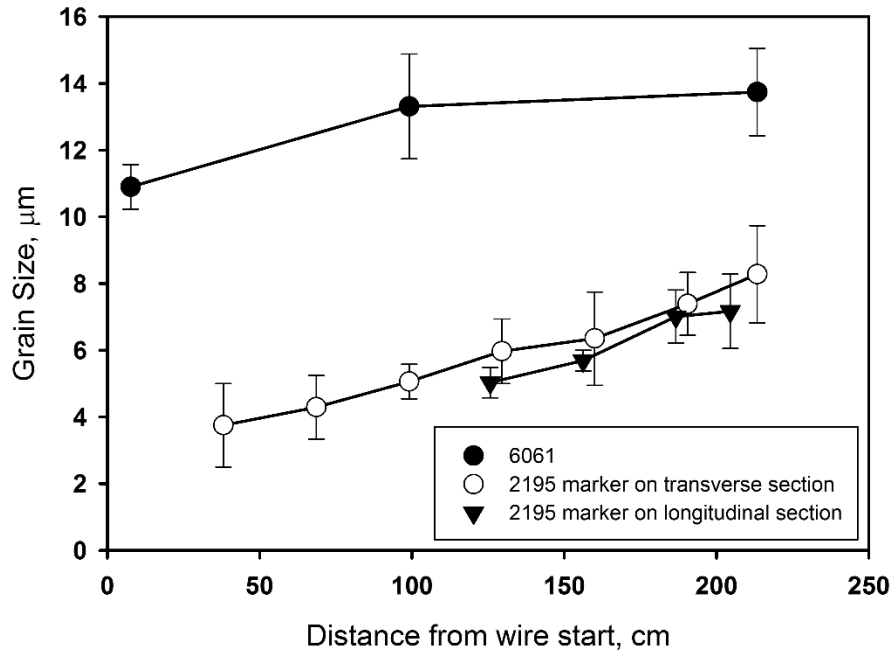
Figure 3.41. Grain size in 2195 marker and 6061 as functions of distance from extrusion start, wire No.1 made by the modified milling machine.

Inverse pole figure maps and pole figure maps are presented in Figure 3.42 and Figure 3.43 for the three specimens taken at the end, middle, and beginning of the extruded wire. In each pole map, the extrusion direction is normal to the plane of the map and each map contains information from a 300 μm wide strip along a wire diameter (2.4 mm). Thin black lines denote high angle grain boundaries ($\theta > 15°$). AGG is far more prevalent in the last material extruded as evidenced by the numerous large grains seen in Figure 3.42(1). Average textures are similar for each scan but are rather weak with the maximum intensity of from 2.6 to 3.1 times random. However, it can be seen in Figure 3.42 that each scan exhibits a region near the wire center where a stronger <100> texture is observed (the red grains). Qualitatively, the region of strong <100> texture increases with increasing wire

length; therefore corresponding to (1) larger grain size and (2) fewer marker spirals and lower transverse strain. Away from the center of the wire, the strength of the texture diminishes.
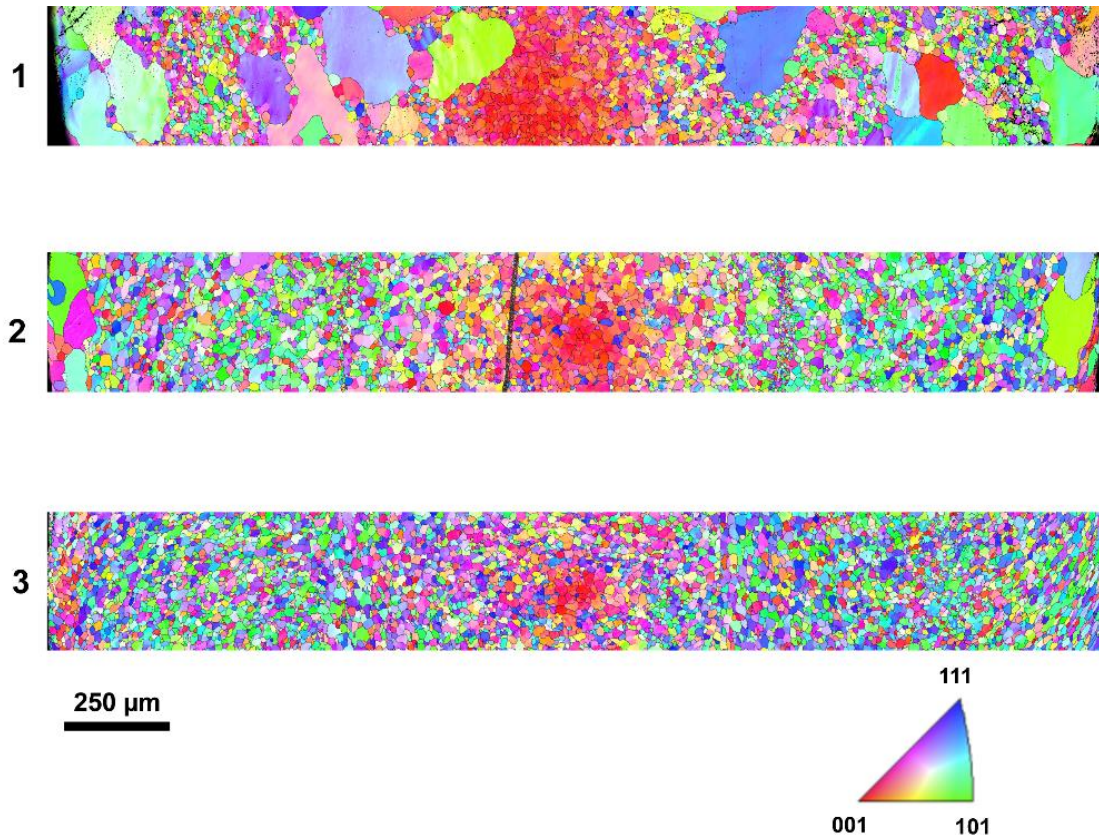
Figure 3.42. Inverse pole figure maps from the cross sections of wire No.1: (1) 2180 mm from extrusion start, (2) 980 mm from extrusion start, and (3) 80 mm from extrusion start.
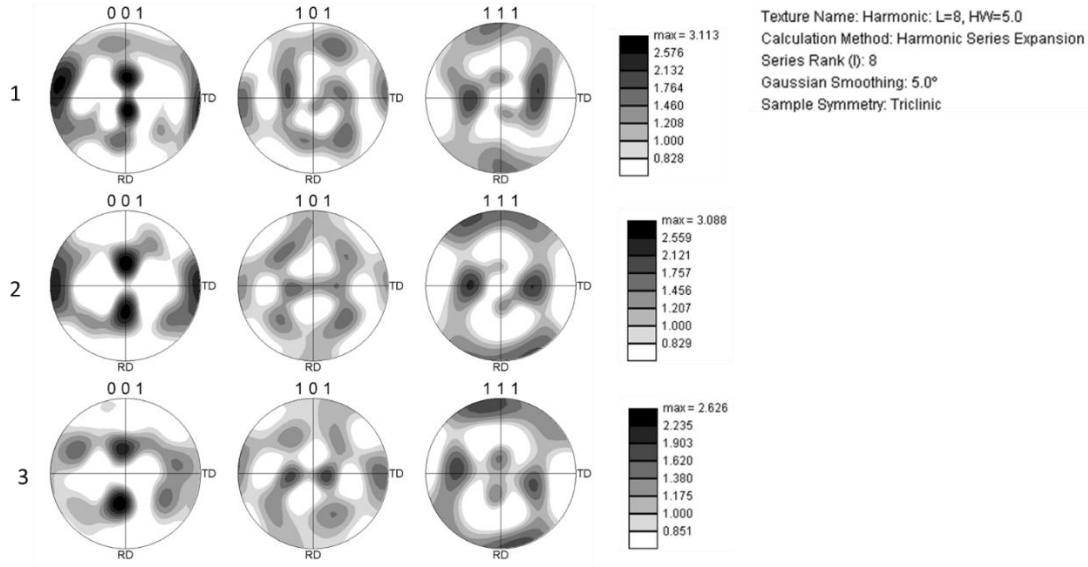
Figure 3.43. Pole figure cross sections of wire No.1: (1) 2180 mm from extrusion start, (2) 980 mm from extrusion start, and (3) 80 mm from extrusion start

3.2.5 Strain analysis in wires made by modified mill machine

In order to develop a measure of the strain experienced by the marker material, the deformation was deconvoluted into two parts: a longitudinal strain (in the extrusion direction) and a transverse strain in the plane of the cross-section. In conventional extrusion, the ideal strain is calculated based on the extrusion ratio, which is the ratio of the cross-section area of billet and the area of extruded part. Similarly, the longitudinal strain was estimated by measuring the area of the marker on the metallographic section and calculating the strain as:

$$\varepsilon = \ln(A_0/A_f) \hspace{4cm} \text{Eq (3.2)}$$

In eq (3.2), A_0 is the original cross-sectional area of the marker wire and A_f is the total observed area of marker material in the extrusion cross section. The transverse or in-

71

plane strain is obtained by use of several assumptions and is not intended to be an exact calculation but to give a rough, order-of-magnitude estimate. The calculated transverse strain is strictly applicable only to the radial position at which the marker was placed (1/3 r). In addition, it cannot be determined with certainty that all the material in a wire cross-section came from the same plane in the billet. Regardless, the observed trends in the measurements are consistent and useful for interpretation of the process progression. The procedure used for the rough estimation of the in-plane strain is as follows:

1) The marker area on the cross section (A_f from equation 3.2) is converted to a circle with the equivalent area and corresponding diameter, d_0.

2) The transverse or in-plane strain is calculated as:

$$\varepsilon = \ln(d_f/d_0) \qquad\qquad \text{Eq (3.3)}$$

Where d_f is the actual length of the "spiral" on a given cross section.

The in-plane or transverse strain and longitudinal strains of wire No.1 are plotted as functions of distance from the start of the wire in Figure 3.44. From the figure, it can be seen that the longitudinal strain is nearly constant and is similar to what would be expected based on the overall reduction, 4.0 while the in-plane strain declines with increasing wire length and practically vanishes at some distance from the wire start.
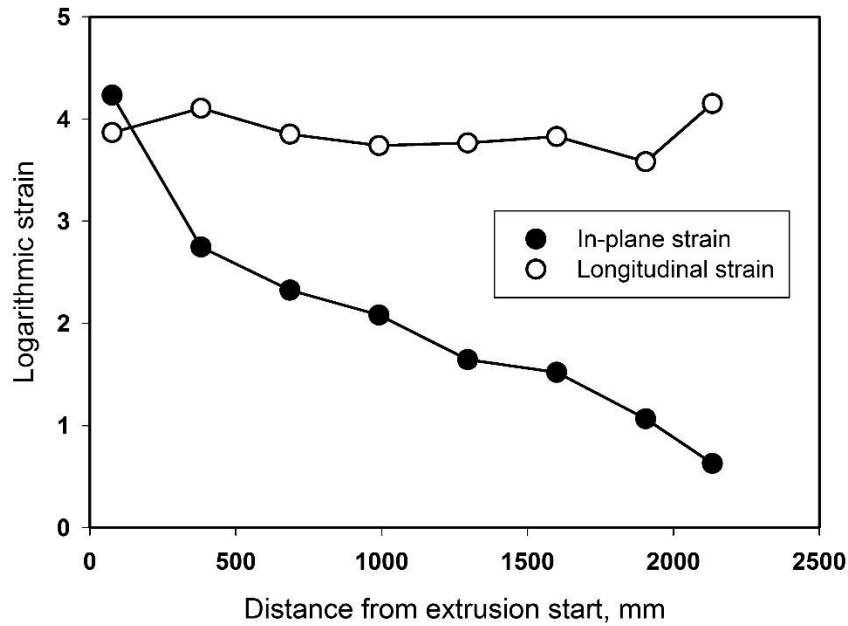
Figure 3.44. In-plane and longitudinal strain from the R/3 position as functions of distance from the extrusion start, wire No.1.

The in-plane strain and longitudinal strain of the other 3 wires were also calculated. Along with wire No.1, these results are presented in Figure 3.45 and Figure 3.46. The trends of strain in all wires are consistent: in-plane strain decreases and longitudinal strain remains nearly constant with increasing wire length. At the same position in the wire relative to the start of the extrusion, the in-plane strain of wire made with higher rotational speed is relatively smaller than the in-plane strain of wire made with lower rotational speed. Compared with lower extrusion force conditions, the higher extrusion force conditions have a lower in-plane strain in the last part of the wire. The longitudinal strain does not change much along the length of any wire nor with changes in adopted extrusion

parameters and is, as mentioned in the preceding, dependent on and consistent with the

overall extrusion reduction.
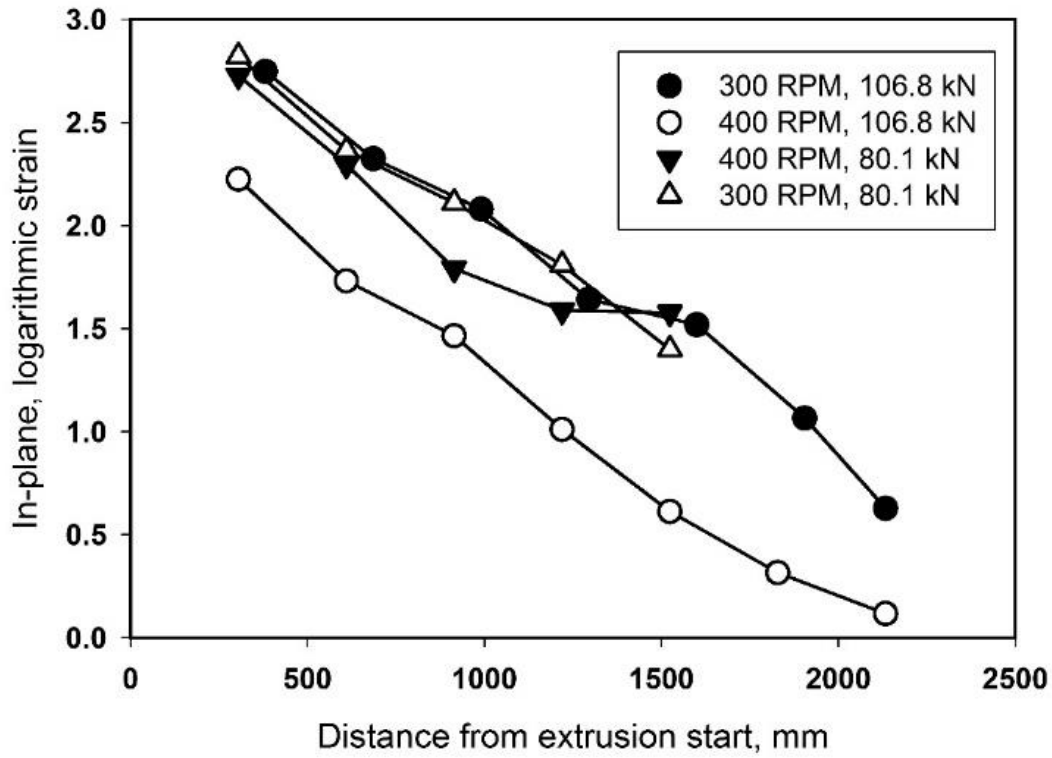
Figure 3.45. In-plane strain from the R/3 position as functions of distance from the extrusion start, with various extrusion forces and rotational speed.
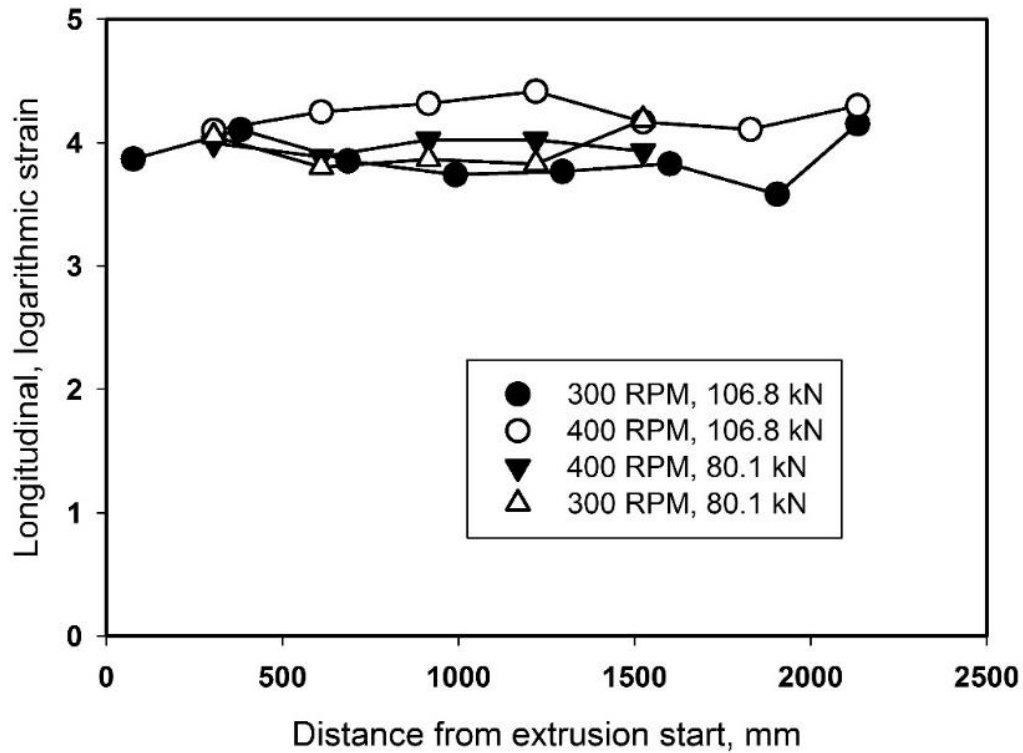
Figure 3.46. Longitudinal strain from the R/3 position as functions of distance from the extrusion start, with various extrusion forces and rotational speed.

3.2.6 Comparison with finite element model

To better study the mechanism of friction extrusion process and contribute to the creation of a scientific knowledge base for this novel process, finite element method was introduced to analysis heat transfer, material flow and predict process progression in different experimental parameters. A numerical non-flow based thermal model was first built to simulate temperature field distribution of friction extrusion process made by FSWPDS. Results of experimental temperature measurement were used to validate it. Then, a thermal-fluid model with marker particles was developed to provide reasonable

75

predictions of the temperature and material flow fields in the friction extrusion process. A mathematical code was programmed in Matlab to help reconstruct the marker pattern so that it can be compared with experimental observation.

3.2.5.1 Temperature field in heat transfer model

To understand heat transfer phenomenon and the temperature field in the friction extrusion process, a numerical thermal model for the experimental system has been developed by co-worker[73]. The model includes the rotating extrusion die, the material being processed inside the extrusion chamber, and the chamber wall and the back plate at the bottom of the chamber wall. The experimentally measured mechanical power is used as input to the model to predict the temperature field in the experiment. Temperatures were measured and recorded in several locations during the experiment to compare with the simulated result and validate finite element model.

Similar to non-flow based thermal models for friction stir welding, this is a pure thermal model in which the material flow is not modeled. As such, and considering the characteristics of the problem, such as the geometry, the governing equation, and the boundary conditions, a two-dimensional axisymmetric model is found appropriate for the process. Utilization of axisymmetry saves computing cost significantly since only half of the cross-sectional area along the axis of symmetry is needed for the geometry. The finite volume method was used to discretize the computational domain. The computational grid is shown in Figure 3.47. A grid with a cell size of 0.5 mm was used. The time step is 0.05

76

second. Convergence analysis with smaller grid sizes and time steps has been conducted

and the grid used in this work is converged. The commercial code ANSYS FLUENT was

used to carry out the computations.
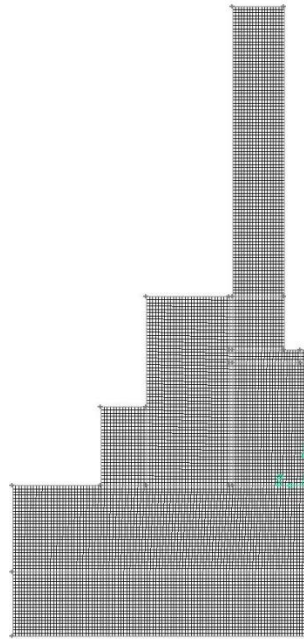
Figure 3.47 Thermal model grid of finite element model of friction extrusion

In this method, a volume heat source method is employed. Heat generation is

represented by a volume heat source in a material layer in the sample that starts at the

interface and ends somewhere below the interface. In this layer, the sample material is

expected to undergo extensive material flow and severe plastic deformation. The use of a

volume heat source model is intended to include the effect of heating contributions from

two sources: the heat source in the volume region immediately adjacent to the interface can

approximate the frictional heating at the interface and the heat source in the volume region

further away from the interface can approximate the plastic energy dissipation away from the interface.

The height of the layer is determined based on experimental observations of the material flow region in the sample. At the end of the friction extrusion experiment, observations of marker material positions in the remnant of the sample in the chamber revealed that the depth of the material flow region in the remnant is about 4.5 mm (Figure 3.19) at one-third of the sample radius from the center and it is smaller near the edge of the sample. As an approximation, and for simplicity, a material layer from the interface to a uniform depth of 4 mm below the interface is taken as the layer with a volume heat source.
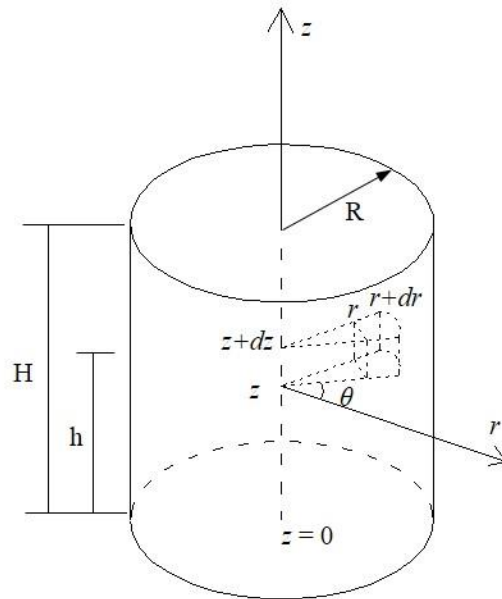
Figure 3.48 Sample geometry and coordinates of friction extrusion

First, it is noted that the radial distribution of frictional surface heat flux is often approximated by a linear distribution in the friction stir welding literature, resulting from

78

the product between a shear stress created by a uniform tool pressure and a tangential velocity created by rigid tool rotation. For simplicity, and as a first-order approximation, this linear distribution in the radial direction is adopted in the present study in the volume heat source method, since the volume heat source is in a region immediately adjacent to the die-sample interface. Second, in the vertical direction (which is the axial direction of the cylindrical sample), it is expected that plastic deformation is greater closer to the die-sample interface, thus, more heat is expected to be generated closer to the interface. Again, for simplicity and as a first-order approximation, a linear distribution along the vertical direction is assumed for the volume heat source.

Based on the above simplifications, the heat generation rate in the volume heat source method can be expressed as below

$$q = m(z - h)r \qquad \text{Eq (3.4)}$$

Where m is a power-related quantity to be determined from the mechanical power input, q is the volumetric heat generation rate, and h is the height of the sample without a heat source (see Figure 3.48 for a schematic of the sample geometry and the coordinate system).

The total heat generation can be obtained by integration over the volume heating layer from $z = $ h to $z = $ H (see Figure 3.48):

$$Q_{total} = \int_0^{2\pi} \int_0^R \int_h^H q \cdot r \, dz \, dr \, d\theta = \frac{1}{3} m\pi (H - h)^2 R^3 \qquad \text{Eq (3.5)}$$

In the current thermal model, Q_{total} is set to equal to the mechanical power input in the friction extrusion experiment, which was recorded in the experiment as a function of time. From equation (3.5), the quantity m can be determined, which can be substituted into equation (3.4). Finally, the volumetric heat generation rate per unit volume is given by

$$q = \frac{3Q_{total}}{\pi(H-h)^2 R^3}(z-h)r \qquad \text{Eq (3.6)}$$

This expression is implemented into the code FLUENT through a user defined function.

Since the material flow is not considered, the only needed governing equation to be solved is the transient heat conduction equation. The expression of the two-dimensional axisymmetric conduction equation is given by

$$\frac{1}{r}\frac{\partial}{\partial r}\left(kr\frac{\partial T}{\partial r}\right) + \frac{\partial}{\partial z}\left(k\frac{\partial T}{\partial z}\right) + q = \rho c_p \frac{\partial T}{\partial t} \qquad \text{Eq (3.7)}$$

where T is the temperature, t is the time, k is the thermal conductivity, ρ is the density, c_p is the specific heat, and q is the heat generation rate per unit volume which is given by equation (3.6).

In the extrusion experiment, temperature variations were recorded at designated locations using thermal couples. The measured temperature variations with time are plotted in Figure 12. For validation purposes, temperature variations at the same locations that are predicted by the thermal model are also shown in Figure 12. At $t = 0$, the die began to rotate and there already was a vertical force of 2.2 kN exerted on the sample. The extrusion of the wire started at about $t = 10$ seconds and ended at $t = 27.7$ seconds.
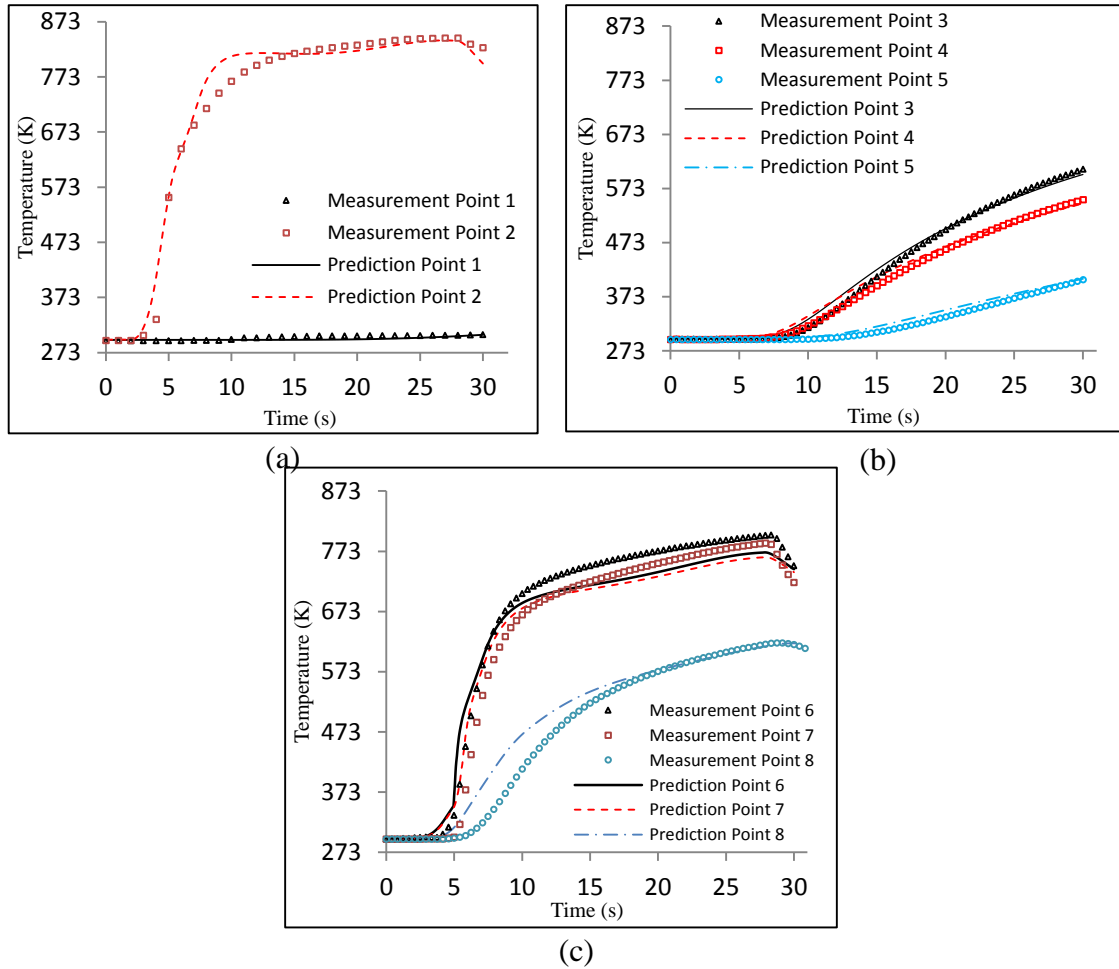
Figure 3.49 Comparisons between predictions and experimental measurements for (a) points 1 and 2, (b) points 3, 4, and 5, (c) points 6, 7, and 8.

Generally, the comparisons show a good agreement between predicted and measured temperature variations with time. Point 2 was in the extrusion die near the die/sample interface. It can be seen from Figure 3.49(a) that the predicted temperature variation at point 2 matches the experimental measurement very well, which indicates that the heat transfer between the die and the sample has been modeled accurately. For the predictions at points 3, 4, and 5, illustrated in Figure 3.49(b), there are small discrepancies with experimental measurements. That might be caused by the uncertain effects of the

initial gap between the sample and the chamber wall. The temperature variation at point 8, shown in Figure 3.49(c), has a more noticeable mismatch between the predictions and the experimental measurements in the period when the temperature began to rise. The predicted temperature is higher than the measured value during that period. A possible reason for the mismatch is that the contact between the sample and the back plate was imperfect in the experiment while it is assumed to be perfect in the thermal model. Overall, since there are eight thermal couples which were located in different parts in the experimental setup and a very good agreement between model predictions and experimental measurements is found, it is believed that the heat transfer phenomenon during the friction extrusion process has been reasonably captured in the thermal model.

3.2.5.2 Temperature field and material flow study in 3D fluid dynamics model

To study the friction extrusion process with the combination of both heat transfer and material flow field, a three-dimensional thermo-fluid Computational Fluid Dynamics (CFD) model has been developed. The heat generation source from a pure thermal model was adopted. Some massless particles were used in the fluid in the modeling to capture the material flow pattern. To compare with experimental observation of AA2195 marker on the transverse direction of friction extrusion wire, the pattern of these maker particles was re-constructed based on their exit positions and exit times derived from simulation. The path lines of the particles show the material flow in friction extrusion process.
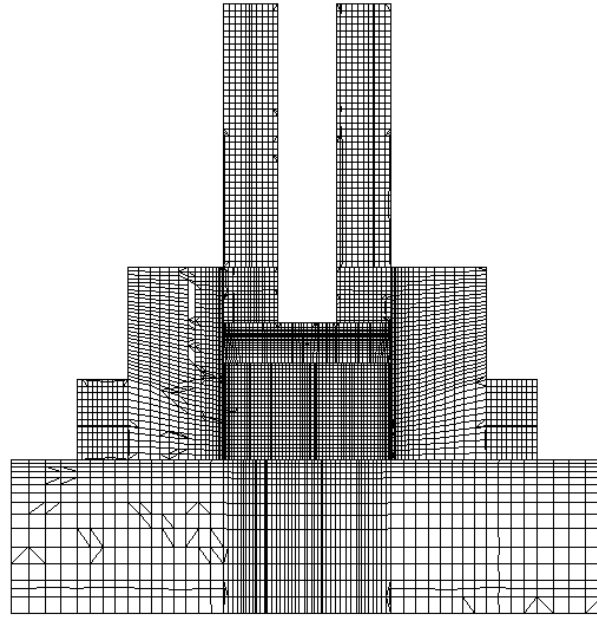
Figure 3.50 A cross-section of the converged grid of 3D fluid dynamics model

The model includes all parts in the experiment, such as the die, the chamber wall, the back plate, and the table. Only limited parts of the die, back plate, and table are modeled in the simulation and their sizes used in the model are chosen so that they represent them well. The other parts have actual geometrical dimensions of the experimental setup. The finite volume method is used to discretize the computational domain. In the modeling, the precursor material is treated as a non-Newtonian fluid and the other parts are considered as rigid solids. A cross section of a converged mesh is shown in Figure 3.50. The minimum size of the mesh is located at boundary layers which are close to the interfaces between solids and fluid and its size is 0.05 mm and the maximum cell size is 1.2 mm. In the current work, the heat transfer and material flow are modeled not in a fully coupled way. Instead of frictional heating and fluid viscous dissipation (or plastic deformation), the same thermal

model in pure heat transfer model is used. The commercial code ANSYS FLUENT is used for the computation.

The total power input in the model is correlated to the mechanical power recorded in the experiment based on the fact that almost all mechanical power was converted into heat. The heat generation rate per volume in the layer is assumed to be linear both along vertical and radial directions, as described below

$$q = \frac{3Q_{total}}{\pi(H-h)^2 R^3}(z-h)\sqrt{x^2+y^2} \qquad \text{Eq (3.8)}$$

Where q is the heat generation rate per volume, Q_{total} is the power input equal to the mechanical power in the experiment which is shown in Fig. 8, H is the height of the precursor sample, h is the height of the sample minus the volume heating layer, and R is the radius of the sample. The heat source is implemented in ANSYS FLUENT through a user defined function.

The thermo-fluid model involves both heat transfer and material flow so the governing equations needed to be solved include continuity equation, Navier-Stokes equations, and energy equation. By using indicial notation for i=1, 2, and 3 representing x, y, and z coordinates, the continuity equation for an incompressible flow is expressed as:

$$\frac{\partial u_i}{\partial x_i} = 0 \qquad \text{Eq (3.9)}$$

Where u is velocity. The Navier-Stokes equations for non-Newtonian transient fluid flow are given by

$$\rho \frac{\partial u_j}{\partial t} + \rho u_i \frac{\partial u_j}{\partial x_i} = -\frac{\partial P}{\partial x_j} + \frac{\partial}{\partial x_i}\left(\mu \frac{\partial u_j}{\partial x_i}\right) + F_j \qquad \text{Eq (3.10)}$$

Where ρ is density, μ is fluid viscosity, and F is body force. The equation of energy conservation is

$$\rho c_p \frac{\partial T}{\partial t} + \rho c_p u_i \frac{\partial T}{\partial x_i} = \frac{\partial}{\partial x_i}\left(K \frac{\partial T}{\partial x_i}\right) + q \qquad \text{Eq (3.11)}$$

Where c_p is specific heat, T is temperature, K is conductivity, and q is the heat generation rate given by equation (3.8).

The first thing to validate this model is to compare simulated temperature with measured value in the experiment. As described in Section 3.1.1.4, the temperature at several different positions in the friction extrusion experiment was recorded. The measured temperature variations with time are compared with numerical predictions as shown in Figure 3.51. In general, a good agreement between the experimental measurements and the predictions is observed.
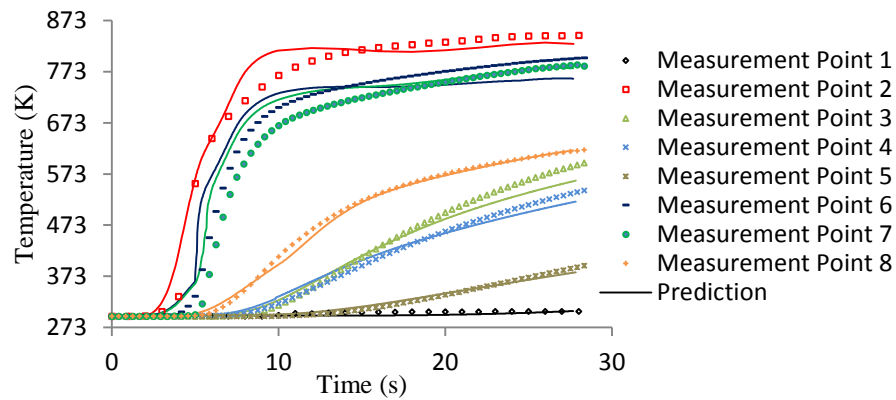
Figure 3.51 Comparisons between temperature predictions of thermal-fluid model and experimental measurements
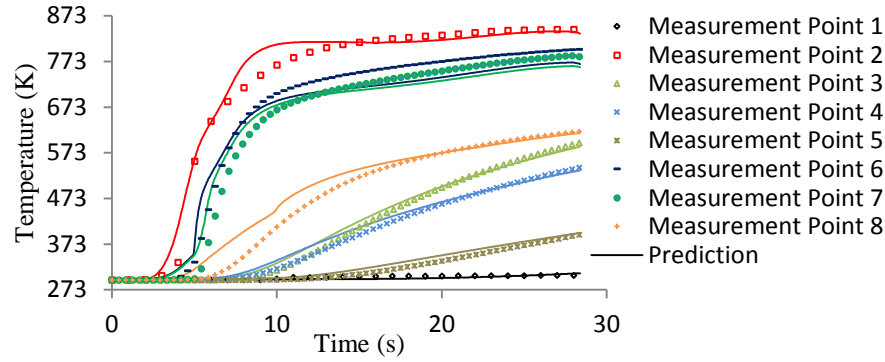
Figure 3.52 Comparisons between temperature predictions of pure thermal model and experimental measurements

For comparisons, the temperature predictions compared with the same experimental measurements in the pure thermal model are shown in a separate Figure 3.52. Since the experimental measurements are the same, changes from the two numerical models can be observed from the comparisons. It is seen that there are unnoticeable differences for the temperature at point 1, 3, 4, and 5, which are on the outer surfaces, far from the heat source zone. The temperatures at rest points have mild changes after t = 10 s. The changes come from mainly from the influence of material flow and movement of the heating zone (moving down pushed by the die). The material flow introduces convection heat transfer in the material and the movement of the heating zone results in variations of the distances from the heat source to the temperature measurement points. The temperature at sensitive points (point 2, 6, 7 and 8) which are closer to the heat source zone have larger changes. For point 8, the temperature prediction in this work has a better agreement with the experimental measurement which is mainly due to the using thermal resistance between the aluminum alloy sample and the back plate. It is shown from the

comparisons above that (1) the temperature field can be reasonably predicted by using the pure thermal model in the current decoupled thermo-fluid model, (2) thus, the method used in friction stir welding, applying thermal models in fluid modeling, also works in modeling of friction extrusion process, and (3) the material flow has very limited influence to the heat transfer phenomenon.

It is found that the predicted temperature variations at the locations of the thermal couple tips agree well with those measured experimentally, suggesting that the thermal model can serve as a reasonable predictive model for the temperature field distribution in the friction extrusion process.

Figure 3.53 presents the contour graphs of the temperature field on the entire cross section of the thermal system (they were created by mirroring the model predictions from one-half of the cross-section to the other half) at several instants in the friction extrusion process. Figure 3.53 (a) shows the temperature field at t = 7 seconds. Apparently, the heat source region had higher temperatures due to the fact that heat generation occurred from there. At this moment, only a part of the initial gap between the sample and the chamber wall was filled with the hot sample material from near the die/sample interface. Consequently, the heat was conducted through the partially filled gap into the nearby chamber wall, and as a result, the temperature was higher in the region of the chamber wall that is close to the partially filled gap. At the same time, the lower part of the gap, which was still unfilled, blocked the heat transfer from the heated sample to the chamber wall, so

the temperature was much lower in that part of the chamber wall. Because of the perfect

contact between the sample and the back plate in the thermal model, heat flowed into the

back plate without obstruction. However, the stainless steel back plate has a much lower

thermal conductivity than the AA6061 billet charge so that heat did not flow deeply and

quickly into the back plate and the temperature rise there is limited to the sample-backplate

interface region.
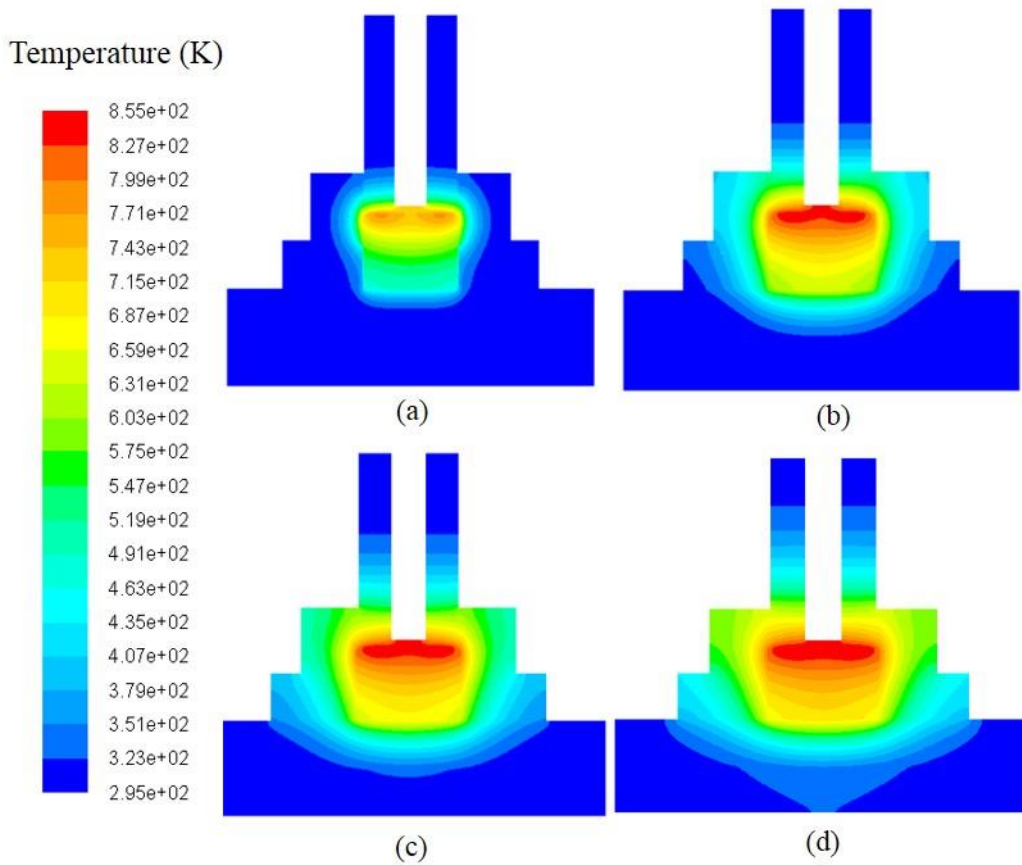
Figure 3.53 Predicted temperature contours of friction extrusion at (a) t = 7s, (b) t = 14s, (c) t = 21s, (d) t = 27.7s.

Figure 3.53(b) gives the temperature contours at t = 14 seconds. At that instant, the gap between the sample and the chamber wall had been filled completely so that heat flow into the chamber wall was not blocked anymore and temperature rise in the chamber wall was now more evident. The temperature near the sample-die interface was pronouncedly high since it is close to the heat generation heat source. The die also has a relatively low thermal conductivity compared with the sample, so that heat transfer into the die did not go very deep and the temperature rise in the die is limited to the sample-die interface region.

Figure 3.53(c) and (d) show how the temperature field was developed at t = 21 second and 27.7 seconds respectively. Obviously, heat flowed from the sample into the chamber wall continuously with ease since the gap between the chamber wall and the sample had been completely filled. Correspondingly, the temperature in the chamber wall rose continuously. The region below the die/sample interface always had the highest temperatures and the material in this region was the source of the subsequently extruded wire. It is also clearly shown that heat flowed into the die slowly.

From the model predictions, it can be seen that the highest temperature is about 848 K, which occurred at the end of the extrusion and at a location within the heat generation zone. This highest temperature was below the aluminum alloy's solidus temperature of 855 K so that melting did not occur. It is consistent with experiment observation that there is no defects or voids in the remnant sample.

89

Another crucial clue to valid the numerical model with experiment observation is material flow or material re-distribution. In the experiment, marker material had been placed into cylinder sample at a certain position. After friction extrusion, this marker material was revealed by etching several transverse cross-sections along extruded wire. In the numerical simulation, some traceable massless particles are pre-placed at the same position in the model. These particles can be tracked and their trajectory paths can be recorded during the simulation. By deriving the path lines of these particles, the material flow can be visualized and compared with the result from the experiment.

The distribution of marker material in experiment cylinder sample is shown in Figure 3.54 left. It is a solid bar located at 1/3 radius far from the central line and ran through z-direction of cylinder sample. In finite element simulation model, traceable massless particles are pre-placed on a z-r plane, see Figure 3.54 right. Since the deformation zone is about 4mm thick from the top of the cylinder, only this region had been placed particles. To note, instead of continue bulk mass in reality, these marker particles are discrete. From z equals to 18mm to 15mm with 0.0125mm interval, r equals to 2.93mm to 5.57mm with 0.22mm interval, totally 325 tiny massless particles had been placed. In the modeling only some particles are extruded out of the chamber and the distribution of them on the extruded wire can be compared with experimental measurements. In the experiment, the traces of the marker material can be observed clearly on the extruded wire cross sections although it was distorted and stretched since the marker

material is a continuum. However, in the simulation, the number of the solid particles is finite and it is not enough to have a better view effect when comparing them with experimental observations on wire cross sections. To have better comparisons, interpolations of the predictions about the particles positions on extruded wire cross sections are done to obtain more data points.
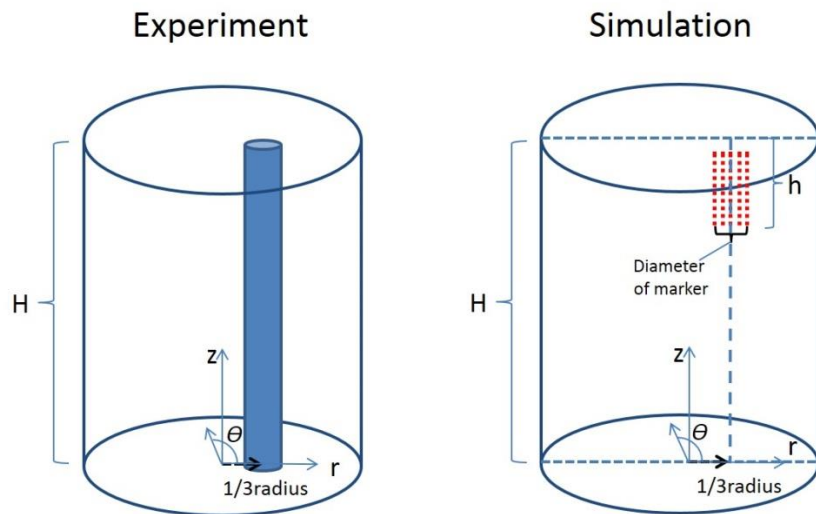
Figure 3.54 Marker distribution in friction extrusion, experiment sample (left) and simulation model (right)

Some assumptions are made before reconstructing the marker pattern:

a) It is assumed that at the moment when material exited extrusion hole, it left heat source, lost mobility and was fixed there. So, the particles' position on the plane of exiting hole, which is the top surface of the cylinder, can be presented together as a figure and compared with transverse cross-section images of wire in experiments.

b) Since the geometry of cylinder sample is central-symmetric, it is assumed that

two particles with same initial height and radius but different angle should have

the same shape of path line but with an angle difference. For gaining

information out of plane where no particle was pre-placed, we can derive result

at positions which have same radii but different angle with known positions.

c) Extrusion rate is constant. Which means the extrusion time can be correlated

with a certain transverse cross-section of wire.

From numerical simulation result, the path line of each particle has been recorded.

Therefore, the following three parameters are derived: the first one is exiting time t, which

is the time from the beginning of the process to the moment that particle entering extrusion

hole. The second one it exiting radius r, which is the distance to the central line when

particle enters extrusion die hole. The third one is angle Θ that particle rotated before

entering extrusion die hole.

The volume of the entire region of real marker material is actually much larger than

the volume that discrete particles can represent. So the information from the simulation is

not sufficient to compare with experiment observation. It is necessary to derive information

between placed position and press close to real marker, a solid bar. Curve fit was carried

for t, r and Θ, respectively, among the z-r plane where particles are placed. Polynomial

function from 1 to 7 order of were tried and the best fit was selected. Therefore, the function

of t, r and Θ on the z-r plane at marker region are determined. The mathematical method

of curve fit is described in appendix A. For material point located in marker area but out of the z-r plane, its exit time t, exit radius r and rotated angle Θ should be identical with values of the point located at the z-r plane which has same initial radius and height with it.

Now, the exit time and position of material on entire marker zone are derived. To determine how many points are enough to draw marker in transverse cross-sections, the average grain size of AA2195 in extruded wire is used as the volume of each point represented. After t, r and Θ of all points are reached, these points are sorted by time. For each point, add the initial angle Θ_0 with Θ, we have exit angle Θ_1. So the final position of each point when it entering extrusion hole are determined. The exit time t is calculated to correspond with examined transverse cross-sections of extruded wire. Plot the final positions of points which exit around t, the marker redistribution figure from the result of numerical simulation can be drawn. Detailed Matlab code is given in appendix B. As many as thousands of data points can be obtained by the above method. The time when a particle reaches the exit hole determines its longitudinal position in the wire since the extrusion rate is known. As a result, the particles and the marker material on same wire cross sections can be compared.
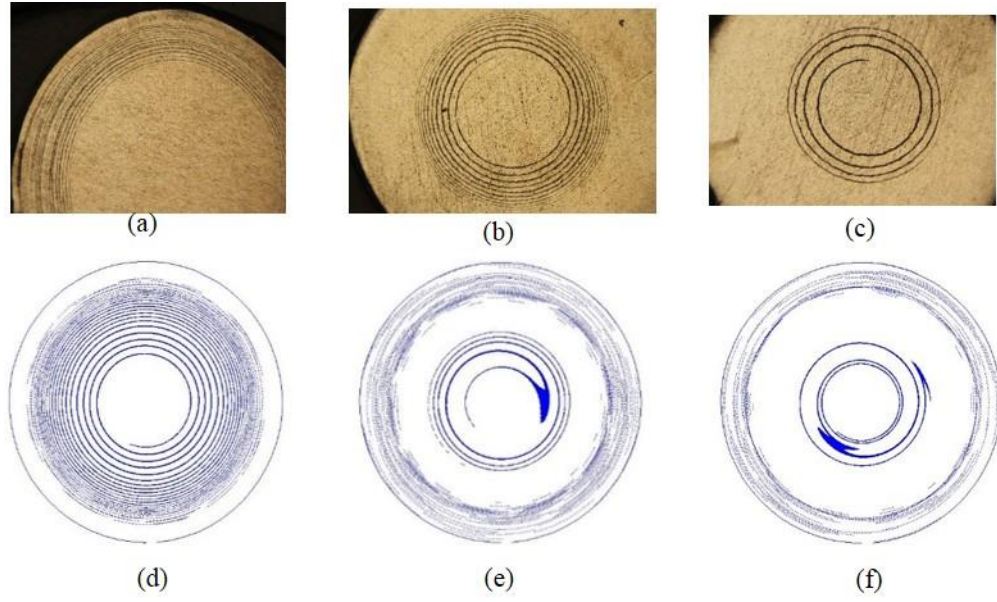
Figure 3.55 Comparisons of marker positions on wire cross sections (a) t = 13.0 s, experiment; (b) t = 16.9 s, experiment; (c) t = 18.8 s, experiment; (d) t = 13.0 s, simulation; (e) t = 16.9 s, simulation; and (f) t = 18.8 s, simulation.

Figure 3.55 shows the comparisons between the marker material in the experiment and the numerical predictions after interpolation between the particles in the modeling on extruded wire cross sections. Figure 3.55 (a)-(c) show experimental results, the marker material distribution on extruded wire cross sections at different moments. The marker material used in the experiment shows a dark color after chemical etching. Figure 3.55 (d)-(f) show the numerical results. It can be seen that they share some features in common, such as (a) the markers form continuous spirals on extruded wire cross sections and (b) the revolutions of the spirals on the cross sections decrease as extrusion continues. However, some differences exist between the simulation and experimental measurements. The discrepancies are mainly due to some assumptions made in the modeling. Nevertheless, the qualitative comparisons indicate that the material flow trends can be captured.

94

In the modeling, the particle markers released in the precursor material flow with it and leave continuous trajectory paths. Since the particles are massless, they follow the nearby material all the time and thus their trajectory paths represent the nearby material paths. Studying the paths of particle markers can help understand how the precursor material in the chamber flows and how the extruded wire is formed. It is worth to note that numerical modeling is able to provide a vivid visualization that is not available in the experiment. Figure 3.56 depicts the path lines of the particle markers with different initial positions in the simulation. The initial heights of these path lines range from 15 mm to 18 mm. Every path line has a unique color. For a better view, the figures don't have the same scale. Figure 3.56(a) shows a group of path lines which originate from one-third of sample radius from the center. All of these path lines go through the extrusion hole, indicating that the material there is extruded out of the chamber to form the wire. Before reaching the extrusion hole, all path lines have experienced spiral shapes which feature decreasing radii and increasing heights. For those path lines who have higher initial heights, their spirals have more rotations. The spirals are the consequence of the rotating die which is stuck by the material at the die-sample interface. Near the interface, material has larger tangential velocity and thus experiences more rotations. This can explain those path lines with more spirals. The path lines with lower initial heights have more obvious height increase. The decreasing radii of spirals show the material flows toward the center and the increasing heights indicate that the material has vertical velocity. All of these imply that there is

95

material in the central region being pushed spirally upward the extrusion hole. Figure 3.56(b) shows pathlines of particles which are released at positions with a distance 7.2mm from the center (The sample radius is 12.5 mm). Only some of the path lines which have lower initial positions reach the extrusion hole, meaning that the material in that region with lower heights flows out of the chamber to compose the extruded wire while those with higher heights stay in the chamber all the time during the process. The path lines with lower initial heights show the material there also is pushed to both the center and the extrusion hole spirally. The spiral shapes of the particles with higher initial heights are different. Since they stay in the chamber all the time and in the higher velocity region they have experienced more numbers of spirals. During the friction extrusion process, the die moves down gradually, pushing the material just under it down. As a result, the heights of these particles decrease slowly. Figure 3.56(c) show the path lines whose initial positions are 10.4 mm away from the center. Apparently, none of the particles pass the extrusion hole and no material there goes out of the chamber. The number of spirals is obviously less due to the region has small velocity. Likewise, the radii of the path lines with lower initial heights decrease but with a slight variation. Pathlines in Figure 3.56(b) and (c) show that there exists a dead zone as in traditional extrusion process where the material can never be extruded out of the chamber. From die surface to 4mm below die surface, the dead zone includes at least the region from 2/3r to 1r in radial direction.
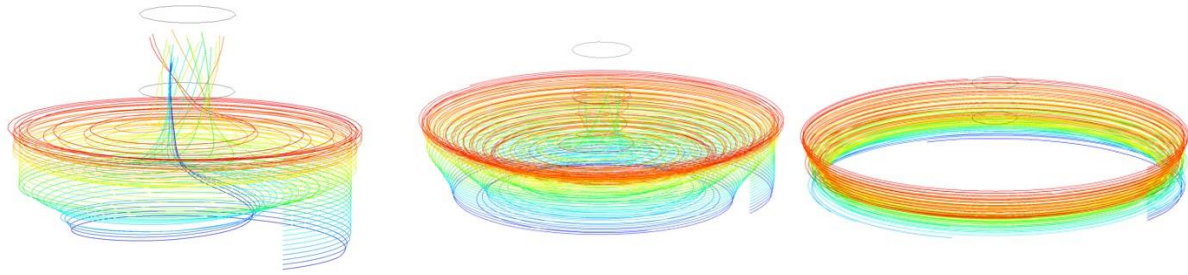
Figure 3.56 Path lines with initial positions at (a) r = 4.3 mm (b) r = 7.2 mm (c) r = 10.4 mm from the center

3.2.7 Post-extrusion drawing

3.2.6.1 Effect of annealing and reannealing

The theoretical true strain ε from work hardening in a drawing step can be calculated by:

$$\varepsilon = \ln\frac{A_0}{A_f} \qquad \text{Eq (3.12)}$$

Where, A_0 and A_f are the areas of cross-section before and after drawing respectively.

The engineering strain e can be expressed as:

$$e = (\frac{A_0}{A_f} - 1) \qquad \text{Eq (3.13)}$$

As shown in Table 3.5, the theoretical strain introduced by corresponding draw step was listed.

Table 3.5 theoretical strain introduced by corresponding draw step

Diameter(mm)	2.7	2.6	2.5	2.4	2.3	2.2	2.1	2	1.9
A_0/A_f		1.0784	1.0816	1.0851	1.0888	1.093	1.0975	1.1025	1.108

97

True strain	0.0755	0.0784	0.0816	0.0851	0.0889	0.093	0.0976	0.1026
Engineering strain	0.0784	0.0816	0.0851	0.0888	0.093	0.0975	0.1025	0.108

Diameter(mm)	1.8	1.7	1.6	1.5	1.4	1.3	1.2
A_o/Af	1.1142	1.1211	1.1289	1.1378	1.148	1.1598	1.1736
True strain	0.1081	0.1143	0.1212	0.1291	0.138	0.1482	0.1601
Engineering strain	0.1142	0.1211	0.1289	0.1378	0.148	0.1598	0.1736

To quantify the effect of annealing and reannealing, Vickers hardness testing was performed on as-extruded condition, as-drawn condition and annealed condition with varying annealing time. The hardness values are shown in Figure 3.57 with the value of AA5356 commercial weld wire and AA2050 base metal. The as-extruded wire has only half hardness compared with base metal. As annealing time increases, the hardness of friction extruded wire decreases. From 0 to 10 minutes, it dropped from 95 to 76 HV. From 10 minutes to 60 minutes, it slightly dropped from 76 to 66 HV. That means along with annealing time goes, friction extruded wire got softer. The most of the annealing effect was introduced in first 10 minutes.
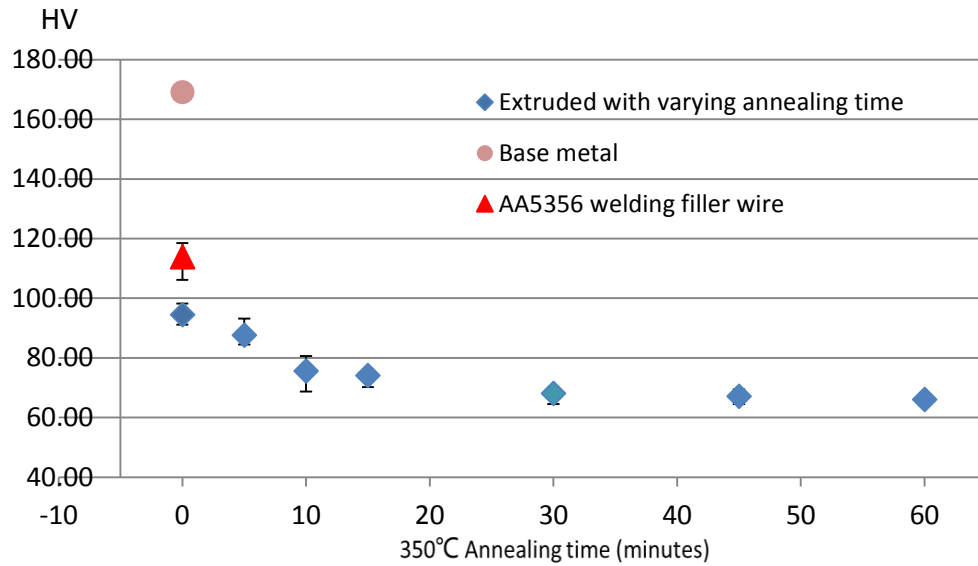
Figure 3.57 Vickers hardness of friction extruded wire with varying annealing time, base metal and AA5356 welding wire

After 60 minutes annealing, the wire was drawn from Φ2.7mm to Φ2.6mm and reannealed. The effect of reannealed time on the hardness of wire are shown in Figure 3.58. It indicates hardness increased from 66 to 82 HV after drawing. With 5 minutes reannealing, it decreased to 74 and didn't change much with longer annealing time. Therefore, 5 minutes is appropriate reannealing time to ease work hardening caused by post-extrusion drawing.
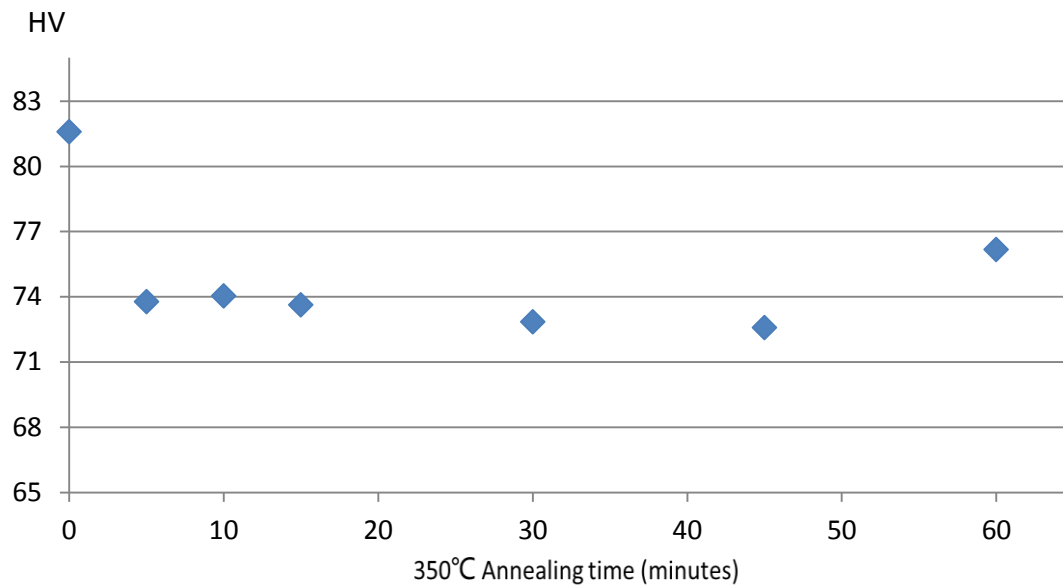
Figure 3.58 Vickers hardness of friction extruded wire with varying reannealing time, at true strain equals to 0.076

The microstructure of transverse cross-sections of friction extruded wires with varying annealing time are presented in Figure 3.59. The as-extruded wire has equiaxial grain structure with about 17 μm grain size and abnormal huge grains on the peripheral region of the cross-section. Along with annealing time increases, all grains recrystallized to smaller grain. After 10 minutes annealing, the grain size is smaller than 2 μm, which is unmeasurable with the maximum magnification of our microscopy.
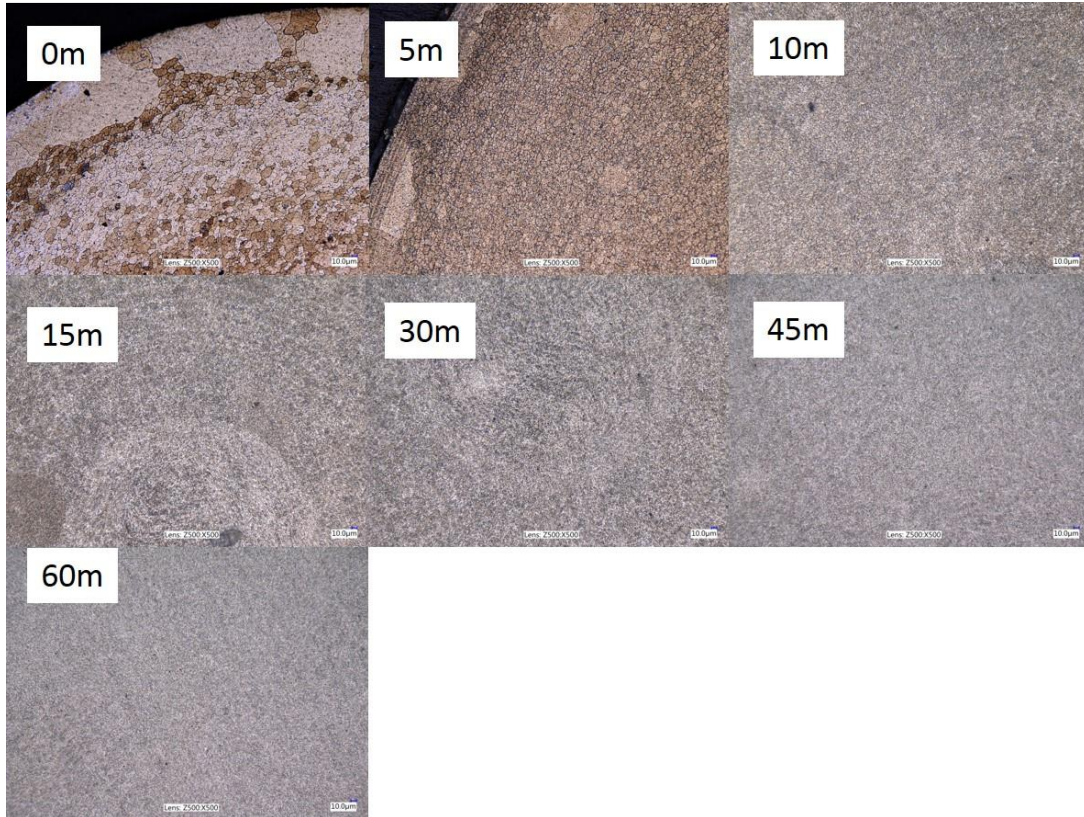
Figure 3.59 Micro-structure of AA 2050 friction extruded wire with different annealing time

3.2.6.2 Wire producing and post-extrusion drawing for additive manufacturing

Firstly, AA2050 wires with 1.8mm, 1.6mm and 1.2mm diameters were produced using corresponding die hole size. The lengths of them are shown in Table 3.6. Compared with 3 meters long wire with 2.54mm in diameter, though longer wires were obtained, they are still not long enough. What's more, wire break happened during drawing with current setup that is no heat-treatment applied. Dies with larger diameters 4 to 6 mm were introduced to make a rod first which is not easy to be break. After few tries with 4-6mm die hole size, a friction extruded rod with 6mm in diameter, 1.854 meters in length was extruded with good surface quality and no breaking. It was drawn to a thin wire with 1.6mm

in diameter, about 20 meters in length, shown in Figure 3.60. With such diameter and

length, it can be applied as filler wire to build an additive manufacturing sample.

Table 3.6 lengths of wire made with different die hole size and rotational speed

RPM	die hole diameter(mm)	length(m)
200	1.8	4.902
200	1.6	5.004
200	1.2	8.636
200	4	1.854
150	4	1.854
115	5	1.245
115	6	1.854

Figure 3.60 AA2050 drawn friction extrusion wire, 1.6mm in diameter

3.3 Discussion and summary

Several of the presented results may be used altogether to gain a picture of how the friction extrusion process, as performed in this study, evolves.

1) By analogy with friction stir welding, it was assumed that because the grain size increases with wire length, the extrusion is occurring under conditions of increasing temperature. The increasing temperature is due to uncontrolled heating of the extrusion apparatus resulting from continuous heat input via dissipation of plastic work and insufficient heat transfer away from the apparatus to maintain a steady state. This observation is consistent with the simulated result of the friction extrusion process.

2) In-plane deformation and, hence, strain, decreases with increasing extrusion length: that is, the extrusion becomes more like a "conventional" extrusion and the major working direction moves toward the extrusion direction and away from the die rotation direction. However, in all cases, the major working direction is closest to the extrusion direction near the center of the wire. It may be surmised that this corresponds with a greater extrusion length per die revolution. Since the extrusion pressure is constant, this indicates a reduction in flow stress presumably due to an increase in temperature as described in (1) above.

3) Material flows in spiral line in friction extrusion process. The material located

between center and 1/3 radius gradually move into central extrusion hole as a spiral line. Both experiment and simulation show that dead zone exist in friction extrusion as well as in conventional extrusion. Die tip pattern, extrusion ratio, experimental parameter can change the shape of flow pattern and dead zone. More precise simulation can help predict the entire material flow field.

4) Higher rotational speed, which corresponds to higher power input accelerates the evolution of the process toward "conventional" extrusion. This phenomenon can be explained by the following assumption: more power input will increase processing temperature, so the material's flow stress is lower and mobility is better. In other words, the extrusion rate is higher. Even though the rotational speed is higher, the marker material with higher mobility experiences fewer revolutions for production of a unit length of wire. The longitudinal deformation is stable during the process despite using different rotational speeds and extrusion forces: this reduction is governed solely by the ratio of die hole area to billet area.

5) <100> recrystallization texture is strongest in the hottest part of the wire (that extruded last) and for all cross sections, nearer the center.

    a. The hottest part of the wire has the most nearly uniform major working direction (the extrusion direction) evidenced by minimized marker spiral patterns and lowest in-plane strain.

    b. The region of strong <100> texture is largest for wire extruded later in the

process and decreases with decreasing grain size and hence, reduced temperature.

c. The strongest <100> texture corresponds to regions and conditions for which the major working direction is most nearly the extrusion direction.

6) In order to ensure that consistent levels of strain are produced during the friction extrusion process (e.g. as might be required for full consolidation of a finely divided charge or for homogenization of a cast billet), it will be necessary to control the die revolutions per unit length of extruded wire while processing.

A thermal-fluid finite element model was validated by verifying temperature curve and redistribution of marker material. The thermal history of the extruded wire is of great interest since it is expected to play an important role in determining the mechanical properties of the extruded wire. Figure 3.61 depicts the predicted thermal histories at the center of the die/sample interface where the extrusion hole exists and at the center of the bottom of the sample cylinder, respectively. The predictions show that the temperature at the extrusion hole increased rapidly and then held steady after the start of wire extrusion, which is very similar to the temperature measured experimentally at point 2. In the 'steady-state" region the temperature at the extrusion hole varied from 833 K to 848 K. At the end of the extrusion, the temperature at the hole was 853 K, which was very close to the solidus temperature of 855 K. For comparison, the temperature at the center point of the bottom of the sample cylinder varied smoothly from 596 K to 711 K.
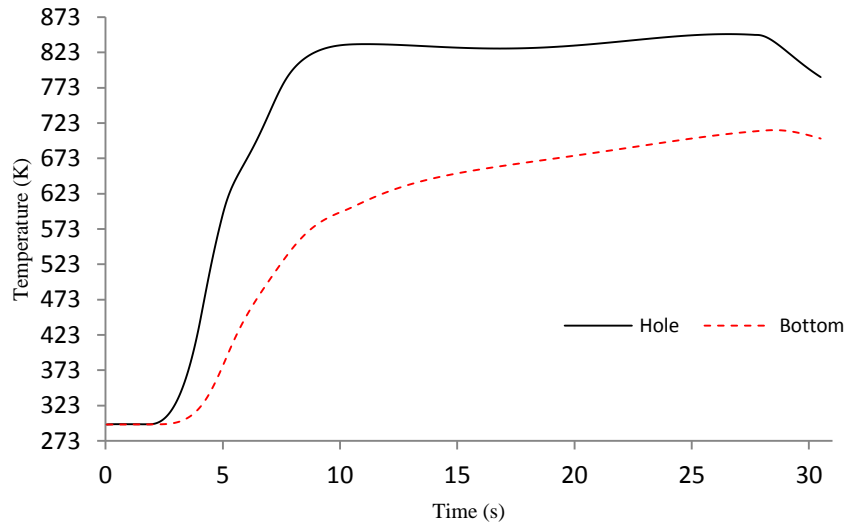
Figure 3.61 Predicted temperature in the hole and the bottom of friction extrusion

The temperature predictions from the thermal model agree reasonably well with experimental measurements, thus providing a good validation of the proposed thermal model. From the results of this study, the following conclusions can be made: (1) The volume heat source method can be used to reasonably represent the heat source in the friction extrusion process; (2)The initial gap between the sample and the chamber wall needs to be modeled in order to properly capture the heat transfer phenomenon; (3)The thermal contact between the billet charge sample and the back plate is not perfect based on comparisons between predictions and experimental measurements, and its complication needs to be further studied; (4)The extruded wire experienced a small range of temperature history during extrusion that varied in a small range somewhat below the solidus temperature.

Apply post-extrusion drawing can improve the applicability of extruded wires in the following ways: (1) obtain desired diameter, (2) improve surface finish, (3) extend the total length. Annealing and re-annealing can alleviate work-hardening brought by drawing to prevent wire breaking in the posterior drawing. Proper heat treatment time: 10 minutes for first annealing and 5 minutes for reannealing are suggested for the AA2050 wire.

In sum, aluminum alloy wires were made via friction extrusion using FSWPDS and modified milling machine. The thermal-mechanical progress of friction extrusion process was revealed by analyzing the variation of force and die movement during the process. Marker insert technique was employed to exhibit material flow, highlight effect of experiment parameter and deduce strain in the wire. The equiaxial grain structure and texture of friction extrusion wire was found by optical and electronic microscope. Post-extrusion drawing and annealing was applied on extrusion wire to make it more suitable for a downstream process like additive manufacturing.

CHAPTER 4

FRICTION CONSOLIDATION

4.1 Aluminum chips consolidation

4.1.1 Experiment design

4.1.1.1 Apparatus and materials

The friction consolidation equipment is composed of the following four parts: die, chamber, back plate and FSWPDS. The consolidation die is fabricated with H13 tool steel with a dimension of Φ25 mm X 114.3 mm cylinder shape, see Figure 4.1. The die tip pattern is a scrolled surface. The scroll die is rotated in a clockwise direction (when die tip faced downward as in experiment setup) so that the scroll pattern can gather plastic-state material toward the center.

Figure 4.1 Friction consolidation scroll die

Figure 4.2 Billet chamber used in friction consolidation

The chamber has a wider shoulder ring outside with two semicircle breaches for being fixed on the back plate, see Figure 4.2. The chambers were fabricated with O1 tool steel. The inner diameter of the stationary 'billet' chamber is 25.4mm. A stainless steel plate is adopted as the back plate for fixing the chamber and supporting aluminum chips. Four thermocouples are placed in several locations on the chamber for collecting temperature data, shown in Figure 4.3. Three thermocouples were placed on the chamber outer surface. They are located at the top of the chamber, the corner of the chamber

shoulder and the bottom of the chamber, respectively (point 0, 1, and 2). Close to the

chamber inner wall, one thermocouple was placed at 18mm (point 3) far from the back

plate.
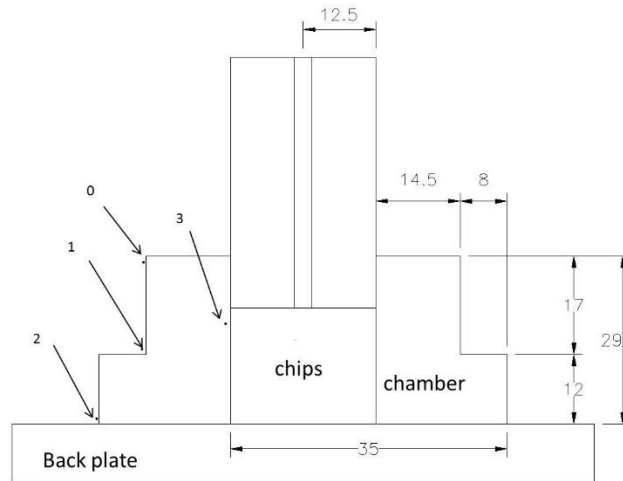
Figure 4.3 Location of thermocouples in friction consolidation

For parameter comparison experiments, the FSW PDS (Friction Stir Welding

Process Development System) was used to implement the friction consolidation process.

Key features of the PDS are a rigid steel table and a hydraulically driven spindle which is

able to rotate and generate pressure for consolidation, see Figure 3.5. Using this machine,

the process is performed under force control which can lead to varying die advance speed

(motion of die into the billet chamber). The axis of die rotation and die advance is vertical

to the table.

Aluminum alloy 6061 (Al-1.0Mg-0.6Si-0.6Fe-0.25Cr-0.2Cu) is a medium strength precipitation hardening alloy that is commonly used in a wide variety of structures.

In order to prepare AA6061 chips with uniform size as precursors, desired thickness of AA6061 chips were made by milling according to equation (4.1):

$$t_c = \frac{2v}{Nn} \sqrt{\frac{d}{D}} \qquad \qquad \text{Eq (4.1)}$$

Where t_c is the average thickness of chips, N is the rotational speed of the cutter, n is the number of teeth on the cutter periphery, d is the depth of cut, D is the cutter diameter, and v is the linear speed (feed rate) of the workpiece. The parameters adopted for making 75.8um thick chips with 3 different lengths are listed in Table 4.1.

Table 4.1 The machining parameters adopted for producing 75.8um thick chips with different lengths

No.	N(rev/s)	n	d(mm)	D(mm)	v(mm/s)	Chip length(mm)
1	2.13	4	0.5	19.05	2	6.35
2	2.13	4	0.5	19.05	2	3.18
3	2.13	4	0.5	19.05	2	1.59

4.1.1.2 Procedure of fully processed friction consolidation

The experimental procedure of a fully processed friction consolidation process can be described as below: after the backing plate and billet chamber are aligned with the rotational axis of the PDS, they are clamped to the PDS table using finger clamps. Subsequently, the chamber is loaded with the desired weight of chips. After loading, the chips are pre-compacted by applying a force of 8900 N for ten seconds. During this pre-compaction, the die does not rotate. The compaction force is reduced to zero and then raised

to 2225N at which time the die rotation is started. Once die rotation has begun and the spindle rotating at the desired rate, the compaction force is raised to the desired value and maintained for the specified time. Since load control was implemented, displacement of die position was monitored as a reference of when friction consolidation was fully consolidated. While the motion of die is not obviously moving forward or drifting around, we consider billet charge are fully processed with designed experimental parameters. Then, the die will be raised and the process finished. The rotation speed, die position and Z-force (consolidation force) were recorded by the FSW system control computer with 10Hz sampling rate. The rotating torque and power were recorded by a torque transducer mounted on the machine spindle with at least 40Hz data collection rate. In these study, 400rpm die rotational speed and 17.8kN force were implemented. 10 grams chips No.2 (see Table 4.1) were used as precursor. At about 45s, they were considered fully processed.

4.1.1.3 Procedure for partial consolidation study

A series of partial friction consolidation experiments were carried with gradually decreased processing time (from die start rotation to end of the process). The experimental parameters are 400*rpm* and 17,800*N* consolidation force. At this parameter and chip size, the full consolidation processing time is about 45.1 seconds (determined from the preliminary consolidation study). The experiments were run with 42.3s, 30.9s, 19.2s, 12.5s and 6.1s processing time. After experiments, the processed billets were cut in half vertically along the radial direction and then examined metallographically.

4.1.1.4 Consolidation parameter study

There are three sizes of aluminum chips have been prepared using parameters shown in Table 4.1: 6.35mm long, 3.18mm long and 1.59mm long, all are 75.8µm thick. They were friction consolidated separately to study the effort of chip length on the quality of the consolidated material. 10 grams of chips were used as the billet charge for each consolidation run. The process parameters were 400*rpm* and 17,800*N* force for these experiments. All three experiments were applied with 50 seconds processing time.

4.1.1.5 Consolidation parameter study

The effects of various control parameters on the fraction of billet charge consolidation were studied systematically through the statistical orthogonal design of experiments (DOE). There are three control parameters: Z-force, which is consolidation force; die rotational speed and processing time. For each parameter, 3 levels are picked. Their values are presented in Table 4.2. Here, 15 grams AA6061 chip was used as precursor in each experiment.

Table 4.2 Adopted control parameters in design of experiments

Factor	A RPM	B Z-force(N)	C Process time(s)
1	200	8900	15s
2	300	17800	30s
3	400	26700	45s

To reduce the number of experiments, Orthogonal table $L_9(3^3)$ is used, order of experiments are randomly sorted, shown in Table 4.3:

Table 4.3 $L_9(3^3)$ orthogonal table of design of experiments

DOE	factor		
Order	A	B	C
3	1	1	1
6	1	2	2
8	1	3	3
1	2	1	2
5	2	2	3
9	2	3	1
2	3	1	3
4	3	2	1
7	3	3	2

4.1.1.6 Post-consolidation analysis

The consolidated portion of the charge was carefully removed from the chamber and considered as consolidated disc. The rest of material includes the unconsolidated chips and the material left on tool and chamber. The mass of consolidated disc was weighed by digital scale accurate to 0.0001 grams. The height and diameter of the consolidated disc were measured using a caliper. Then, the density/state of porosity was calculated for comparing with the standard base metal material. For analyzing the void state and deformation depth throughout the product, the consolidated discs were cut horizontally or vertically, then ground, polished and etched (Keller's etchant: 190ml water, 2ml HF, 3ml HCl, and 5ml HNO_3) to reveal the macro-structure. Optical microscopy was used to show the microstructure variation along the radial direction and vertical directions on consolidated discs.

4.1.2 Results and analyzes

4.1.2.1 Progression of the friction consolidation process

A fully processed friction consolidation experiment was implemented at 400rpm, 17.8kN force. The position of the die is monitored during the process to make sure at last the die cannot move advance anymore which means the material is fully consolidated and the process is finished. Although force control has been adopted in our study, the compressive force feedback is not constant before the material is mostly consolidated. The variation of force feedback indicates the tendency that billet material transitions from discrete and loose condition to an integrated block. The velocity of die movement largely slows down after 10 seconds due to the diminishing of the gap between chips. In Figure 4.4, the compressive force feedback and position of the die are presented. Here, the moment when the die starts rotating is defined as the beginning of the process. At that moment, the die is in contact with metal chips since $2225N$ force is applied. We consider this position of the die is at zero and the direction of the compressive force is negative. The power input history is presented in Figure 4.5. From 0s to about 9s, the Z-force and power rapidly increase to a peak, and the die quickly moves down about 9mm. The volume of material is largely compressed due to the Z-force and increased temperature. So, this period can be described as compaction. The difference between it and pre-compaction is that die is spinning so heat dissipation softens the material. From about 9s to 45.1s, the position of the die doesn't significantly change. The friction between die tip and the top layer of

aluminum chips brings about heat and subsequently temperature increasing. With higher

temperature the flow stress of the material is lower. In other word, material is softened and

enabled better mobility. Under high compressive force and torque, these finely divided

chips are "welded" together. In addition, the severe plastic deformation provides heat

dissipation to the chips beneath the top layer which is in contact with the die. So lower

material are gradually turned into plastic state and friction consolidated. While the motion

of die is not obviously moving forward, we consider billet charge are fully processed with

designed experimental parameters. At about 45 seconds, this vibration is stable so process

was terminated. This period can be described as consolidation.
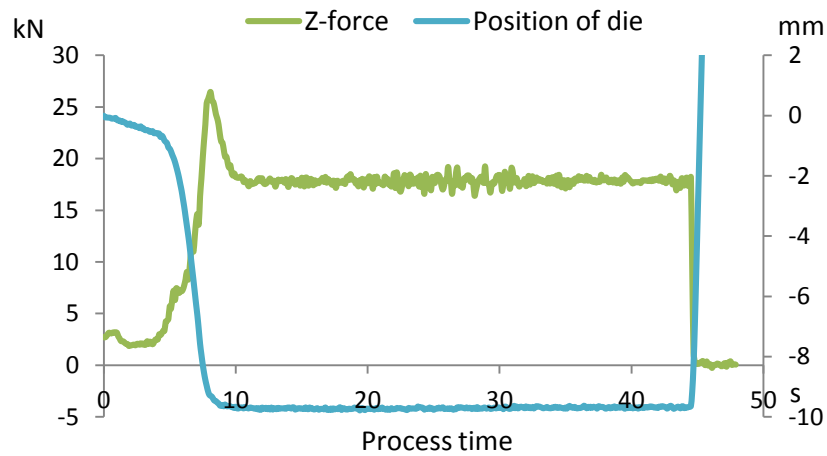
Figure 4.4 Z-force and position of die in friction consolidation
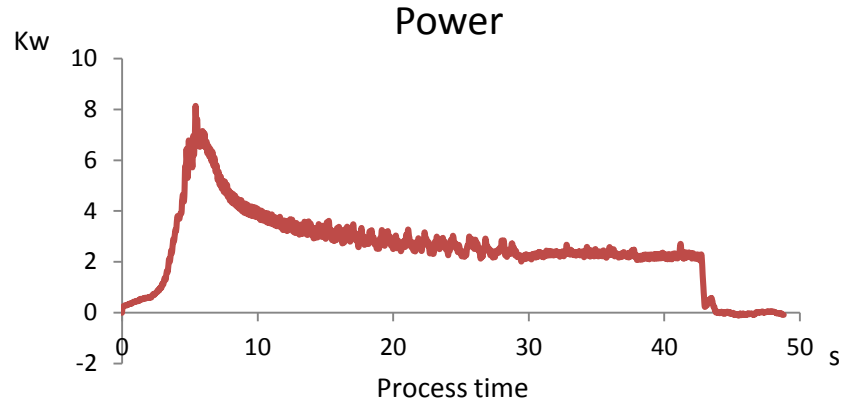
Figure 4.5 Power history in friction consolidation

The vertical cross-sections were ground, polished and etched using Keller's solution. The scanned pictures of macro-structure are shown in Figure 4.6. After the experiment with 6.1s processing time, a considerable amount of material at the bottom are still loose chips that don't attach on sample (a). So, only part of billet charge is shown here. Most of the sample is shown in (a) is unconsolidated because the process is still in the compaction period. The pictures of sample (b) to (f) show that aluminum chips were transformed into a solid disc for longer processing times. Their cross-sections can be divided into two regions by a bowl shape borderline, see sample (d) as an example. No.1 is above borderline and No.2 is below it. Along with increasing processing time, the borderline is moving down and getting clearer. The area and area fraction of region 1 vs. processing time was presented in Figure 4.7.

117
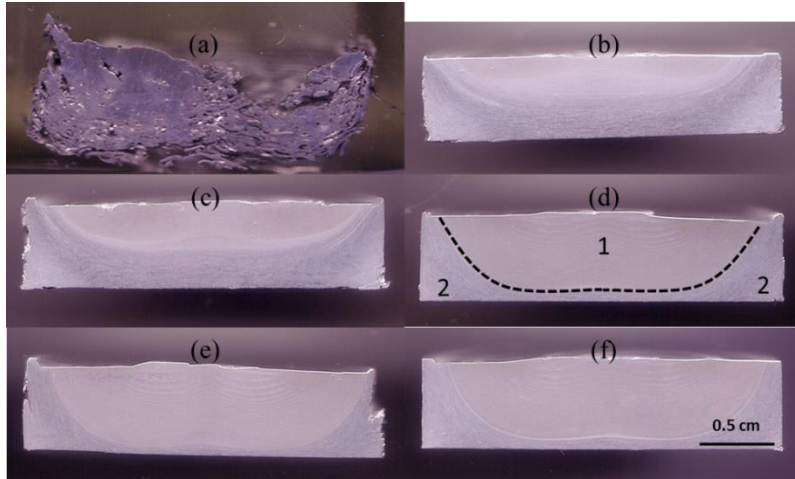
Figure 4.6 Cross-sections of series of partial consolidation discs, from (a) to (f): 6.1s, 12.5s, 19.2s, 30.9s, 42.3s, and 45.1s processing time
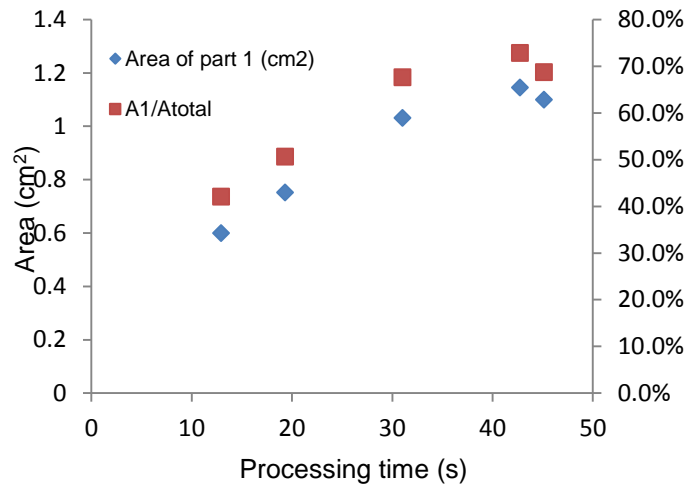
Figure 4.7 Effect of processing time to fully consolidated area

Microstructure images were taken on disc (f) using an optical microscope, see Figure 4.8. Fine recrystallized equiaxed grain structure is observed in the whole of region 1. Also, a well-defined, layered structure was observed, shown in Figure 4.8(a). This banded structure could be flow patterns cause by thermal-mechanical cycle during processing. It appears quite similar to onion ring nugget structure found in friction stir welds [21], [77]. The inner spacing between two layers was marker from 1 to 23, from

center to side, and measured, see Figure 4.9. The result shows space is getting smaller from

center to side. In region 2, the grains are more or less elongated along the direction tangent

to the boundary of regions 1 and 2, Figure 4.8(e) and (f). Unbonded regions can be observed

in region 2 particularly near the lower corners, Figure 4.8(c) and (d).
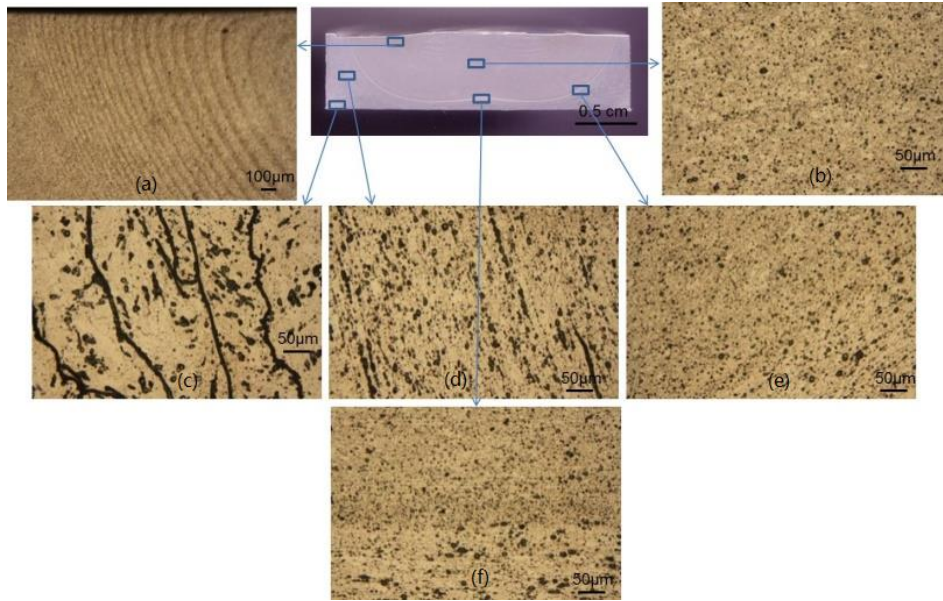
Figure 4.8 Microstructure of fully consolidated disc, (a) and (b) layered structure and fully consolidated zone, (c) and (d) unbonded regions, (e) and (f) grains elongated along tangent direction of boundary
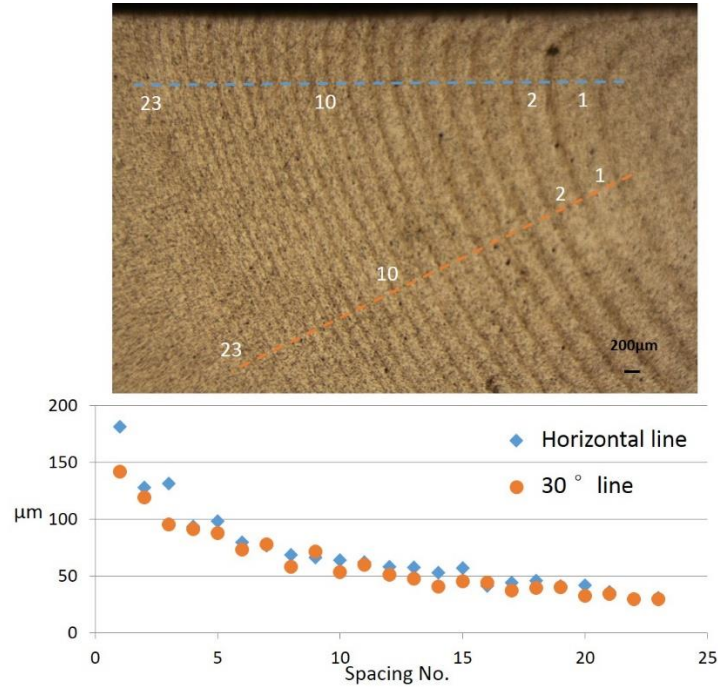
Figure 4.9 length of space between layered structure in fully consolidated zone

Based on above observations, we can learn that region 1 has better consolidation status than region 2 and can be considered as fully consolidated part. With longer processing time, region 1 will be extended further to the peripheral side and bottom of the disc and thus result in fuller consolidation. But even with longest processing time, there are still some gaps that cannot be consolidated at the bottom of the die chamber near the vertical walls.

Grain size was measured for all samples the recrystallized zone where located at 3.35mm below top center, the results are shown in Figure 4.10. Grain growth happened along with processing in the recrystallized zone and reaches a plateau after 20 seconds of processing time.
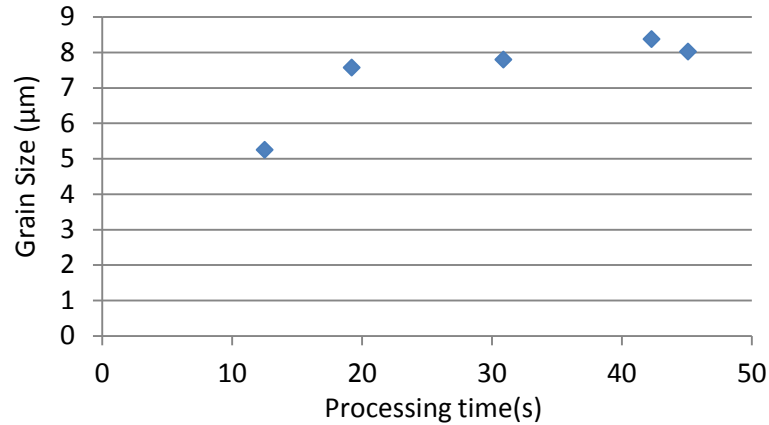
Figure 4.10 Variation of grain size with different processing time

4.1.2.2 Precursor dimension effect

There are three sizes of aluminum chips have been friction consolidated separately: 6.35mm long, 3.18mm long, 1.59mm long, all are 75.8μm thickness. The process parameters are 400*rpm* and 17,800*N* force for these experiments. Same processing time 50 seconds have been applied in all three experiments.

The top and bottom view of these three runs are shown in Figure 4.11. The center and peripheral region at both sides were checked carefully. No obvious voids or cracks were found in appearance and no big difference between each other, which indicated that all three kinds of aluminum chips can be successfully made into solid disc via friction consolidation.
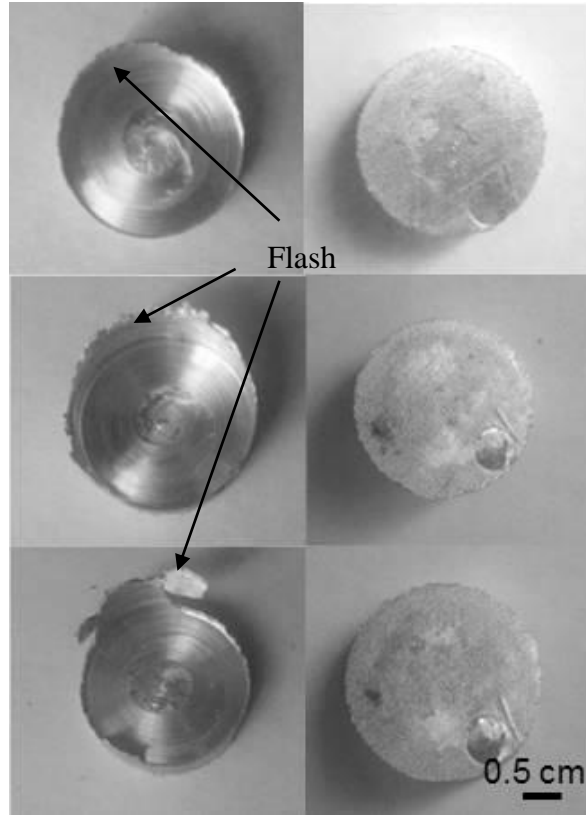
Figure 4.11 Friction consolidated disc with flash on top made with 6.35mm long (top), 3.175mm long(middle), 1.588mm long(bottom) AA6061 chips, top view on left and bottom view on right.

After removing the flash on top, the height and radii of the disc were measured. Then, the volume of the disc was calculated. The weight of disc was measured by a precise digital balance. So the overall density of consolidated disc was derived, see Table 4.4. For all conditions, the density of friction consolidated disc is very close to 2.61×103 which is the density of standard AA6061. No significant difference is found between using precursors with different length. This result is consistent with the finding in hot profile extrusion [78]. The energy input is derived from power history. Results indicate that similar energy is consumed among three kinds of chips, see Table 4.4.

Table 4.4 Density of consolidated discs with different precursor length

	Consolidated disc with different chip length (mm)		
	6.35	3.18	1.59
Density (kg/m3)	2.63×103	2.66×103	2.61×103
Energy input(kJ)	109	114	112

4.1.2.3 Design of experiments for parameter effect study

After each of the nine randomized experiments, the processed material was carefully removed from the chamber. All discs' top region are well consolidated. However, only samples No.5, No.7 and No.8 were fully consolidated. The density of each disc was calculated and presented in Table 4.5. Above discs were cut into half vertically. The vertical mid-plane cross-sections were etched and scanned as shown in Figure 4.12.
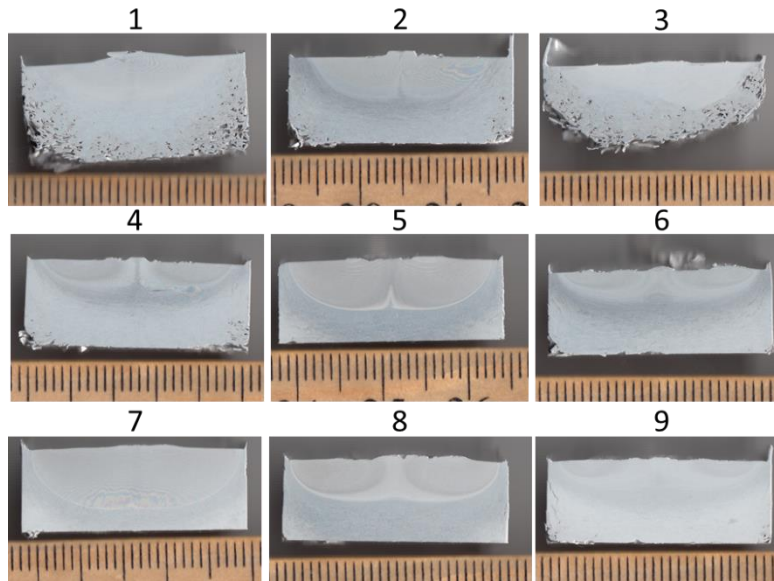
Figure 4.12 Vertical cross-sections of friction consolidated discs in DOE experiments

As stated in 4.1, the cross-sections of processed disc are divided into two regions by the bowl shaped borderline: fully consolidated region above the border and partially consolidated region below the border. In order to evaluate the fraction of consolidation, the volume of the fully consolidated region needs to be calculated. For each cross-section, we turn over the picture upside down and then set the origin of coordinate at the middle bottom of the disc. The function of borderline is mathematically derived by subsection curve-fitting, see Figure 4.13 as an example.
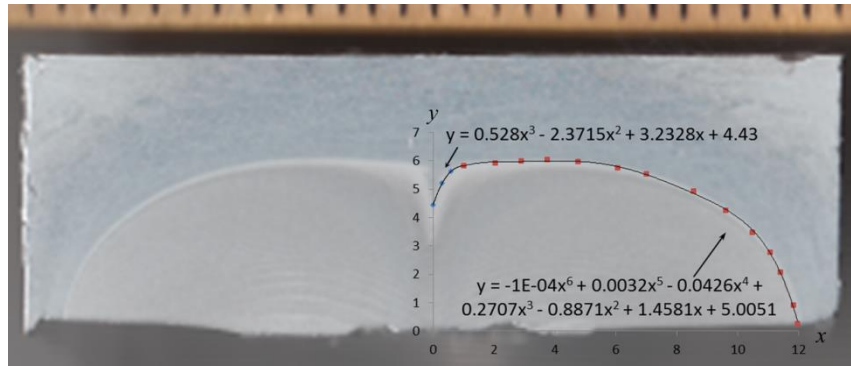
Figure 4.13 Curve fit for the borderline of disc No.5 (upside down)

Due to central symmetry (except disc No.3), the volume of fully consolidated region V is formed by half of recrystallized area on vertical cross-section revolving around the central axis. Here it can be written as:

$$V = 2\pi \int_0^x xy\,dx \qquad\qquad \text{Eq (4.2)}$$

Where, y is the function of borderline. For sample No.3, the volume of fully consolidated region is the average V calculated from half left and half right recrystallized area.

The fraction of consolidation θ is defined as the ratio of volume of fully

consolidated region to the volume of solid AA6061 with same mass of billet charge:

$$\theta = \frac{V}{m_t/\rho_s} \qquad\qquad \text{Eq (4.3)}$$

Where, ρ_s is the standard density of AA6061, m_t is the total mass of billet charge.

In previous experiments, maximum fraction of consolidation is 73%.

The fraction of consolidation of all discs (except sample No.3) is presented in Table

4.5.

Table 4.5 Density and fraction of consolidation of friction consolidated discs with varied
control parameters

Sample No.	RPM	Z-force(N)	Process time(s)	Density （g/cm^3）	Fully consolidated volume (mm^3)	Fraction of consolidation θ
1	300	8900	30	2.15	872.1	15.7%
2	400	8900	45	2.86	1532.7	27.6%
3	200	8900	15	1.91	1243.2	22.4%
4	400	17800	15	2.74	1181.1	21.3%
5	300	17800	45	2.79	2024.6	36.4%
6	200	17800	30	2.81	1262.5	22.7%
7	400	26700	30	2.91	2645.6	47.6%
8	200	26700	45	2.79	1836.9	33.1%
9	300	26700	15	2.86	1375.7	24.8%

Based on above calculation, the correlation between fraction of consolidation and

experimental parameters are statistically established by Minitab software. As shown in

Figure 4.14, a main effect is the difference in the mean response between three levels of a

factor. Each point shows the mean value for all runs that used the corresponding

experimental parameter. The dash line show the mean for all runs in the experiments. Naturally all three parameters have a positive influence on fraction of consolidation. The effect of processing time is small at high processing times since complete consolidation occurs at finite processing time. This is consistent with the plateau in Figure 4.7 which indicates over certain processing time will not give better consolidation.
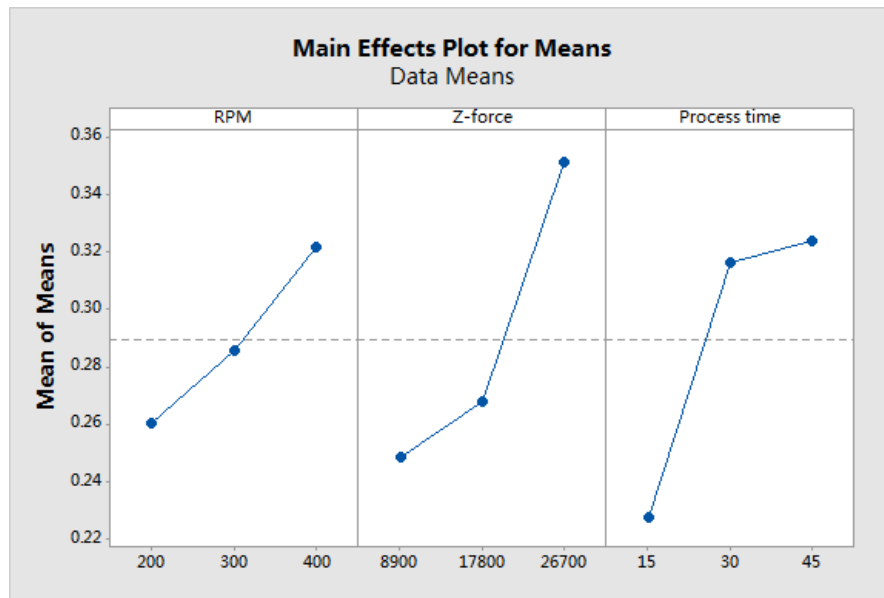
Figure 4.14 Main effects plot of RPM, Z-force and processing time on fraction of consolidation

4.1.3 Summary and discussion

In this study, aluminum alloy 6061 machining chips have been successfully consolidated to solid block via friction consolidation. Unlike in conventional recycling processes that involve melting and casting, in the friction consolidation process, material remains in solid-state. The deformation and temperature of material are both

inhomogeneous. It should be noted that they are coupled with each other since the plastic deformation is the heat source. The mentioned inhomogeneities exist in two directions: the radial direction of the die and advancing direction of the die. In the radial direction, the peripheral region has higher velocity and strain compared with the central region. Thus, the temperature is different also. In the direction of die advance, the contact surface between the die and the top layer of the billet charge is where friction takes place and thus generates most severe plastic deformation and highest heat flux. As the process progresses, the deformation zone and heat generation zone gradually expand from the region adjacent to contact surface to more remote regions. The evolution of material is fairly complex due to gradients in both temperature and deformation fields in both radial and die advancing directions.

Based on post-analysis of experimental data and consolidated discs, the underlying physical mechanisms are discovered and illustrated. The following conclusions are drawn:

(1) Friction consolidation process has two distinct periods: compaction and consolidation. In compaction period, material is largely compacted but not well integrated. The gap between material particles diminishes but welding of the chips to each other does not occur. In consolidation period, material density increases slightly. With a combination of high temperature and severe plastic deformation, a bowl shape fully consolidated region with recrystallized equiaxed grain structure is formed at the top of billet charge. With increasing processing time, the bowl-shaped

region gradually expands from top to lower part of the billet chamber but can't reach bottom corner even after long processing time.

(2) Three kinds of chips with different length are prepared to study the effect of the precursor size on the process. All of them are successfully consolidated. No obvious difference was found in the appearance of consolidated discs. The densities of discs are quite similar and very close to standard AA6061. The energy inputs are also similar to each other. In sum, the length of chips did not fundamentally affect process if the weight of material and processing time is fixed.

(3) The fraction of consolidation has been proposed to quantify the mass percentage of fully consolidated material. Maximum 73% has been reached in a fully processed friction consolidation. The effort of die rotational speed, compressive force and processing time on fraction of consolidation have been analyzed via design of experiments. All three parameters have a positive influence on fraction of consolidation. Over certain processing time, the effect of processing time will not give better consolidation.

4.2 ODS bead on plate

Oxide dispersion strengthened alloys (ODS alloys) can be defined as an alloy consist of a high temperature metal matrix - such as iron aluminide, iron chromium, iron-chromium-aluminum, nickel chromium or nickel aluminide - with small (5-50nm) oxide

particles of alumina (Al_2O_3) or yttria (Y_2O_3) dispersed within it. Iron-based and nickel-based oxide dispersion strengthened alloys exhibit good corrosion resistance and mechanical properties at elevated temperatures. These alloys also show excellent creep resistance, which stems partly from the dispersion of oxide and other particles, and partly from the very large elongated grain structure. ODS steels are being considered for use in nuclear fission applications[79].

Normally, ODS alloy is produced by mechanical alloying of powders. The metal and oxide (i.e. Yttria) powders are blended and mechanically alloyed using a ball mill. The repeated impacts of this process cause smearing together of the powders followed by shearing which generates particles that each contains a fine mixture of the constituents. This manufacturing process can be considered as a combination of shearing and consolidation, which is quite similar to friction consolidation. Also, ODS alloy has been successfully jointed by friction stir welding[80]. Therefore, it is worthy to study the potential of friction consolidation as an alternative way of producing or processing ODS alloy.

4.2.1 Experiment design and procedure

In this study, Incoloy MA956 iron-based ODS alloy is employed as billet material. The composition and thermal mechanical properties are listed in Table 4.6 and Table 4.7.

Table 4.6 Composition of Incoloy MA956

129

	Composition (wt %)					
Name	Fe	Cr	Al	Ti	C	Yttrium Oxide
INCOLOY MA956	74	20	4.5	0.5	0.05	0.5

Table 4.7 thermal mechanical properties of Incoloy MA956 at room temperature and 1000 ℃

Property	MA956	
Melting point (℃)	1482	
Density (g/cm3)	7.2	
	Room Temp	1000℃
Coefficient of thermal expansion (/K)	11.3x10 -6	14.9x10 -6
Thermal conductivity (W/m K)	10.9	25.5
Specific heat (J/kg K)	469	741
Electrical resistivity (μ Ω·m)	1.31	1.43
Modulus of elasticity (GPa)	269	191

Due to the high melting temperature of MA956, tool steel is not capable of die and

chamber material. So, W-La was adopted as die material for its sound strength and hardness

in high temperature above 650℃. The die surface is also scrolled as shown in Figure 4.15.

Instead of using chamber, "bead on plate" experiment is employed for saving material and

preparation time. The ODS friction stir consolidation is also carried by FSW PDS.

Figure 4.15 Scrolled surface of consolidation die used in ODS consolidation

The thickness of MA956 plate is 6.35mm. For visualizing the material flow and redistribution, stainless steel wire is employed as a marker material in the MA956 bead on plate experiments, as shown in Figure 4.16.
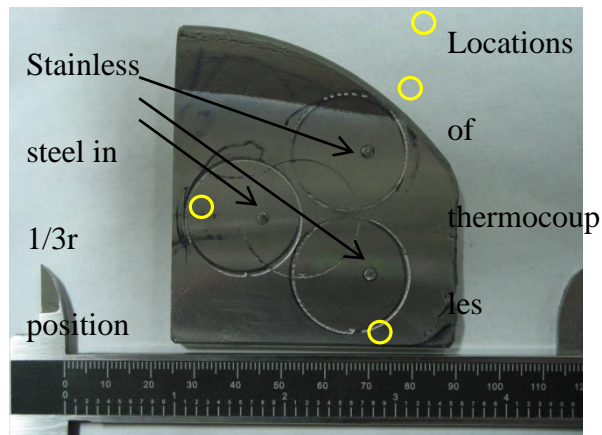
Figure 4.16 MA956 plate, three circles with markers in 1/3r position

At first, circles with same diameter (25.4mm) of die cross-section are drawn on MA956 plate for outlining the process area. A single intact experiment will be performed with each circle. Then through holes with 1/10 diameter of die cross-section were drilled

131

on 1/3 radius position of each circle for placing stainless steel marker segment. As shown in Figure 4.16, three circles were drawn for 3 runs in this plate.

At first, the ODS plate was clamped on a titanium back plate. Then, align the die right above of the circle and make sure Z-axis of the machine is coincident with the consolidation axis. When this was done, the position of the die would be recorded as initial die position of the process. In order to reduce the die wear, preheating is carried by torch flame. During preheating period and process period, the temperature was measured by a thermocouple and recorded by LabVIEW program. The locations of thermocouples which attached on the side of process area are shown in Figure 4.16. When the temperature reached 370℃, the torch was turned off immediately and die was moved to initial die position. After die was in position, pressing force was applied with 500N/s increasing rate and die started rotating. There are three experiment conditions implemented: 300RPM, 500RPM and 700RPM. The process load is same at 22,250N. The rotation speed, die position and Z-force (consolidation force) were recorded by the FSW system control computer with 10Hz sampling rate. The rotating torque and power were recorded by a torque transducer mounted on the machine spindle: these data were recorded with at least 40Hz data collection rate.

After experiments, grinding, polishing and etching were applied on horizontally sectioned disc. MA956 and marker material can be differentiated by etched color and flow patterns along the depth of disc were easily observed. By assembling these images along

the depth of disc together, the material flow and deformation of the entire disc were visualized. The commonalities and difference of discs made with various rotational speeds were also analyzed.

4.2.3 Result and discussion

There were three experiment conditions implemented: 300RPM, 500RPM and 700RPM. The same process load at 22,250N and same processing time at 26.4s were applied for comparing deformation of each condition. The peak temperature, maximum torque and total energy input were presented in Table 4.8.

Table 4.8 temperature, maximum torque and energy input in ODS consolidation

rpm	300	500	700
Peak Temperature(℃)	732	776	791
Maximum torque(Nm)	296.7	218.3	173.1
Energy input(kJ)	129.1	149.7	131

The processed part was cut off from the plate and then sectioned horizontally layer by layer. Each layer's top surface was ground, polished and etched for showing the distribution of marker material. As shown in Figure 4.17, silver part is MA956 and darker part is stainless steel marker material. All discs were aligned in the same direction which the initial position of the marker was at 12 o'clock on top view.

133

Figure 4.17 Material deformation of MA956 with stainless steel marker on 1/3r in Friction Stir Process, labeled with layer distance to the bottom of processed disc.

For 300rpm, a considerable amount of material was attached to die after the process. So, only about 3 mm thick remnant disc was left. The deformation below 3mm was not large. For 500rpm and 700 rpm, the deformation depth is about 2.5mm (flash not included). From higher part (which is close to die) to the lower part of processed disc, the deformation is gradually reduced and almost zero at 3.00mm. The mixture area of marker material with MA956 is spread on almost entire surface on top. Along with going deep and getting far from a heat source which is die surface, the mixture area shrinks to center. Then the marker becomes a segment of spiral and finally it is unchanged at the location of the marker's initial shape. The rotational speed range from 300RPM to 700RPM didn't significantly affect the deformation depth when same processing time was used. Comparing the pictures

134

of 500RPM and 700RPM, at 5mm, 4.5mm and 4mm deep, higher rpm has more deformation in these upper layers. But at 3mm deep they are similar, which may indicate a limitation in thickness of the shear layer possibly resulting from similar temperature distributions.

CHAPTER 5

WIRE AND ARC ADDITIVE MANUFACTURING USING FRICTION EXTRUSION WIRES

The friction extruded wire can be applied in several different wire-based techniques like TIG welding or wire and arc additive manufacturing (WAAM). The benefits of using friction extruded wire may lie in its fine equiaxial grain structure, customizable chemical compositions, simple equipment requirement and one step manufacturing procedure. In this study, AA6061 friction extruded wire was used as feedstock of wire and arc additive manufacturing for the first time. Up to 5 meters long aluminum alloy wires were produced by a modified milling machine. They were examined by optical and electron microscope and compared with commercial weld filler wire. Then, up to 16mm high wall samples were successfully built using the friction extruded wires and then cut for metallurgical analysis and mechanical testing. The quality of WAAM part made with friction extruded wire was evaluated. Combine results of hardness test and tensile test with finite element analysis, the thermal cycles of deposition layers are revealed and attributed to properties variation in the vertical direction.

5.1 Wire produce and wall sample build

5.1.1 Friction extrusion wire producing

A C-frame milling machine with a hollow draw bar was employed for the friction extrusion process. The milling machine spindle was used to rotate the die while a hydraulic cylinder mounted on the knee was used to drive the billet chamber charge into the spindle. Hence, this was a force controlled extrusion somewhat analogous to forward extrusion with a rotating die. The rotation rate was set by gear selection and the extrusion pressure was determined by setting the hydraulic pressure on the ram by adjustment of a pressure regulator (the maximum hydraulic power supply pressure was 21 MPa). For this experiment, a 25.0 mm diameter by 38.1 mm long Aluminum Alloy 6061 cylinder was used as the extrusion billet. The hollow drawbar enabled the extrusion of wires up to several meters long. The die hole size defines the diameter of extruded wire. 1mm and 2mm dies were used in this study. The die rotation speeds, extrusion forces and drawing dies used are shown in Table 5.1

Table 5.1 Producing friction extruded wire for WAAM, extrusion parameters and resulting wire lengths.

No.	Diameter of drawing die hole(mm)	Rotational speed (RPM)	Extrusion force (kN)	Wire length (m)
1	1.0	300	106.8	1.36
2	1.0	400	106.8	2.70
3	1.0	400	106.8	2.60
4	2.0	300	106.8	4.30
5	2.0	300	106.8	5.30

Due to the geometry of the experimental device, the extrusion direction is vertical to the ground. Therefore, the wire is twisted by the rotating die and then bent itself by gravity after exiting the draw bar. Part of wires No.3, No.4 and No.5 are shown in Figure 5.1(1), (2) and (3), respectively: some twisting of the wire is evident in the pictures. The surface quality of friction extruded wire and commercial filler wire are examined under scanning electron microscope (SEM), see Figure 5.2. It notes that the damaged surface of ER4043 is obtained by the wire feed roller. It is shown that the surface of the AA6061 filler wire is smooth and uniform. Electron Backscattered Diffraction (EBSD) was performed to inspect the microstructure and grain orientation. As shown in Figure 5.3, metallography of the wires has shown that they are pore-free and that the microstructure consists of fully recrystallized, equiaxed grains with a typical size of 20 μm. The equiaxed grains distribute uniformly in both longitudinal and transverse direction.
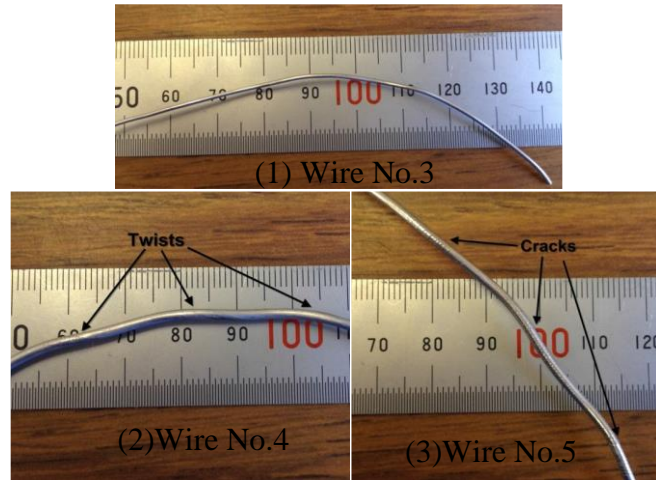
Figure 5.1 Appearance of friction extruded wires: (1) wire No.3 (2) wire No.4 (3) wire No.5
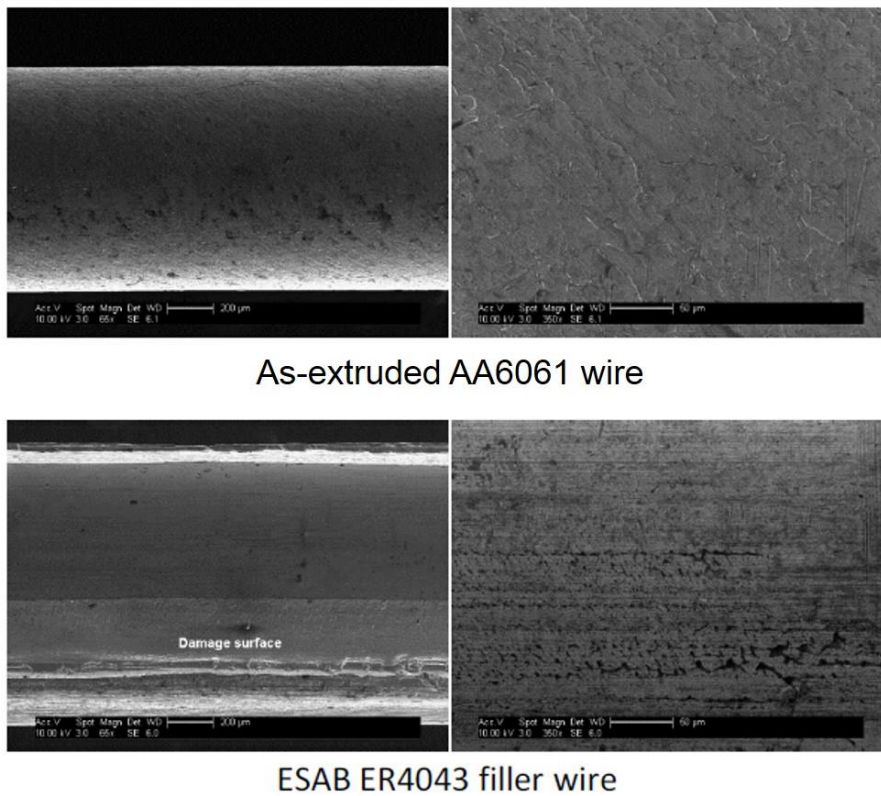
Figure 5.2 Surface condition of 6061 extruded wire and commercial weld filler wire under SEM

Longitudinal section   Transverse section
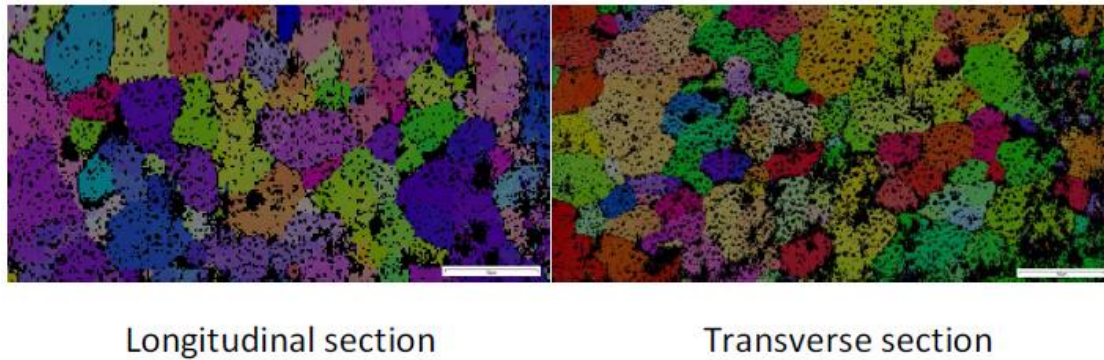
Figure 5.3 EBSD of friction extruded AA6061 wire, longitudinal section (left), transverse section (right)

5.1.2 WAAM wall sample building

The WAAM experiments were performed by Stewart Williams' group at Cranfield University, UK. The experimental system is shown in Figure 5.4, which consists of a Fronius Magicwave 2000 power source, ABB robot, Fronius TIG torch with a diameter of 3.2mm W-2%Ce as electrode, and pure argon as shielding gas (BOC). The actual alternating arc current and voltage waveforms are represented in Figure 5.5, which shows that the positive polarity duration is 70% and that of negative is 30%. AA5083 plate with 6mm thickness was used as the substrate. Because 1mm wire is too thin for manual feeding, the three 1mm diameter wires were wrapped together to form a single wire. The two 2mm wires were fed individually. All wires were cleaned by degreasing with acetone, cleaning with sandpaper (240 grits) and then drying. All builds were produced by manually feeding the wire.
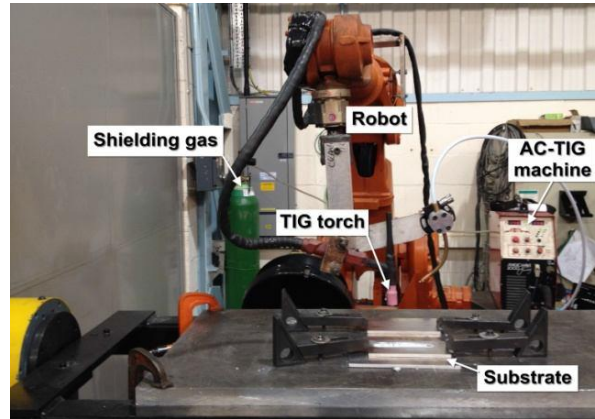
Figure 5.4 AC-TIG experimental system for wire and arc additive manufacturing
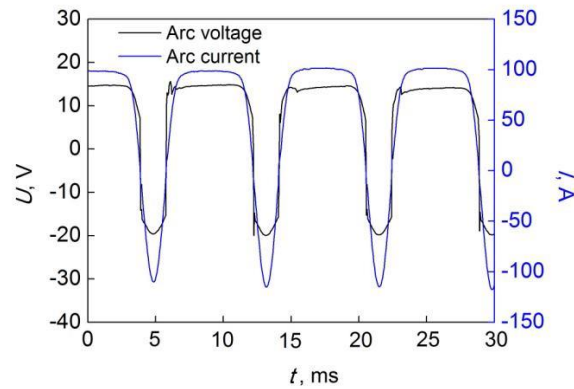
Figure 5.5 Actual arc current and voltage waveforms used in WAAM with friction extruded wire

Builds were made with constant argon shielding gas flow rate of 15L/min, arc length of approximately 5mm, an electrode tip angle of 60 °, and travel speed of 0.21m/min. Each layer was approximately 100mm long and 1 mm high. Arc current is varied with the increase of deposition layer number in accord with previous experience. AA5083 (Mg 4.5%, Cr 0.2%, Mg 0.7%, Si≤0.4%, Ti≤0.15%, Zn≤0.25%, Cu≤0.1%, Fe≤0.4% and Al balance) was used as substrate to support wall samples.

Multilayer deposition samples successfully made with the three AA6061 friction extruded wires using the AC-TIG process are shown in Figure 5.6. The height of walls made with No.3, No.4 and No.5 are 3mm, 10mm and 16mm respectively.
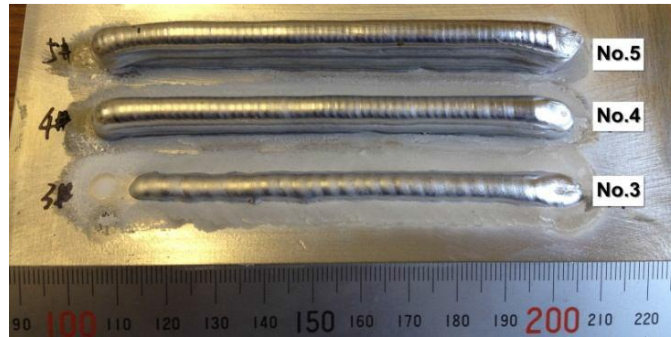
Figure 5.6 Profile of multilayer deposition walls made with friction extruded wires

5.2 Post-analysis

5.2.1 Surface inspection and metallurgical analysis

Due to sub-optimal wire cleaning processes and issues related to waviness of the wires, inclusions and geometric inconsistencies are intermittently observed on the build surface. The inclusions in a previous layer will influence the melting stability and quality of subsequently deposited layers and may result in porosity and other defects in the multilayer deposition. Inclusions and depressions which are indicated in Figure 5.7 are generated mainly due to imperfections in the wire. Twisting of the wire also results in somewhat inconsistent wire feed rate.
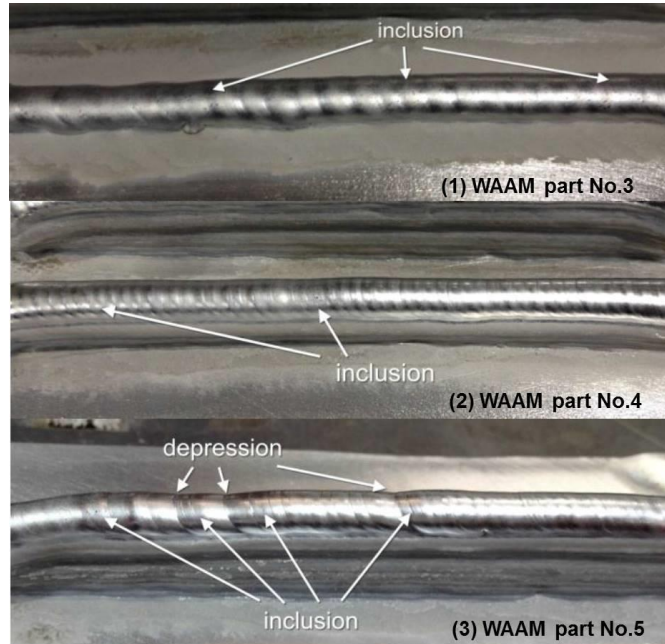
Figure 5.7 Appearance of WAAM parts made with (1) wire No.3 (2) wire No.4 (3) wire No.5

The WAAM parts were transversely cut, as shown in Figure 5.8. The cross-section of the left part was ground and polished.

Figure 5.8 Cut line of WAAM parts

Void content was assessed by optical microscope on as polished specimens. The microstructure was elucidated while Keller's etchant (190ml water, 2ml HF, 3ml HCl, and 5ml HNO$_3$) was used. Grain size was measured along the vertical direction of the build by using the mean linear intercept (MLI) method [74].

As shown in Figure 5.9, there are voids observed in the cross-sections of the WAAM parts made with the friction extruded wire. For all three samples, the upper region contains more voids than bottom lower region: why this is so is not obvious but may be related to the arc model type and changes in arc current with build height[63]. The void number, total void area, average void size and void area faction at different heights were calculated by ImageJ software and shown in Figure 5.10. The lower region contains a higher number of voids but the total area and the void fraction are relatively small. Middle and top region contain more, larger, voids: the largest void is over 50 μm across.
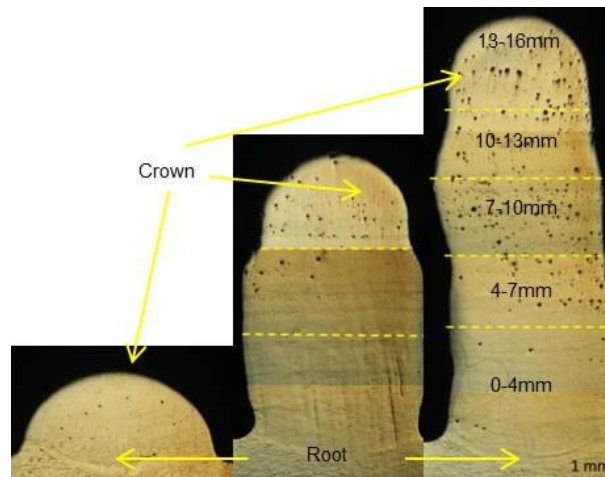
Figure 5.9 Transverse cross-sections of WAAM parts

144
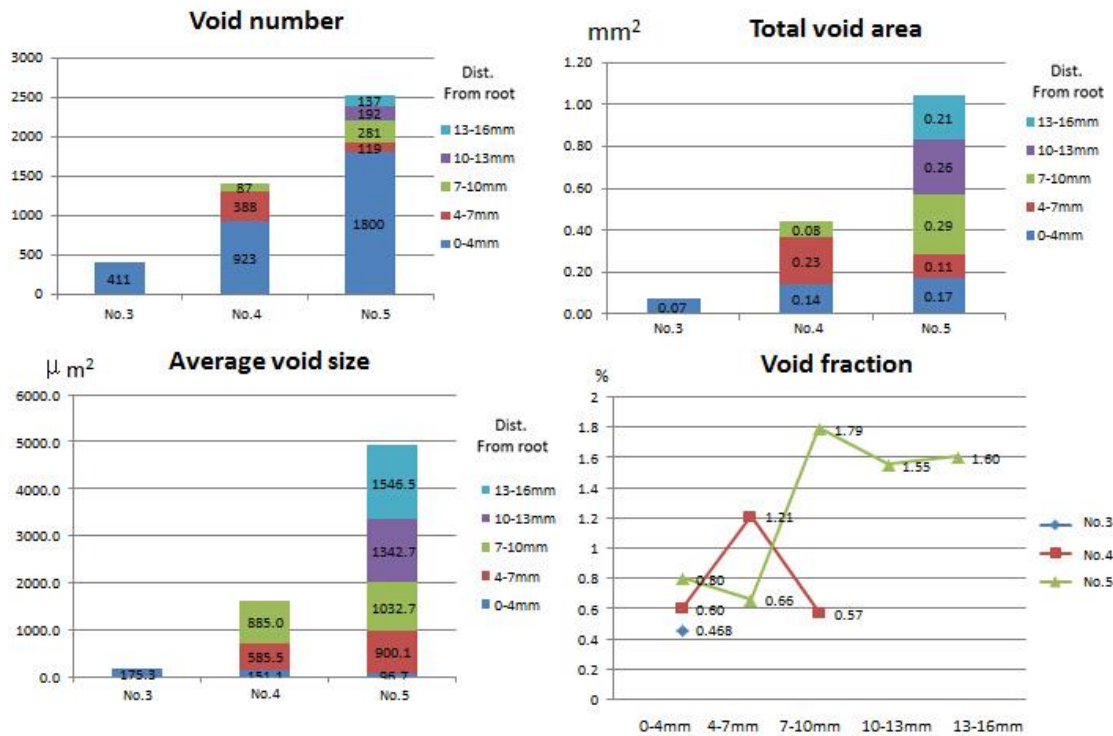
Figure 5.10 Void number, area, average size and void fraction on the transverse cross-sections of WAAM parts

As shown in Figure 5.11, the microstructure of the builds is typical of arc weld deposited material. Grains were nearly equiaxed but slightly elongated in the vertical direction. On the boundary between the AA6061 walls and the AA5083 substrate, this vertical elongation is most obvious. The grain size of the highest build at the crown, middle and root is presented in Figure 5.11. The grains are largest at the root and smallest near the crown.
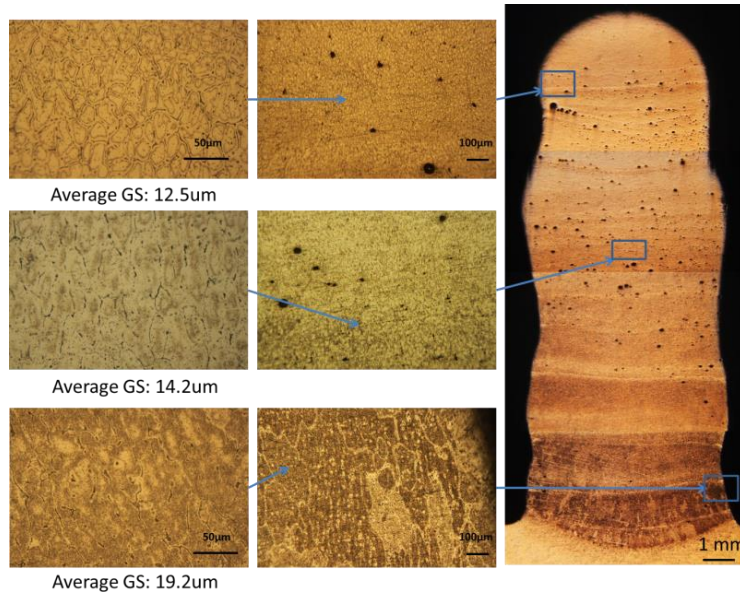
Figure 5.11 Microstructure and grain size distribution on the cross-section of WAAM sample No.5

5.2.2 Hardness Test

The Vickers hardness of No.4 and No.5 WAAM parts have been measured along the central vertical line on the transverse cross-section. Both as-made and after a standard 6061-T6 heat-treatment were tested to reveal the effort of heat-treatment on these samples. The hardness data are shown in Figure 5.12. Both of them give the same trend of hardness along the vertical direction. From crown to root, the value increases first and reaches a peak at 3mm from the top. Below three mm from the crown the hardness decreases to approximately 60-70 HV and remains stable. Below the boundary of the WAAM part and the 5083 substrate, the hardness of the substrate is higher than that of the wall. Comparing the result before and after heat treatment, the T6 heat treatment generally provides a minor

improvement on hardness but most regions remain far from the hardness of the standard

6061-T6 value 107HV.
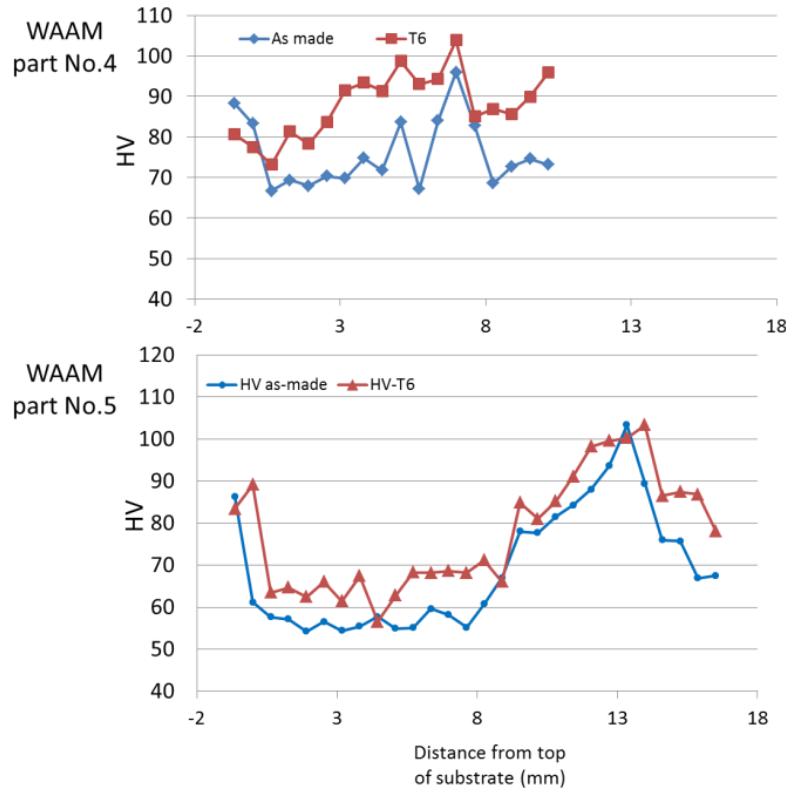
Figure 5.12 Vickers hardness on vertical central line of transverse cross-sections of part No.4 and No.5

5.2.3 Tension Test

For both as-made and standard AA6061-T6 (18 hours at 160°C) conditions, longitudinal tensile specimens w ere machined from WAAM wall sample No.5. They were machined to the shape suggested by ASTM standard [81] and then horizontally sliced into 1mm thick tensile bars, see Figure 5.13 and Figure 5.14. At last, 400 grits sand paper was applied to smooth their surfaces. In order to perform digital image correlation (DIC) during

tension test, one side of the tensile bar was painted with white background and then black

dots pattern, shown in Figure 5.15.
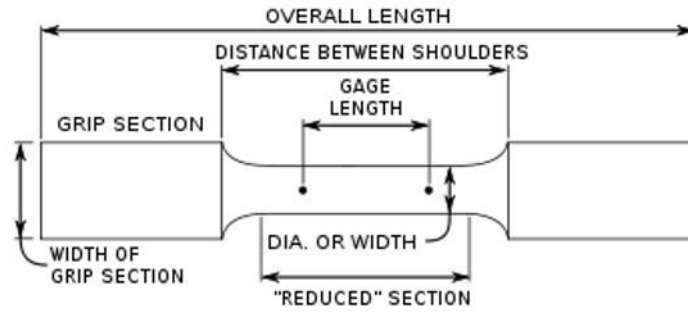
As ASTM Standard E 8M-04	Sub-size specimen (mm)
Gauge length	12±0.05
Width	3.0±0.05
Thickness	1
Overall length	24
Length of reduced section	16
Length of grip sections	8
Width of grip	4--6

Figure 5.13 Geometry of sub-scale tensile bar
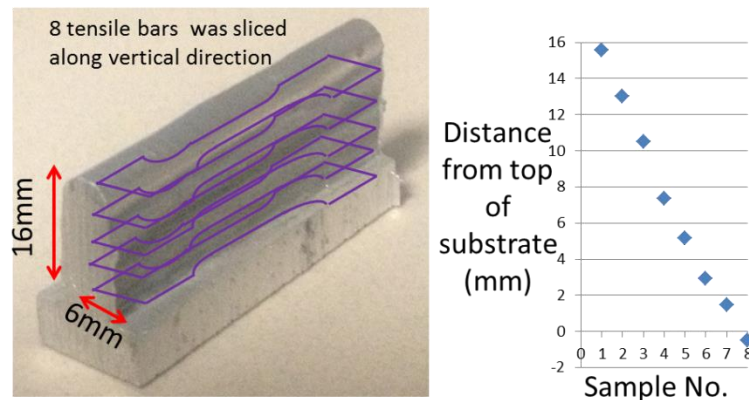
Figure 5.14 longitudinal tensile bars and sample positions

148
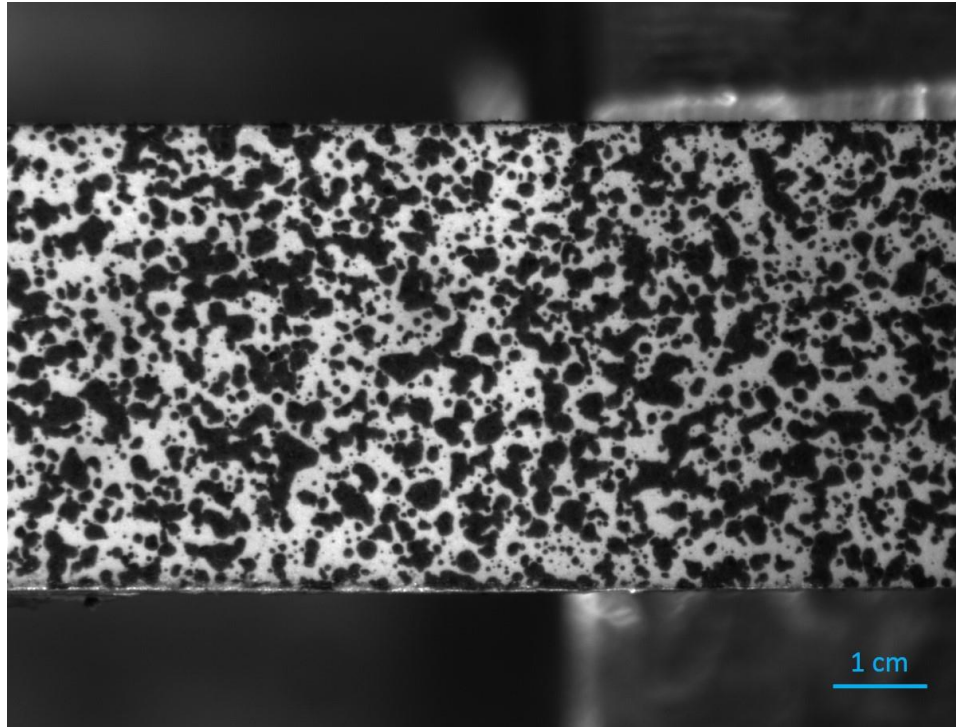
Figure 5.15 Painted tensile bar, gage area

A sub-scale material tester (Figure 5.16) and digital image correlation (Figure 5.17) were used to obtain stress-strain curves of all tensile bars. These tension tests were performed with 0.1mm/s displacement rate. Force was measured by a load cell instrumented on the sub-scale tester and recorded by computer via Labview software. Displacement field was captured and calculated by digital image correlation system. A CCD camera was employed to take pictures with 2Hz sampling rate during tension test. The focal length of the camera is 55mm, aperture number N=16, the circle of confusion c=3.6e-3, subject distance is 120mm, depth of field is 0.55mm which is sufficient for this test. After the experiment, pictures were analyzed by Vic2D DIC software to extract strain field history on the tensile bar. Thus, the local strain and elongation can be obtained.

149
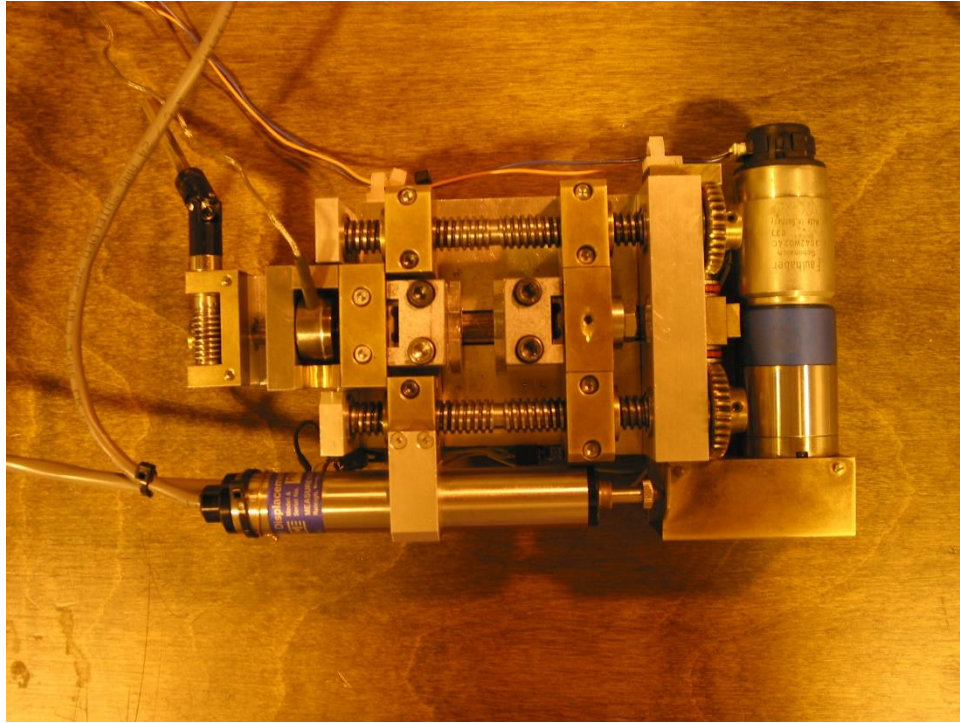
Figure 5.16 sub-scale tension tester
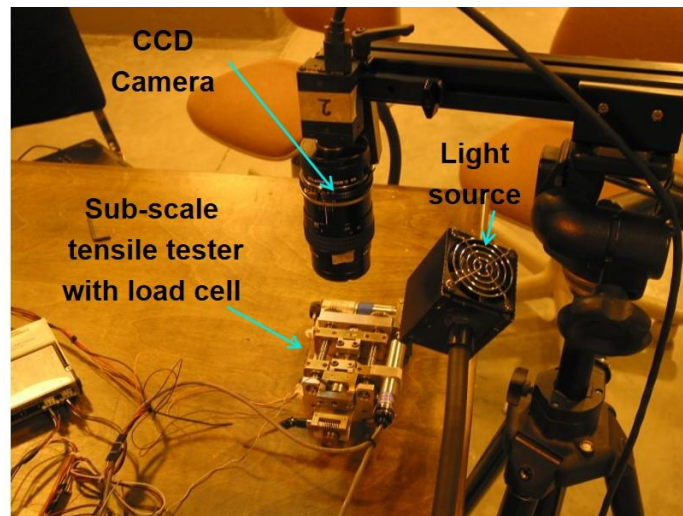
Figure 5.17 Camera and lighting setup for digital image correlation

The elongation of tensile bars at different height are presented with porosity condition in Figure 5.18. The trends of elongation in both as-made and aged conditions are basically matching with voids fraction distribution.
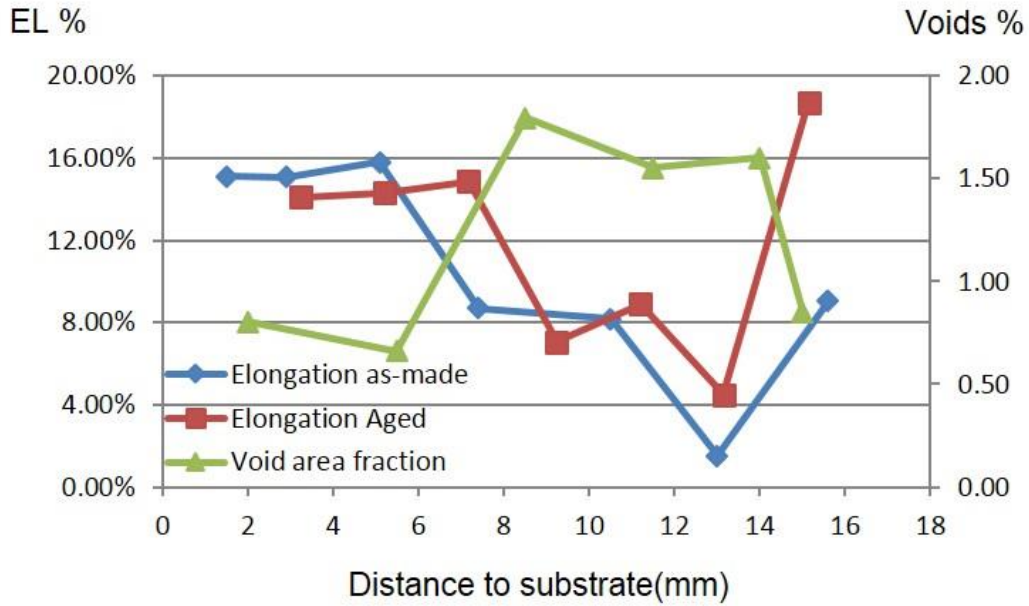
Figure 5.18 Elongation and voids area fraction vs. height on cross-section

The ultimate tensile strength is presented together with hardness results in Figure

5.19. The strongest part of the wall has UTS over 340MPa at 3mm below the crown: this

is higher than the UTS of standard 6061-T6, 310MPa. Comparing UTS values with the

hardness result indicates that they have similar trends with regard to the position in the

build.
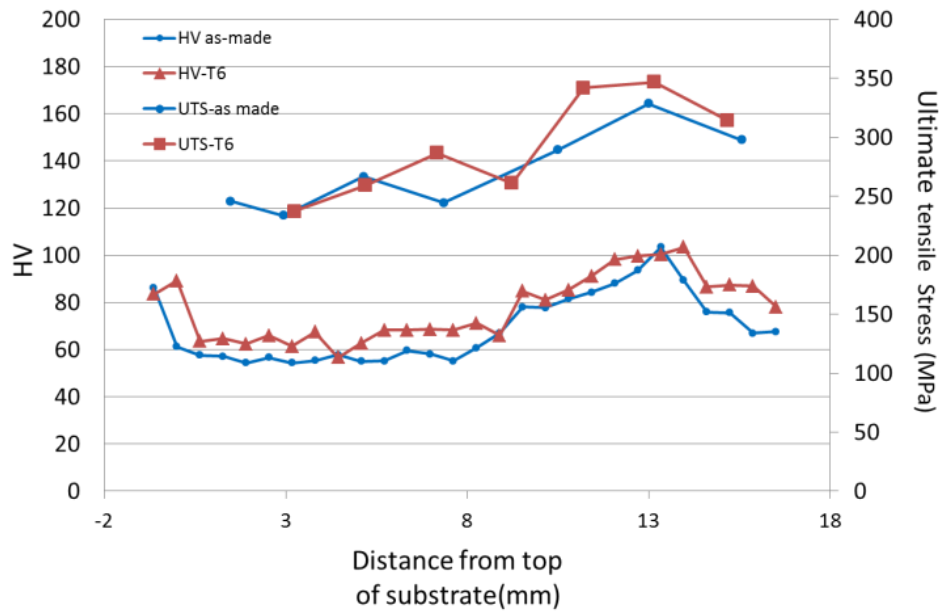
Figure 5.19 Ultimate tensile stress and Vickers Hardness variation on different height position of WAAM sample No.5

5.3 Transient thermal modeling of wire and arc additive manufacturing

Based on above mechanical tests, it shows that the distribution of hardness and ultimate tensile strength are following the same trend in the vertical direction where depositions were layer by layer structured. This inhomogeneous could be related to the different thermal history between deposited layers. At the root of the wall, substrate acted like heat sink which gave it fast cooling rate and consequent lower temperature. The deposition layers in the middle were affected heat-treatment when subsequent layers were produced above them. The last few layers at the top will not receive much later influence or even no influence at all for the last layer. Since no temperature measurement could be

152

done in the center of a depositing droplet, finite element method was introduced to provide an estimation of the temperature field of wire and arc additive manufacturing process.

5.3.1 Heat transfer model

Due to the interaction between thermal field, temperature dependent material properties and microstructure, the thermo-mechanical analysis of welding process is complex. In this study, the most interesting issues are the thermal field of WAAM process and temperature history of each deposition layer. Microstructure evolution and residual stress are not considered to reduce the computational cost of the analysis. Therefore, pure heat transfer model is used for achieving our target. Comsol 4.4 software is adopted to establish finite element model and perform thermal analysis.

The geometry of substrate and deposited wall is shown in Figure 5.20. X axis is defined as length direction. The positive x direction is consistent with the moving direction of the welding torch. Y axis is defined as width direction. Z axis is height direction. Deposition layers were built along with positive Z direction. Since the deformation of the droplet is neglected, the y-z cross-section of deposition layer was modeled as a rectangular shape. The size of substrate and deposition layer which were obtained in the real sample are shown in Table 5.2. Several models with different layer numbers were built individually to simulate a single deposit path. In each model, a moving heat source was only generated in top layer which pre-existed in the initial step.
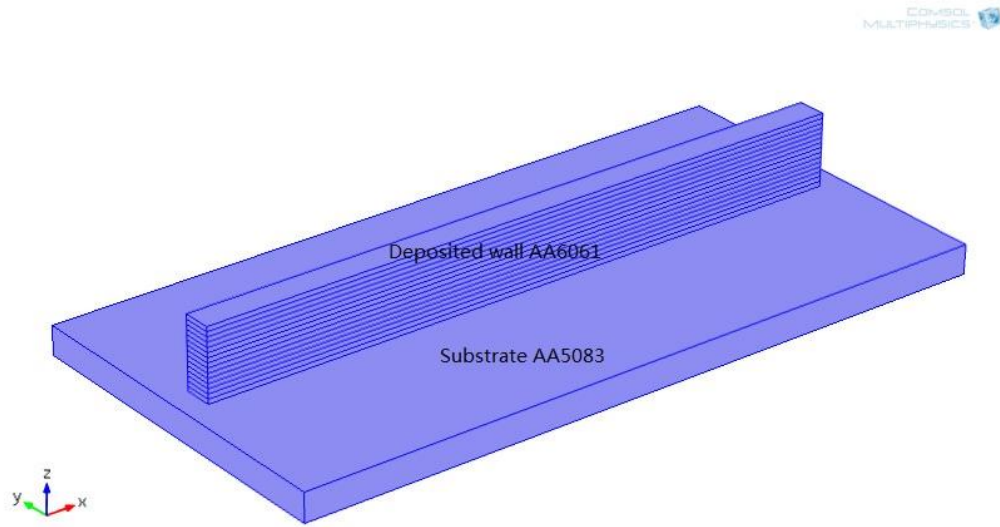
Figure 5.20 Geometry of substrate and deposited wall in simulation model of WAAM process

Table 5.2 Size of substrate and a single deposition layer

	X(mm)	Y(mm)	Z(mm)
Substrate	150	75	6
Deposition layer	140	6	1
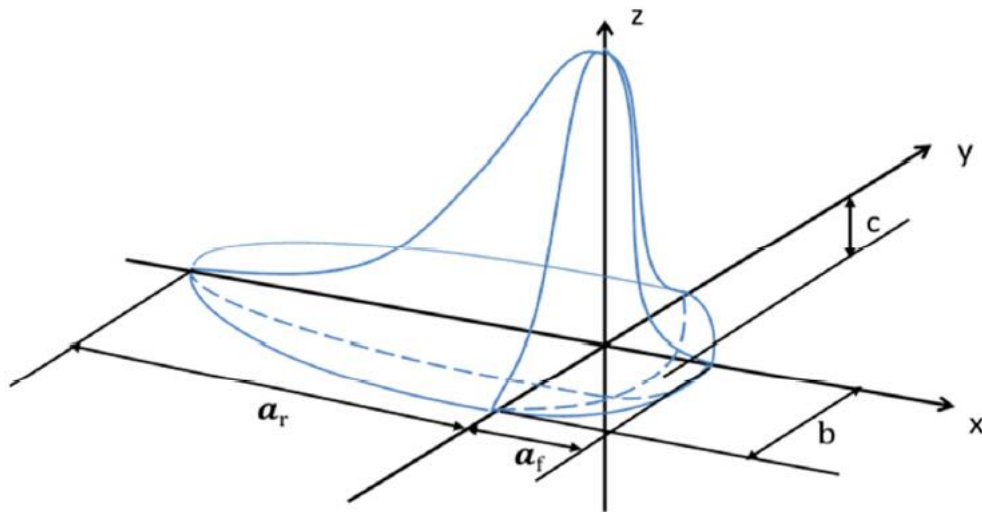
Figure 5.21 Goldak's double ellipsoid heat source model[65]

The heat generation function used in this transient heat transfer modeling is Goldak's double ellipsoid heat source model, see Figure 5.21. The power density distributions are separately defined in the region in front of the arc center, Eq (5.1):

$$q_f = \frac{6\sqrt{3}Qf_f}{\pi\sqrt{\pi}a_f bc} e^{\left[-3\left(\frac{x^2}{a_f^2}+\frac{y^2}{b^2}+\frac{z^2}{c^2}\right)\right]}$$

Eq (5.1)

and the region behind the arc center, Eq (5.2)

$$q_r = \frac{6\sqrt{3}Qf_r}{\pi\sqrt{\pi}a_r bc} e^{\left[-3\left(\frac{x^2}{a_r^2}+\frac{y^2}{b^2}+\frac{z^2}{c^2}\right)\right]}$$

Eq (5.2)

Where Q is the total energy input considering efficiency factor, a_f and a_r are the length of the frontal ellipsoid and the rear ellipsoid, respectively, b is the half width of heat source, c is the depth of heat source, f_f and f_r are the factors of distributing the power to the front and rear of the heat source, they have the relation that $f_f + f_r = 2$. In this model, a moving heat source was established to simulate the movement of the welding torch. The arc center is defined in the center of the y-z cross-section of the top deposition layer and moving towards positive x-direction with a constant speed 8.33mm/s.

Based on actual arc current and voltage waveforms shown in Figure 5.5, the energy input is calculated by the Average Instantaneous Power (AIP) method:

$$Q[W] = \eta \cdot \sum_{i=1}^{n} \frac{V_i \cdot I_i}{n}$$

Eq (5.3)

Where Q it the total energy input, η is the factor of efficiency, V_i and I_i are the instantaneous voltage and instantaneous current, respectively. The parameter a, b and c are determined by the weld pool size and shape which estimated from metallographic

155

measurement on cross-section and surface ripple marking of the weld. They are listed together with calculated power input in Table 5.3.

Table 5.3 Heat source parameter

af (mm)	ar (mm)	b (mm)	c (mm)	Q(W)	ff	fr	η
2	6	3.5	1.5	965	0.6	1.4	0.7

Conduction, convection and surface radiation are considered in thermal boundary conditions. The initial temperature was set to 20℃. The convection coefficient is set to 6 W/m^2·K. The radiation coefficient was set to 0.2 W/m^2·K. They were assumed independent of temperature. The heat loss through the back side of the substrate was modeled with an equivalent convection coefficient 900 W/m^2·K. The other heat loss like through clamping tool and filler wire was minor and so neglected.

The key temperature dependent thermal properties of material include thermal conductivity and specific heat. An artificial high thermal conductivity 1000 W/m·K is set at temperature above liquidus temperature of AA6061 to capture the convective heat transfer in the molten weld pool. The latent heat during phase change of AA6061 is 360 KJ/kg. The heat capacity of AA6061 from solidus temperature 582 ℃ to liquidus temperature 652℃ is uniformly modified for compensating latent heat. The values of modified thermal conductivity and specific heat of AA6061 and AA5083 are listed in Table 5.4 and Table 5.5, respectively. Linear interpolation and constant extrapolation were employed. Constant material density at room temperature was used in the simulation, 2700 kg/m^3 for AA6061, 2640 kg/m^3 for AA5083.

Table 5.4 Thermal conductivity and specific heat of AA6061

Temperature ℃	Thermal conductivity k(W/m·K)	Specific Heat Cp [J/kg·K]
-17.78	155.94	916.54
37.78	164.79	944.09
93.33	173.65	971.64
148.89	182.50	999.19
204.44	191.36	1026.74
260.00	200.21	1054.29
315.56	209.07	1081.84
371.11	217.93	1109.39
426.67	226.78	1136.94
571.11	249.81	1208.57
582.00		1213.94
583.00		1223.70
652.00	1000.00	1608.66
652.01		1248.66

Table 5.5 Thermal conductivity and specific heat of AA5083

Temperature ℃	Thermal conductivity k(W/m·K)	Specific Heat Cp [J/kg·K]
20	117	900
80	122.7	984.2
180	131.6	1039.6
280	142.3	1081.2
380	152.5	1136.6
480	159.5	1178.2
580	177.2	1261.4

There were two major types of elements used in meshing, Figure 5.22. Brick elements with 8 nodes are more accurate with increased computing source and time. It was employed to mesh deposition walls which are the most significant part. Tetrahedral elements are more effective in saving computing time so they were adopted to mesh the substrate. All elements were pre-existed in the initial step. For a 15 layers model, entire

geometry was consists of 36656 elements. Temperature probes were placed at the center

of all deposition layers to record temperature change during the process.
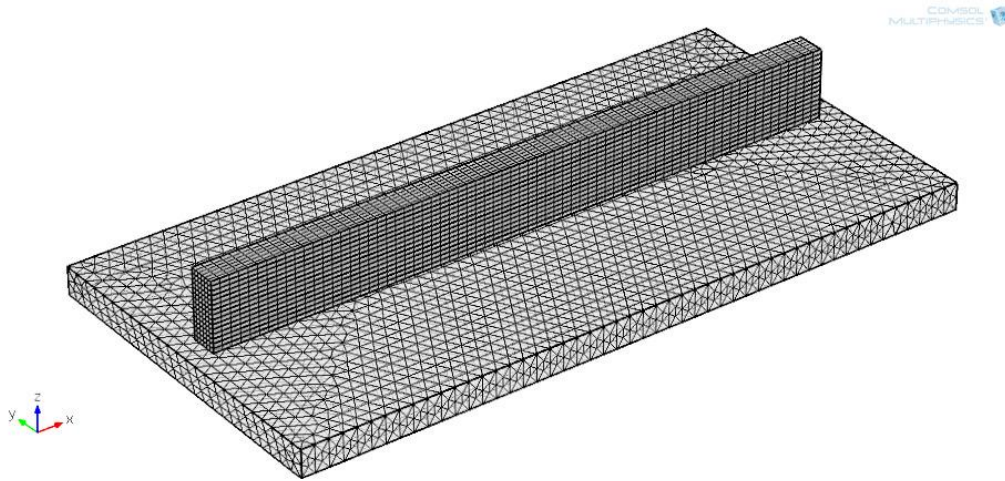
Figure 5.22 Meshing of AA6061 wall and AA5083 substrate

5.3.2 Temperature field and temperature history for a single layer
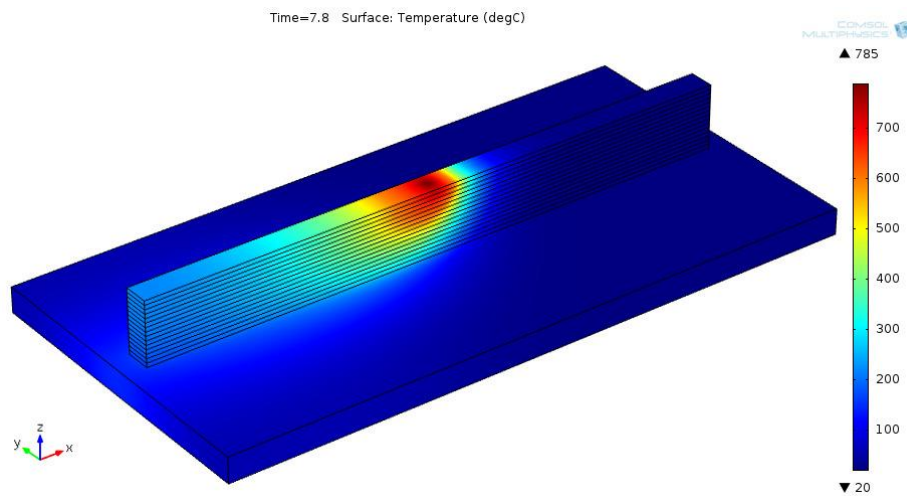
Figure 5.23 Simulated temperature field of AA6061 WAAM process at 7.8s (with history peak temperature)

Figure 5.23 shows the simulated temperature field while depositing the 15th layer

of WAAM process using AA6061 wires, at 7.8s when history peak temperature is observed.

158

Because no temperature measurements have been done during the process, strict validation of temperature result is not available. Qualitatively comparisons are discussed to give a general idea of the validity of this simulation. The shape of temperature profile is a tail-dragged ellipse which is reasonable and consistent with results found in mild steel and Ti WAAM[52]. The temperature history of center points of each layer is present in Figure 5.24, layers closer to heat source naturally have a higher temperature. From observation during the process, we learn that the depth of fusion zone is about 4 to 5 mm. Results in Figure 5.24 show that only top 5 layers' peak temperature exceed solidus temperature 582℃, which corresponds with experimental observation.
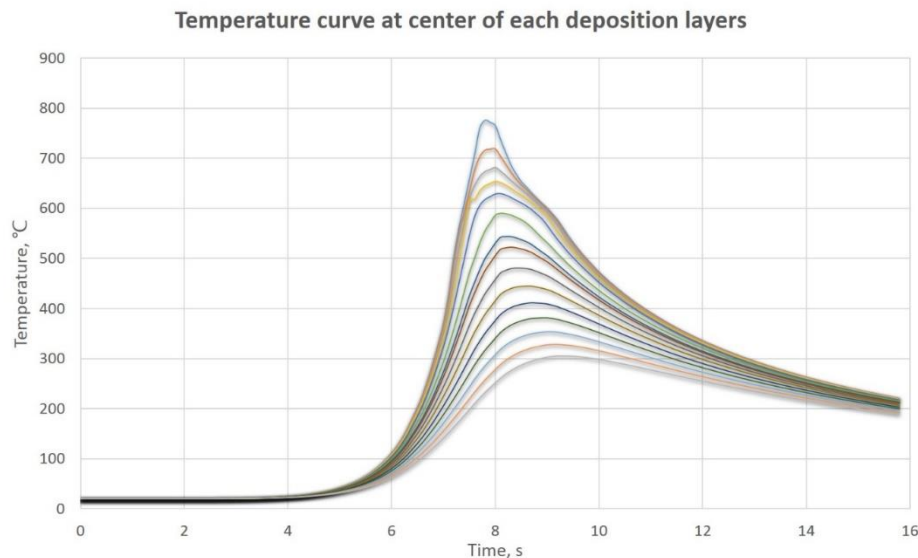
Figure 5.24 Temperature curve at center of each deposition layer during deposition of the final layer.

To conduct mesh density sensitive study, a model with double finer element number meshing on vertical direction of wall part was performed. Only minor difference was found

159

between two meshing. The results of history peak temperature at each layer from these two

model were presented in Figure 5.25. It indicates the adopted meshing density is sufficient

enough for this model.
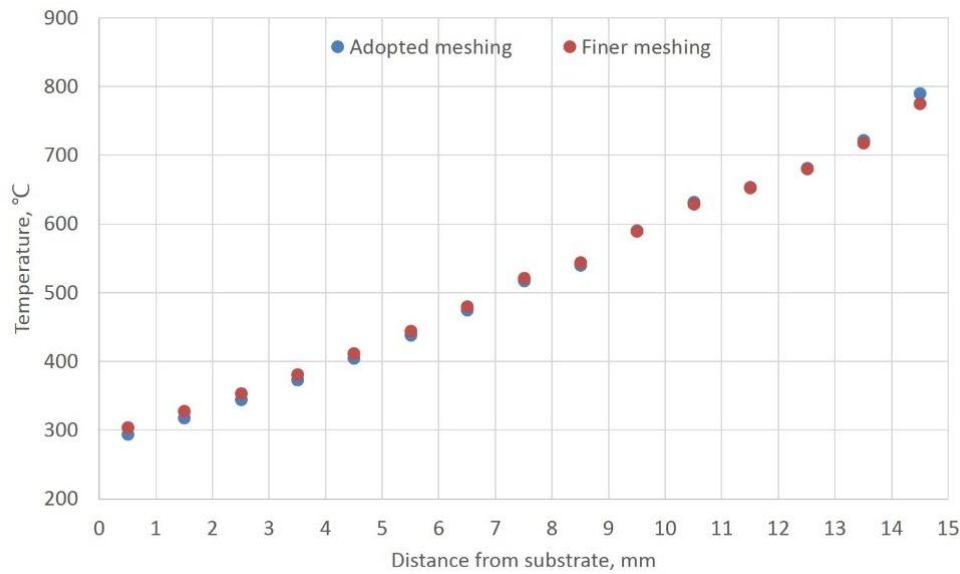
Figure 5.25 History Peak temperature of each layer in adopted meshing and finer meshing
models

The temperature history of a single deposited layer during multi-pass depositions

was obtained by combine results from several single simulations with increased wall height.

For instance, temperature curve of the 11th layer was shown in Figure 5.26 from depositing

11th to 15th layer. When the 11th layer was deposited, the temperature in molten weld pool

reached almost 800℃. After that, when the following deposition layers were fabricated

with further and further distance, the 11the layer received a sort of "heat-treatment" with

decreased temperature. This heat treatment affects the final mechanical and metallurgical

properties. The material located in different height position received heat treatment at different times and temperatures. For this reason, they turn out to have variant tensile strength and hardness in the vertical direction.
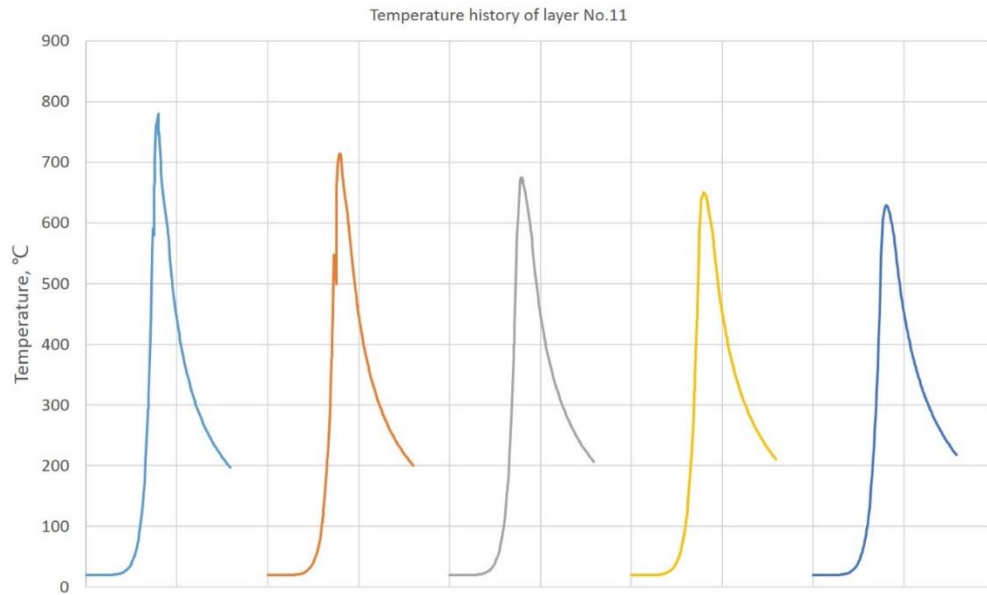
Figure 5.26 Temperature history of layer No.11 during deposition layer No.11 to No.15 (from left to right, respectively)

5.4 Summary and discussions

A modified milling machine with a hydraulically driven ram was employed to produce friction extruded wire for additive manufacturing. Process variables like die rotational speed and extrusion hole size were adjusted to achieve a wire with no break and longer length, respectively. SEM images showed friction extrusion wire have smoother surface compared with commercial welding filler wire. Texture analysis on both transverse cross-section and longitudinal cross-section of friction extrusion wire revealed an equiaxial

grain structure which is a favorable feature in AM which conventional filler wire do not possess.

Using friction extruded wire as filler material, wall structure samples were successfully made via wire and arc additive manufacturing. TIG torch combined with robotic automation system was employed in WAAM to realize precise motion control of welding torch. Metallurgical inspection showed nearly intact microstructure with equiaxial grain shape on aluminum WAAM sample, but small voids were also found and related with elongation reduction in tensile tests. Results of tensile tests and hardness tests indicated that good mechanical properties were obtained in some region. Post heat treatment did not significantly improve the tensile strength and hardness.

Thermal finite element model of WAAM using aluminum wire was established to simulate energy input, heat transfer and temperature field during the process. Goldak's double ellipsoid heat source model was adopted to determine the shape, the size and the density of energy input. Temperature dependent material properties included modified thermal conductivities with considering phase change were derived. The region of simulated fusion zone corresponded with experimental observation, thus, a good simulation was validated. Comparing the different thermal cycle history of each deposition layer from simulation, the difference of mechanical properties along the vertical direction of WAAM sample can be explained: due to distance gradient, material on different height received different heat treatment while the last layer was deposited. For deposition layer

162

about 3 or 4 mm to the last (top) path, the temperature of it during producing the last path was around 529℃ which is the solution heat treat temperature. Therefore, it acquired strongest tensile strength and hardness. For the layers about 8mm from the top, the temperature during the last path was around like 400℃ which is a temper heat treat temperature, so it lost strength and hardness.

To conclude, the feasibility of using friction extrusion wire as feedstock in additive manufacturing was proven. Friction extrusion wire has a great potential ability in AM due to its customizable chemical compositions, simple producing equipment/procedure and fine equiaxial grain structure. A specialized machine with horizontal extrusion direction, longer chamber and accurate thermal management can help produce friction extrusion wire with longer length and stable mechanical quality. Structure with considerable good mechanical properties can be manufactured when favorable thermal control is applied during WAAM process. Finite element model can predict the thermal field of WAAM process and help obtain parts with better mechanical properties. To further study about residual stress or microstructure evolution, a mechanical thermal model will be useful to provide a better simulation of WAAM process.

CHAPTER 6

CONCLUSIONS AND FUTURE WORK

To understand the mechanism of friction extrusion and consolidation, key data was recorded and experiments were performed with different die tip patterns, die rotational speeds, extrusion forces, and precursor sizes. Wire and disc products were sectioned then metallurgically examined to reveal microstructure, texture and material flow. The result of temperature measurement and marker material redistribution validated finite element model of friction extrusion process. Wire and arc additive manufacturing samples made with friction extruded wire were tested and compared with commercial base metal. Heat transfer model was built to predict temperature field of WAAM process.

By comprehensive analysis all the results from experiments and numerical simulations, several conclusions and trends are summarized and highlighted below:

About friction extrusion

Material flows in spiral line in friction extrusion process. The material located between center and 1/3 radius gradually move into central extrusion hole as a spiral line. A dead zone exist in friction extrusion as well as in conventional extrusion. Die tip

pattern, experimental parameter can change the shape of flow pattern. Scrolled die face brings about more rotations of material than flat die face. Higher rotational speed and lower extrusion force also lead to more revolutions in material flow pattern.

(1) The process temperature of friction extrusion, as performed in this study, is increasing due to uncontrolled heating of the extrusion apparatus resulting from continuous heat input via dissipation of plastic work and insufficient heat transfer away from the apparatus to maintain a steady state. Due to an increase in temperature, the in-plane deformation and, hence, strain, decreases with increasing extrusion length: that is, the extrusion becomes more like a "conventional" extrusion and the major working direction moves toward the extrusion direction and away from the die rotation direction. The evolution of texture of wire and simulated material flow pattern are also in agreement with above conclusion.

(2) Figure 3.36 indicates that higher rotational speed, which corresponds to higher power input accelerates the evolution of the process toward "conventional" extrusion and higher extrusion rate; higher extrusion force also brings about higher extrusion rate.

(3) No obvious grain elongation in the longitudinal direction. Equiaxial recrystallized grain structure exists in both transverse direction and longitudinal direction, which implies that aluminum alloy was recrystallized after being extruded through the hole.

(4) Post-extrusion drawing can improve the applicability of extruded wires in the following ways: (a) obtain desired diameter, (b) improve surface finish, (c) extending the total length. Annealing and re-annealing can alleviate work-hardening caused by drawing to prevent wire breaking in the posterior drawing.

About friction consolidation:

(1) Aluminum alloy machining chips can be friction consolidated into a bulk disc with almost same density of parent material.

(2) Friction consolidation process has two distinct periods: compaction and consolidation. In compaction period, material is largely compacted but not well integrated. The gap between material particles diminishes but welding of the chips to each other does not occur. In consolidation period, material density increases slightly. With a combination of high temperature and severe plastic deformation, a bowl-shaped, fully consolidated region with recrystallized equiaxed grain structure is formed at the top of billet charge. With increasing processing time, the bowl-shaped region gradually expands from top to lower part of the billet chamber but can't reach bottom corner even after long processing time.

(3) Three kinds of chips with different length are prepared to study the effect of precursor dimensions on the process. All of them are successfully consolidated. No obvious difference was found in the appearance of consolidated discs. The densities of discs are quite similar and very close to standard AA6061. The energy inputs are

166

also similar to each other. In sum, the length of chips did not fundamentally affect process if the weight of material and processing time is fixed.

(4) The fraction of consolidation has been proposed to quantify the mass percentage of fully consolidated material. With current experimental setup, maximum 73% has been reached in a fully processed friction consolidation. The effort of die rotational speed, compressive force and processing time on fraction of consolidation have been analyzed via design of experiments. All three parameters have a positive influence on fraction of consolidation. Over certain processing time, the effect of processing time will not give better consolidation.

About wire and arc additive manufacturing using friction extruded Al alloy wire:

(1) The feasibility of using friction extrusion wire as feedstock in additive manufacturing was proven. Friction extruded wires have a great potential ability in AM due to its customizable chemical compositions, simple producing equipment/procedure and fine equiaxial grain structure.

(2) Structure with good mechanical properties can be manufactured when favorable thermal control is applied during WAAM process. Finite element model can predict the thermal field of WAAM process and help obtain parts with better mechanical properties.

Based on above analysis and current understanding of friction extrusion and consolidation, future work is proposed as following:

(1) A specialized machine with horizontal extrusion direction and longer chamber can help produce friction extrusion wire with longer length and stable mechanical quality. This machine must be designed and built.

(2) Apply an effective thermal management system on friction extrusion process with capabilities like pre-heat chamber and die, fast heat extraction, etc. Therefore, better control on temperature, extrusion rate and even microstructure and texture of wire can be realized.

(3) Establish more precise theoretical and simulation model to better describe heat generation, predict heat transfer, capture material flow, derive strain rate and determine the region of dead zone.

(4) Use a mechanical thermal model to simulation the residual stress and microstructure evolution of WAAM process, and provide effective data for thermal management that ensure WAAM parts have sound mechanical properties in extended region.

BIBLIOGRAPHY

[1] W. M. Thomas, E. D. Nicholas, J. C. Needham, M. G. Murch, P. Templesmith, and C. J. Dawes, "GB Patent application no. 9125978.8," *Int. Pat. Appl. No PCTGB9202203*, 1991.

[2] "Wire," *Wikipedia, the free encyclopedia*. 16-Mar-2015.

[3] "Recycling," *Wikipedia, the free encyclopedia*. 07-Apr-2015.

[4] "Aluminium recycling," *Wikipedia, the free encyclopedia*. 31-Mar-2015.

[5] "Made In Space | Additive Manufacturing in Space." [Online]. Available: http://www.madeinspace.us/. [Accessed: 08-Apr-2015].

[6] R. S. Mishra, M. W. Mahoney, S. X. McFadden, N. A. Mara, and A. K. Mukherjee, "High strain rate superplasticity in a friction stir processed 7075 Al alloy," *Scr. Mater.*, vol. 42, no. 2, pp. 163–168, 1999.

[7] S. Mohan and R. S. Mishra, "Friction stir microforming of superplastic alloys," *Microsyst. Technol.*, vol. 11, no. 4–5, pp. 226–229, 2005.

[8] R. S. Mishra and M. W. Mahoney, "Friction stir processing: a new grain refinement technique to achieve high strain rate superplasticity in commercial alloys," in *Materials Science Forum*, 2001, vol. 357, pp. 507–514.

[9] R. S. Mishra, Z. Y. Ma, and I. Charit, "Friction stir processing: a novel technique for fabrication of surface composite," *Mater. Sci. Eng. A*, vol. 341, no. 1, pp. 307–310, 2003.

[10] I. Charit and R. S. Mishra, "High strain rate superplasticity in a commercial 2024 Al alloy via friction stir processing," *Mater. Sci. Eng. A*, vol. 359, no. 1, pp. 290–296, 2003.

[11] Z. Y. Ma, R. S. Mishra, and M. W. Mahoney, "Superplasticity in cast A356 induced via friction stir processing," *Scr. Mater.*, vol. 50, no. 7, pp. 931–935, 2004.

[12] S. Jana, R. S. Mishra, H. N. Chou, and D. R. Herling, "Friction stir microstructural modification of investment cast F357," in *Proceedings of the 2007 Minerals, Metals, and Materials Society Annual Meeting*, 2007.

[13] N. Balasubramanian, R. S. Mishra, and K. Krishnamurthy, "Process forces during friction stir channeling in an aluminum alloy," *J. Mater. Process. Technol.*, vol. 211, no. 2, pp. 305–311, 2011.

[14] J. A. S. Green and others, *New Materials for Next Generation Commercial Transports*. Washington DC: National Academies Press, 1996.

[15] P. L. Threadgill, "Terminology in friction stir welding," *Sci. Technol. Weld. Join.*, vol. 12, no. 4, pp. 357–360, 2007.

[16] P. L. Threadgill, A. J. Leonard, H. R. Shercliff, and P. J. Withers, "Friction stir welding of aluminum alloys," *Int. Mater. Rev.*, vol. 54, no. 2, pp. 49–93, 2009.

[17] R. Rai, A. De, H. Bhadeshia, and T. DebRoy, "Review: friction stir welding tools," *Sci. Technol. Weld. Join.*, vol. 16, no. 4, pp. 325–342, 2011.

[18] M. A. Sutton, B. Yang, A. P. Reynolds, and J. Yan, "Banded microstructure in 2024-T351 and 2524-T351 aluminum friction stir welds: Part II. Mechanical characterization," *Mater. Sci. Eng. A*, vol. 364, no. 1, pp. 66–74, 2004.

[19] B. Yang, J. Yan, M. A. Sutton, and A. P. Reynolds, "Banded microstructure in AA2024-T351 and AA2524-T351 aluminum friction stir welds: Part I. Metallurgical studies," *Mater. Sci. Eng. A*, vol. 364, no. 1, pp. 55–65, 2004.

[20] S. Xu and X. Deng, "A study of texture patterns in friction stir welds," *Acta Mater.*, vol. 56, no. 6, pp. 1326–1341, 2008.

[21] S. Muthukumaran and S. K. Mukherjee, "Multi-layered metal flow and formation of onion rings in friction stir welds," *Int. J. Adv. Manuf. Technol.*, vol. 38, no. 1–2, pp. 68–73, 2008.

[22] R. Fonda, A. Reynolds, C. R. Feng, K. Knipling, and D. Rowenhorst, "Material flow in friction stir welds," *Metall. Mater. Trans. A*, vol. 44, no. 1, pp. 337–344, 2013.

[23] T. U. Seidel and A. P. Reynolds, "Visualization of the material flow in AA2195 friction-stir welds using a marker insert technique," *Metall. Mater. Trans. A*, vol. 32, no. 11, pp. 2879–2884, 2001.

[24] W. T. Han, F. R. Wan, B. Leng, S. Ukai, Q. X. Tang, S. Hayashi, J. C. He, and Y. Sugino, "Grain characteristic and texture evolution in friction stir welds of nanostructured oxide dispersion strengthened ferritic steel," *Sci. Technol. Weld. Join.*, vol. 16, no. 8, pp. 690–696, 2011.

[25] D. R. Andrews and M. J. Gilpin, *The Metallurgist and Materials Technologist*. 1975.

[26] W. Tang and A. P. Reynolds, "Production of wire via friction extrusion of aluminum alloy machining chips," *J. Mater. Process. Technol.*, vol. 210, no. 15, pp. 2231–2237, 2010.

[27] F. Widerøe, T. Welo, and H. Vestøl, "A new testing machine to determine the behavior of aluminum granulate under combined pressure and shear," *Int. J. Mater. Form.*, vol. 3, no. 1, pp. 861–864, 2010.

[28] F. Abu-Farha, "A preliminary study on the feasibility of friction stir back extrusion," *Scr. Mater.*, vol. 66, no. 9, pp. 615–618, 2012.

[29] A. Hosseini, E. Azarsa, B. Davoodi, and Y. Ardahani, "EFFECT OF PROCESS PARAMETERS ON THE PHYSICAL PROPERTIES OF WIRES PRODUCED BY FRICTION EXTRUSION METHOD," *Int. J. Adv. Eng. Technol.*, 2012.

[30] V. V. Joshi, S. Jana, D. Li, H. Garmestani, E. Nyberg, and C. Lavender, "High Shear Deformation to Produce High Strength and Energy Absorption in Mg Alloys," *Magnes. Technol. 2014*, pp. 83–88, 2014.

[31] Y. S. Sato, M. Urata, and H. Kokawa, "Parameters controlling microstructure and hardness during friction-stir welding of precipitation-hardenable aluminum alloy 6063," *Metall. Mater. Trans. A*, vol. 33, no. 3, pp. 625–635, 2002.

[32] A. P. Zhilyaev and T. G. Langdon, "Using high-pressure torsion for metal processing: Fundamentals and applications," *Prog. Mater. Sci.*, vol. 53, no. 6, pp. 893–979, 2008.

[33] "Extrusion Process." [Online]. Available: http://www.themetalcasting.com/extrusion-process.html. [Accessed: 13-Apr-2015].

[34] M. Stern, *Method for treating aluminum or aluminum alloy scrap*. Google Patents, 1945.

[35] J. Gronostajski and A. Matuszak, "The recycling of metals by plastic deformation: an example of recycling of aluminium and its alloys chips," *J. Mater. Process. Technol.*, vol. 92, pp. 35–41, 1999.

[36] W. Z. Misiolek, M. Haase, N. B. Khalifa, A. E. Tekkaya, and M. Kleiner, "High quality extrudates from aluminum chips by new billet compaction and deformation routes," *CIRP Ann.-Manuf. Technol.*, vol. 61, no. 1, pp. 239–242, 2012.

[37] A. E. Tekkaya, M. Schikorra, D. Becker, D. Biermann, N. Hammer, and K. Pantke, "Hot profile extrusion of AA-6060 aluminum chips," *J. Mater. Process. Technol.*, vol. 209, no. 7, pp. 3343–3350, 2009.

[38] M. Haase, N. B. Khalifa, A. E. Tekkaya, and W. Z. Misiolek, "Improving mechanical properties of chip-based aluminum extrudates by integrated extrusion and equal channel angular pressing (iECAP)," *Mater. Sci. Eng. A*, vol. 539, pp. 194–204, 2012.

[39] D. T. McDonald, E. W. Lui, S. Palanisamy, M. S. Dargusch, and K. Xia, "Achieving Superior Strength and Ductility in Ti-6Al-4V Recycled from Machining Chips by Equal Channel Angular Pressing," *Metall. Mater. Trans. A*, vol. 45, no. 9, pp. 4089–4102, 2014.

[40] V. Güley, A. Güzel, A. Jäger, N. B. Khalifa, A. E. Tekkaya, and W. Z. Misiolek, "Effect of die design on the welding quality during solid state recycling of AA6060 chips by hot extrusion," *Mater. Sci. Eng. A*, vol. 574, pp. 163–175, 2013.

[41] D. R. Cooper and J. M. Allwood, "The influence of deformation conditions in solid-state aluminium welding processes on the resulting weld strength," *J. Mater. Process. Technol.*, vol. 214, no. 11, pp. 2576–2592, 2014.

[42] M. Haase and A. E. Tekkaya, "Cold extrusion of hot extruded aluminum chips," *J. Mater. Process. Technol.*, vol. 217, pp. 356–367, 2015.

[43] J. R. Duflou, A. E. Tekkaya, M. Haase, T. Welo, K. Vanmeensel, K. Kellens, W. Dewulf, and D. Paraskevas, "Environmental assessment of solid state recycling routes for aluminium alloys: Can solid state processes significantly reduce the environmental impact of aluminium recycling?," *CIRP Ann.-Manuf. Technol.*, 2015.

[44] F. Widerøe and T. Welo, "Using contrast material techniques to determine metal flow in screw extrusion of aluminium," *J. Mater. Process. Technol.*, vol. 213, no. 7, pp. 1007–1018, 2013.

[45] W. U. H. Syed, A. J. Pinkerton, and L. Li, "A comparative study of wire feeding and powder feeding in direct diode laser deposition for rapid prototyping," *Appl. Surf. Sci.*, vol. 247, no. 1, pp. 268–276, 2005.

[46] W. U. H. Syed and L. Li, "Effects of wire feeding direction and location in multiple layer diode laser direct metal deposition," *Appl. Surf. Sci.*, vol. 248, no. 1, pp. 518–524, 2005.

[47] S. H. Mok, G. Bi, J. Folkes, and I. Pashby, "Deposition of Ti–6Al–4V using a high power diode laser and wire, Part I: Investigation on the process characteristics," *Surf. Coat. Technol.*, vol. 202, no. 16, pp. 3933–3939, 2008.

[48] S. H. Mok, G. Bi, J. Folkes, I. Pashby, and J. Segal, "Deposition of Ti–6Al–4V using a high power diode laser and wire, Part II: Investigation on the mechanical properties," *Surf. Coat. Technol.*, vol. 202, no. 19, pp. 4613–4619, 2008.

[49] K. M. Taminger and R. A. Hafley, *Electron beam freeform fabrication (EBF3) for cost effective near-net shape manufacturing*. National Aeronautics and Space Administration, Langley Research Center, 2006.

[50] M. S. Domack, K. M. Taminger, and M. Begley, "Metallurgical Mechanisms Controlling Mechanical Properties of Aluminium Alloy 2219 Produced by Electron Beam Freeform Fabrication," in *Materials science forum*, 2006, vol. 519, pp. 1291–1296.

[51] C. A. Brice, B. T. Rosenberger, S. N. Sankaran, K. M. Taminger, B. Woods, and R. Nasserrafi, "Chemistry Control in Electron Beam Deposited Titanium Alloys," in *Materials Science Forum*, 2009, vol. 618, pp. 155–158.

[52] J. Ding, "Thermo-mechanical analysis of wire and arc additive manufacturing process," 2012.

[53] B. Ralph, *Method of making decorative articles*. Google Patents, 1925.

[54] J. Schmidt, H. Dorner, and E. Tenckhoff, "Manufacture of complex parts by shape welding," *J. Nucl. Mater.*, vol. 171, no. 1, pp. 120–127, 1990.

[55] A. F. Ribeiro, J. Norrish, and R. S. McMaster, "Practical case of rapid prototyping using gas metal arc welding," 1994.

[56] A. F. Ribeiro and J. Norrish, "Rapid prototyping using robot welding: slicing system developmens," 1996.

[57] F. Ribeiro, "3d printing with metals," *Comput. Control Eng. J.*, vol. 9, no. 1, pp. 31–38, 1998.

[58] J. D. Spencer, P. M. Dickens, and C. M. Wykes, "Rapid prototyping of metal parts by three-dimensional welding," *Proc. Inst. Mech. Eng. Part B J. Eng. Manuf.*, vol. 212, no. 3, pp. 175–182, 1998.

[59] G. Muscato, G. Spampinato, and L. Cantelli, "A closed loop welding controller for a rapid manufacturing process," in *Emerging Technologies and Factory Automation, 2008. ETFA 2008. IEEE International Conference on*, 2008, pp. 1080–1083.

[60] J. Mehnen, J. Ding, H. Lockett, and P. Kazanas, "Design for wire and arc additive layer manufacture," in *Global Product Development*, Springer, 2011, pp. 721–727.

[61] B. Baufeld, O. Van der Biest, and R. Gault, "Additive manufacturing of Ti–6Al–4V components by shaped metal deposition: microstructure and mechanical properties," *Mater. Des.*, vol. 31, pp. S106–S111, 2010.

[62] F. Wang, S. Williams, P. Colegrove, and A. A. Antonysamy, "Microstructure and mechanical properties of wire and arc additive manufactured Ti-6Al-4V," *Metall. Mater. Trans. A*, vol. 44, no. 2, pp. 968–977, 2013.

[63] B. Cong, J. Ding, and S. Williams, "Effect of arc mode in cold metal transfer process on porosity of additively manufactured Al-6.3% Cu alloy," *Int. J. Adv. Manuf. Technol.*, vol. 76, no. 9–12, pp. 1593–1606, 2015.

[64] D. Rosenthal, "The theory of moving sources of heat and its application to metal treatments," 1946.

[65] J. Goldak, A. Chakravarti, and M. Bibby, "A new finite element model for welding heat sources," *Metall. Trans. B*, vol. 15, no. 2, pp. 299–305, 1984.

[66] S. Brown and H. Song, "Finite element simulation of welding of large structures," *J. Manuf. Sci. Eng.*, vol. 114, no. 4, pp. 441–451, 1992.

[67] P. Michaleris and A. DeBiccari, "Prediction of welding distortion," *Weld. J.- Weld. Res. Suppl.*, vol. 76, no. 4, p. 172s, 1997.

[68] J. Ding, P. Colegrove, J. Mehnen, S. Ganguly, P. S. Almeida, F. Wang, and S. Williams, "Thermo-mechanical analysis of Wire and Arc Additive Layer Manufacturing process on large multi-layer parts," *Comput. Mater. Sci.*, vol. 50, no. 12, pp. 3315–3322, 2011.

[69] H. Fawad, "Heat Transfer Modeling of Metal Deposition Employing Welding Heat Source," in *Applied Mechanics and Materials*, 2013, vol. 315, pp. 463–467.

[70] T. U. Seidel and A. P. Reynolds, "Visualization of the material flow in AA2195 friction-stir welds using a marker insert technique," *Metall. Mater. Trans. A*, vol. 32, no. 11, pp. 2879–2884, 2001.

[71] W. . Arbegast, "Study of flow stress of AA6061 and AA2195," 1999.

[72] W. Tang and A. P. Reynolds, "Production of wire via friction extrusion of aluminum alloy machining chips," *J. Mater. Process. Technol.*, vol. 210, no. 15, pp. 2231–2237, 2010.

[73] H. Zhang, X. Deng, X. Li, W. Tang, A. P. Reynolds, and M. A. Sutton, "Thermo-Fluid Modeling of the Friction Extrusion Process," in *Challenges in Mechanics of Time-Dependent Materials, Volume 2*, Springer, 2015, pp. 187–196.

[74] A. Standard, "ASTM E112-96," *Stand. Test Methods Determining Aver. Grain Size*, 2004.

[75] P. Lequeu, K. P. Smith, and A. Daniélou, "Aluminum-copper-lithium alloy 2050 developed for medium to thick plate," *J. Mater. Eng. Perform.*, vol. 19, no. 6, pp. 841–847, 2010.

[76] H. Zhang, X. Li, W. Tang, X. Deng, A. P. Reynolds, and M. A. Sutton, "Heat transfer modeling of the friction extrusion process," *J. Mater. Process. Technol.*, vol. 221, pp. 21–30, 2015.

[77] K. N. Krishnan, "On the formation of onion rings in friction stir welds," *Mater. Sci. Eng. A*, vol. 327, no. 2, pp. 246–251, 2002.

[78] A. E. Tekkaya, M. Schikorra, D. Becker, D. Biermann, N. Hammer, and K. Pantke, "Hot profile extrusion of AA-6060 aluminum chips," *J. Mater. Process. Technol.*, vol. 209, no. 7, pp. 3343–3350, 2009.

[79] R. L. Klueh, J. P. Shingledecker, R. W. Swindeman, and D. T. Hoelzer, "Oxide dispersion-strengthened steels: A comparison of some commercial and experimental alloys," *J. Nucl. Mater.*, vol. 341, no. 2, pp. 103–114, 2005.

[80] J. Wang, W. Yuan, R. S. Mishra, and I. Charit, "Microstructure and mechanical properties of friction stir welded oxide dispersion strengthened alloy," *J. Nucl. Mater.*, vol. 432, no. 1, pp. 274–280, 2013.

[81] E. ASTM, "ASTM 8M-04, 2004," *Stand. Test Methods Tens. Test. Met. Mater.*

APPENDIX A − THE MATHEMATICAL METHOD OF CURVE FIT

WITH ARBITRARY ORDER

If x, y are initial coordinates of each particle, fit polynomial function like:

$$
\begin{aligned}
f(x, y) = \quad & a_{11} & +a_{12}y & \quad +a_{13}y^2 & +\cdots & +a_{1q}y^{q-1} \\
& +a_{21}x & +a_{22}xy & \quad +a_{23}xy^2 & +\cdots & +a_{2q}xy^{q-1} \\
& \vdots \\
& +a_{i1}x^{i-1} & +a_{i2}x^{i-1}y & \quad +a_{i3}x^{i-1}y^2 & +\cdots & +a_{iq}x^{i-1}y^{q-1} \\
& \vdots \\
& +a_{p1}x^{p-1} & +a_{p2}x^{p-1}y & \quad +a_{p3}x^{p-1}y^2 & +\cdots & +a_{pq}x^{p-1}y^{q-1}
\end{aligned}
$$

Where, p and q are the order of x and y respectively.

Assume:

$$
\mathbf{x} = \begin{bmatrix} 1 \\ x \\ x^2 \\ \vdots \\ x^p \end{bmatrix}, \mathbf{y} = \begin{bmatrix} 1 \\ y \\ y^2 \\ \vdots \\ y^q \end{bmatrix}, \mathbf{A} = \begin{bmatrix} a_{11} & a_{12} & \cdots & a_{1q} \\ a_{21} & a_{22} & \cdots & a_{2q} \\ \vdots & \vdots & \ddots & \vdots \\ a_{p1} & a_{p2} & \cdots & a_{pq} \end{bmatrix}
$$

So, we have:

$$
f(\mathbf{x}, \mathbf{y}) = \mathbf{x}^T \mathbf{A} \mathbf{y}
$$

Define least square function s:

$$s(a_{11},\cdots,a_{pq}) = \sum_{g=1}^{n}\omega_g[f(x_g,y_g)-z_g]^2 = \sum_{g=1}^{n}\omega_g(\sum_{i=1}^{p}\sum_{j=1}^{q}a_{ij}x^{i-1}y^{j-1}-z_g)^2$$

ω_g is the weight function, here equals to one.

Let

$$\frac{\partial s}{\partial a_{ij}} = 0$$

Which is:

$$\frac{\partial s}{\partial a_{ij}} = \frac{\partial}{\partial a_{ij}}\sum_{g=1}^{n}[f(x_g,y_g)-z_g]^2$$

$$= \sum_{g=1}^{n}\left\{2[f(x_g,y_g)-z_g]\frac{\partial}{\partial a_{ij}}[f(x_g,y_g)]\right\}$$

$$= \sum_{g=1}^{n}\left\{2[f(x_g,y_g)-z_g]x_g^{i-1}y_g^{j-1}\right\}$$

$$= 2\sum_{g=1}^{n}\left[x_g^{i-1}y_g^{j-1}f(x_g,y_g)-x_g^{i-1}y_g^{j-1}z_g\right]$$

So, we have:

$$\sum_{g=1}^{n}x_g^{i-1}y_g^{j-1}f(x_g,y_g) = \sum_{g=1}^{n}x_g^{i-1}y_g^{j-1}z_g$$

$$\sum_{g=1}^{n}x_g^{i-1}y_g^{j-1}\sum_{\alpha=1}^{p}\sum_{\beta=1}^{q}a_{\alpha\beta}x_g^{\alpha-1}y_g^{\beta-1} = \sum_{g=1}^{n}x_g^{i-1}y_g^{j-1}z_g$$

$$\sum_{g=1}^{n}x_g^{i-1}y_g^{j-1}\sum_{\alpha\beta=1,1}^{p,q}a_{\alpha\beta}x_g^{\alpha-1}y_g^{\beta-1} = \sum_{g=1}^{n}x_g^{i-1}y_g^{j-1}z_g$$

$$\sum_{\alpha\beta=1,1}^{p,q}\left[a_{\alpha\beta}\sum_{g=1}^{n}(x_g^{\alpha-1}y_g^{\beta-1}x_g^{i-1}y_g^{j-1})\right] = \sum_{g=1}^{n}x_g^{i-1}y_g^{j-1}z_g$$

176

Let:

$$u_{\alpha\beta}(i,j) = \sum_{g=1}^{n}(x_g^{\alpha-1}y_g^{\beta-1}x_g^{i-1}y_g^{j-1}) \quad v(i,j) = \sum_{g=1}^{n}x_g^{i-1}y_g^{j-1}z_g$$

,

We have:

$$\sum_{\alpha\beta=1,1}^{p,q}a_{\alpha\beta}u_{\alpha\beta}(i,j) = v(i,j)$$

, $(i,j) = (1,1),\cdots,(p,q)$

Which is:

$$\begin{bmatrix} u_{11}(1,1) & \cdots & u_{pq}(1,1) \\ \vdots & \ddots & \vdots \\ u_{11}(p,q) & \cdots u_{pq}(p,q) \end{bmatrix}\begin{bmatrix} a_{11} \\ \vdots \\ a_{pq} \end{bmatrix} = \begin{bmatrix} v(1,1) \\ \vdots \\ v(p,q) \end{bmatrix}$$

U*a=V

Solve it, the matrix *a* of polynomial function's parameter is obtained.

APPENDIX B - MATLAB CODE FOR MARKER MATERIAL

PATTERN RECONSTRUCTION

```
% Main body %


clear


%%%%%%% Step 1 input fitting coordinate value [Xi Zi] %%%%%%%


Xi=2.93:0.11:5.57;

detZi=-4.5/49;

Zi=18.5:detZi:14;


%%%%%%% Step 2 input value to be fit [t rad radius] %%%%%%%


t=[];           %input exit time matrix

rad=[];   %input exit rad matrix
```

radius=[];   %input exit radius matrix

[X,Z]=meshgrid(Xi,Zi);

surf(X,Z,t);   %Draw input figures for entire original t, rad and radius.

surf(X,Z,rad);

surf(X,Z,radius),axis([2 6 14 18.5 0 0.0015])

%%%%%%%% Step 3 input "extrusion end time": t_end %%%%%%%%

%%%%%%%% then pick useful (t<t_end) points   %%%%%%%%

t_end=27.624;

[xp,zp,tp,radp,rp]=pick(X,Z,t,rad,radius,t_end);

%%%%%%%% Step 4   surface fitting   %%%%%%%%

%%%%%%%% try from 0 to p-1 order function for X Z %%%%%%%%

%%%%%%%%   and output best fit   %%%%%%%%

%%%%%%% aa bb cc is matrix of fitting parameters for t rad radius %%%%%%

%%%   got 100*100 points in fitting area and their t rad radius values %%%

[Rsqa,aa,bpa,bqa,XI1,YI1,ZI1]=bestfit(xp,zp,tp,2.93,5.57,14,18.5,10,30);

QA=[Rsqa,bpa-1,bqa-1]; %R, order of x, order of y

```matlab
[Rsqb,bb,bpb,bqb,XI2,YI2,ZI2]=bestfit(xp,zp,radp,2.93,5.57,14,18.5,0,500);

QB=[Rsqb,bpb-1,bqb-1];

[Rsqc,cc,bpc,bqc,XI3,YI3,ZI3]=bestfit(xp,zp,rp,2.93,5.57,14,18.5,0,0.0015);

QC=[Rsqc,bpc-1,bqc-1];



%%%%% pick via eliminating points which have larger time than t_end %%%%%

[Cx,Cz,Ct,Crad,Cr]=pick(XI1,YI1,ZI1,ZI2,ZI3,t_end);



%%%%%%%   Step 5      rebuild marker in wire        %%%%%%%

%%%%%%%   obtain start and end time of extrusion   %%%%%%%

Ts=min(Ct);Te=max(Ct);

%%% calculate parameter of relationship function of time and marker height

b0=-(152*Ts)/(Te - Ts);k0=152/(Te - Ts);



pt=1; %project thickness

for lowbound=0:pt:152

    result=[];k=1;

   for n=1:length(Cx)

        for angle=-0.316:0.01:0.316

            radius=Cx(n);
```

```matlab
            [a,b]=pol2cart(angle,radius);c=(a-4.25)^2+b^2;

        if c<=1.7425

            height=Ct(n)*k0+b0;      %transfer time to height

          if (height<lowbound+pt && height>=lowbound);

            theta=rem(Crad(n),2*pi);rho=Cr(n)*1000;

            e=theta+angle;

            [xxx,yyy]=pol2cart(e,rho);

            if (xxx^2+yyy^2<=1.25^2);

            result(k,1)=xxx;result(k,2)=yyy;result(k,5)=Cz(n);

            result(k,4)=Ct(n);

            result(k,3)=height;

            k=k+1;

            end

          end

        end

      end

    end

sheetname=[num2str(lowbound) '-' num2str(lowbound+pt) 'mm.xlsx'];

xlswrite('each 1mm.xlsx',result,sheetname)

aaaa=result(:,1);bbbb=result(:,2);cccc=result(:,3);%zz=diag(cccc);
```

```matlab
% R=1.25;centerx=0;centery=0;botsurf=lowbound;length=5;

% [l,m,n]=cylinder(R,100);

% n=n*length+botsurf;

% mesh(l,m,n),hold on;

R=1.25;Rt=-pi:0.1:pi;

Rx=R*sin(Rt);Ry=R*cos(Rt);

botsurf=lowbound+0*Rt;topsurf=lowbound+pt+0*Rt;

plot3(Rx,Ry,botsurf),hold on;

plot3(Rx,Ry,topsurf),hold on;

plot3(aaaa,bbbb,cccc,'.','markersize',3);

%scatter3(aa,bb,cc,'.');

axis equal

axis([-1.5 1.5 -1.5 1.5 min(cccc) max(cccc)])

%set(gcf,'papersize',[14 10]);

scrsz = get(0,'ScreenSize');

set(gcf,'Position',scrsz);

view(3)

picname=[num2str(lowbound) '-' num2str(lowbound+pt) 'mm_ts'];

%saveas(gcf,picname,'fig');

pic=getframe(gcf);
```

imwrite(pic.cdata,strcat('E:\Friction   Stir   Processing\Friction   Extrusion\Particle

Tracing\',[num2str(lowbound) '-' num2str(lowbound+pt) 'mm_ts',',',.jpg']));

%saveas(gcf,picname,'jpg');

view([0,0,1])

picnametop=[num2str(lowbound) '-' num2str(lowbound+pt) 'mm_top_ts'];

%saveas(gcf,picnametop,'fig');

pic=getframe(gcf);

imwrite(pic.cdata,strcat(' E:\Friction   Stir   Processing\Friction   Extrusion\Particle

Tracing\',[num2str(lowbound) '-' num2str(lowbound+pt) 'mm_top_ts',',',.jpg']));

%saveas(gcf,picnametop,'jpg');

clf

end

% Subroutine 1 %

function [Leastq,A,bp,bq,XI,YI,ZI]=bestfit(x,z,f,x1,x2,y1,y2,z1,z2)

% Leastq is the least R^2 among p q from 1 to 7

% A is the matrix of fitting parameter

% bp is best p from 1 to 7

% bq is best q from 1 to 7

% XI YI are coordinates of fit position

% ZI is value in fit position

%

% x z are input coordinates

% f are value at input coordinate

% x1 x2 are up bottom range of x

% y1 y2 are up bottom range of z

% z1 z2 are up bottom range of fit value when plot surface


```matlab
Leastq=inf;

for p=1: 7

    for q =1 : 7

      clear aa;

      U=leftmatrix(x,p,z,q);

      V=rightmatrix(x,p,z,q,f);

      a_n=U\V;

      for i=1 : length(a_n)

            ii=quotient(i-1,q)+1;

            jj=mod(i-1,q)+1;
```

```matlab
            aa(ii,jj)=a_n(i,1);

    end

    Rsq=0;

    for i= 1:length(f)

        clear xl yr;

        xl(1)=1;yr(1)=1;

        for kk=0:p-1

            xl(kk+1)=x(i)^kk;

        end

        for kk=0:q-1

            yr(kk+1)=z(i)^kk;

        end

        Rsq=Rsq+(xl*aa*yr'-f(i))^2;

    end

    Lq(p,q)=Rsq;

    if Rsq<Leastq

        Leastq=Rsq;

        A=aa;bp=p;bq=q;

    end

end
```

```matlab
end

Leastq;

A;

order(1)=bp;order(2)=bq;

order;




m=300;n=450; % got 100*100 points in fitting area

[XI,YI]=meshgrid(linspace(x1,x2,m),linspace(y1,y2,n));

xx=reshape(XI,m*n,1);

yy=reshape(YI,m*n,1);




tt=zeros(m*n,1);

xy=zeros(m*n,1);

xt=zeros(m*n,1);

yt=zeros(m*n,1);




[p,q]=size(A);

for i=1 : p

    for j=1 : q
```

```matlab
    xt=xx.^(i-1);

        yt=yy.^(j-1);

        xy=xt.*yt;

        tt=tt+A(i,j).*xy;

    end

end


ZI=reshape(tt,n,m);

surf(XI,YI,ZI),axis([2 6 y1 y2 z1 z2])



% Subroutine 2 %


function U=leftmatrix(x,p,y,q)


m=length(x);

if (nargin~=4) & (m~=length(y))

    error('error check check!');

end
```

```matlab
U_length=p*q;

U=zeros(U_length,U_length);

for i=1 : p*q

    for j= 1 : p*q

        x_z=quotient(j-1,q)+quotient(i-1,q);

        y_z=mod(j-1,q)+mod(i-1,q);

        U(i,j)=qiuhe(x,x_z,y,y_z);

    end

end


% Subroutine 3 %

function V=rightmatrix(x,p,y,q,z)


if nargin~=5

    error('error check check! rightmatrix')

end


V=zeros(p*q,1);

for i=1 : p*q

    x_z=quotient(i-1,q);
```

```matlab
        y_z=mod(i-1,q);

        V(i,1)=qiuhe(x,x_z,y,y_z,z);

end


% Subroutine 4 %


function he=qiuhe(x,p,y,q,z)


m=length(x);

if (nargin<4 )&(m~=length(y))

        error('error check check!');

end

if nargin==4

        z=ones(m,1);

end


he=0;

for i=1:m

        he=he+x(i)^p * y(i)^q*z(i);

end
```

% Subroutine 5 %

```matlab
function sh=quotient(x,y)

sh=(x-mod(x,y))/y;
```

% Subroutine 6 %

```matlab
function [xp,zp,tp,radp,rp]=pick(X,Z,t,rad,radius,t_end)

N=numel(X);

Xr=reshape(X,N,1);

Zr=reshape(Z,N,1);

Tr=reshape(t,N,1);

RADr=reshape(rad,N,1);

RADIUSr=reshape(radius,N,1);

j=1;
```

```matlab
for i=1:N

  if Tr(i)<t_end

      Xrc(j)=Xr(i);Zrc(j)=Zr(i);

      Trc(j)=Tr(i);RADrc(j)=RADr(i);RADIUSrc(j)=RADIUSr(i);

      j=j+1;

  end

end

Np=numel(Xrc);

xp=reshape(Xrc,Np,1);

zp=reshape(Zrc,Np,1);

tp=reshape(Trc,Np,1);

radp=reshape(RADrc,Np,1);

rp=reshape(RADIUSrc,Np,1);
```